

High-Resolution Computational Fluid Dynamics using Enriched Finite Elements

Dissertation

**Presented in Partial Fulfillment of the Requirements
for the Degree Doctor of Philosophy in the Graduate School
of The Ohio State University**

By

Troy Patrick Shilt, B.S.

Graduate Program in Aerospace Engineering

**The Ohio State University
2021**

Dissertation Committee:

Jack J. McNamara, Advisor

Jen-Ping Chen

Carlos Armando Duarte

Datta Gaitonde

Patrick O'Hara

Copyright by
Troy Patrick Shilt
2021

Abstract

Computational fluid dynamics provides quantitative insights that complement physical experiments and enable cheaper and faster design/analysis processes. However, problems of interest tend to be highly complex, manifesting multiple physical processes over a broad range of spatial and temporal scales. The consequence of this is the desire for fluid simulations spanning many temporal and spatial scales. Here, relevant physical phenomena include steep gradients – due to shock waves, boundary layers, and laminar to turbulent boundary layer transition – and the broadband response of turbulence. Despite continual advancement in computing power, tractable analysis of problems involving such phenomena depends upon parallel advancements in the efficiency of numerical solution strategies.

In these contexts, the overarching goal of this research is to assess the numerical solution of fluid dynamic problems using an enriched finite element framework. Through an enrichment process, this framework enables the expansion of the approximation space associated with more traditional finite element methods to non-

polynomials. Non-polynomial approximation spaces better enable solution-tailored approximations that can significantly reduce computational costs. For example, previous works applying enriched finite elements in other disciplines have resulted in highly efficient numerical simulation of problems containing steep gradients, discontinuities, and singularities. Application of enriched finite elements for fluid dynamics problems is nontrivial due to numerical challenges: (1) restrictions on allowable velocity-pressure discretization for the solution of incompressible flows and (2) non-physical spurious oscillations in numerical solutions for advection dominated problems. Therefore, an enriched finite element method must address these challenges.

For applying enriched finite elements to fluid dynamics, this research focuses on (1) addressing the aforementioned numerical challenges and (2) obtaining high-accuracy numerical solutions using solution-tailored enrichments. In the presented methodology, stability and high-accuracy solutions are interlinked. Specifically, solution-tailored enrichments typically result in stable and high-accuracy solutions that capture relevant features more efficiently regarding status quo methods; Results demonstrate this for the numerical solution of the governing equations of an elastic medium, creeping flow, the advection-diffusion equation, and the Burgers' equation.

Acknowledgments

First and foremost, thanks to my advisor, Professor Jack McNamara, for everything he has taught me throughout my graduate studies. His support and guidance are invaluable and will guide me for the rest of my career. Thanks to my co-advisor, Dr. Patrick O'Hara, for his constant support, encouragement, and expertise throughout my graduate career. Also, thank you to Professor Ching-Shan Chou for serving on my candidacy committee, Professors Jen-Ping Chen and Datta Gaitonde for serving on my candidacy and dissertation committees, and Professor Carlos Armando Duarte for serving on my dissertation committee.

I want to gratefully acknowledge the financial support I have received for this work. This research was conducted with government support under and awarded by the AFRL-University Collaborative Center in Structural Sciences (Cooperative Agreement FA850-13-2347), with Dr. Benjamin Smarslok as program manager; by an AFRL/DAGSI Fellowship with Dr. Ravinder Chona as my sponsor; and a Presidential Fellowship awarded by The Ohio State University Graduate School.

I am immensely grateful to all the individuals who have provided technical in-

sight into my research. Thanks to Dr. Carlos Armando Duarte and his research group at the University of Illinois Urbana-Champaign for their collaboration and insights on enriched finite element methods. I am incredibly thankful for the guidance and mentorship of Drs. Ravinder Chona, Joeseeph Hollkamp, and Benjamin Smarslok at the AFRL/RQHF Structural Sciences Center. Also, thank you to Drs. Rohit Deshmukh and Ben Grier, Aaron Becks, Jordan Thayer, and the rest of my colleagues in Professor McNamara's research group for their technical insights on numerical methods and fluid dynamics.

I want to express my gratitude and love to my parents Margaret and Shane Shilt, as this work would not be possible without their support over the years. I want to also thank my partner Casey Swick for her constant encouragement and support. Finally, I would like to thank all my family and friends that believed in me, supported me, and made this process an enjoyable experience.

Vita

- 2017 B.S. Aerospace Engineering, Ohio State University
- 2017-2019 Researcher, Wright Patterson Air Force Base
- 2017-2021 Graduate Research Associate, Ohio State University

Publications

Journal Publications

Shilt, T., O'Hara, P. J., and McNamara, J.J., "Stabilization of advection dominated problems through a generalized finite element method," *Computer Methods in Applied Mechanics and Engineering*, Vol. 383, 2021, p. 113889.

Shilt, T., O'Hara, P. J., Deshmukh, R., and McNamara, J.J., "Solution of nearly incompressible field problems using a generalized finite element approach," *Computer Methods in Applied Mechanics and Engineering*, Vol. 368, 2020, p. 113165.

Deshmukh, R., Shilt, T., and McNamara, J.J., "Efficient representation of turbulent flows using data-enriched finite elements," *Int J Numer Methods Eng.*, 2020; 121:3397-3416.

Preprints

Shilt, T., O'Hara, P. J., and McNamara, J.J., "High-resolution solutions of non-linear, advection-dominated problems using a generalized finite element method," *arXiv*, 2021.

Conference Publications

Shilt, T., Deshmukh, R., O'Hara, P. J. and McNamara, J.J., "Data Compression and Modeling of Fluid Dynamics Using Generalized Finite Elements," *2018 Fluid Dynamics Conference AIAA 2018-4264*. June 2018.

Conference Presentations

"High-Resolution Solutions of the One-Dimensional Burgers' Equation using a Generalized Finite Element Method," *16th U.S. National Congress on Computational Mechanics*, July 28, 2021.

"Application of the Generalized Finite Element Method for Computational Fluid Dynamics," *15th U.S. National Congress on Computational Mechanics*, July 29, 2019.

Fields of Study

Major Field: Aerospace Engineering

Table of Contents

Abstract	ii
Acknowledgments	iv
Vita	vi
List of Tables	xiii
List of Figures	xiv
List of Symbols	xxi
Chapter	
1 Introduction and Objectives	1
1.1 Introduction	1
1.2 Literature Review	6
1.2.1 Solutions for Incompressible Flow	6
1.2.2 Solutions for Advection Dominated Problems	9
1.3 Objectives of this Dissertation	12
1.4 Key Novel Contributions of this Dissertation	13
2 Methodology	15
2.1 Preliminaries	15
2.2 Weak and Galerkin Formulation	16

2.3	GFEM Approximation Space	18
2.4	Time Discretization and Initial Conditions	21
2.5	Enforcing Dirichlet Boundary Conditions	22
3	Nearly Incompressible Field Problems	25
3.1	Boundary Value Problem: Linear Elasticity	26
3.1.1	Governing Equations	26
3.1.2	Matrix Formulation	27
3.2	Boundary Value Problem: Stokes Flow	29
3.2.1	Governing Equations and the Penalty Pressure Method	29
3.2.2	A Note on Locking	30
3.3	Numerical Results	32
3.3.1	2D Elasticity Equations with Volumetric Forcing	32
3.3.2	2D Stokes Flow: Lid-Driven Cavity Problem	35
3.4	General Discussion	42
4	Stabilization of Advection Dominated Problems	45
4.1	The GFEM as a Stabilized Method	46
4.1.1	Variational Multiscale Method	46
4.1.2	Stabilized Methods	48
4.1.3	Reformulation of the GFEM	49
4.2	Example: Stabilization of a Steady, 1D Advection-Diffusion Equation	55
4.3	Obtaining Stabilizing Enrichments in GFEM	59
4.3.1	Fundamental Solutions to the 1D and 2D Advection-Diffusion Equation	63
4.3.2	<i>A Priori</i> Error Estimations	64
5	GFEM Solution to the Advection-Diffusion Equation	66
5.1	Governing Equation and GFEM Linear System of Equations	67

5.2	Numerical Results	68
5.2.1	Example: 1D Steady Advection-Diffusion Equation with Complex Volumetric Forcing	69
5.2.2	Example: 1D Unsteady Advection-Diffusion Equation with Complex Initial Condition	71
5.2.3	Example: 2D Steady Advection-Diffusion Equation with Complex Volumetric Forcing	74
5.2.4	Example: 2D Steady Advection-Diffusion Equation with Advection Skewed to the Grid	80
5.2.5	Example: 2D Unsteady Advection-Diffusion Equation with Periodic Boundary Conditions	83
5.3	General Discussion	87
6	GFEM Solution to the Burgers' Equation	93
6.1	Viscous Burgers' Equation	94
6.1.1	Governing equation	94
6.1.2	GFEM Nonlinear System of Equations	95
6.1.3	Iteration of the Nonlinear System using the Newton-Raphson Method	97
6.2	Inviscid Burgers' Equation	98
6.2.1	Governing Equation	98
6.2.2	Formation of Shocks	98
6.2.3	A Note on Stability	100
6.3	Numerical Results	101
6.3.1	Example 1: Boundary Layer Solution as the Kinematic Viscosity Tends Toward Zero	103
6.3.1.1	Problem Statement and Reference Solutions	103
6.3.1.2	Finite Element Solutions	105
6.3.1.3	Generalized Finite Element Solutions	107

6.3.2	Example 2: Shock Formulation in the Domain	113
6.3.2.1	Problem Statement and Reference Solutions	113
6.3.2.2	Numerical Solutions	116
6.3.2.3	Capturing Intermediate Solution Features	118
6.4	General Discussion	123
7	Concluding Remarks	131
7.1	Principal Conclusions Obtained in this Study	131
7.2	Recommendations for Future Research	134
	Bibliography	137

List of Tables

3.1	Lamé parameters (μ, λ) for $E = 1500$ and ν	35
-----	---	----

List of Figures

1.1	Multiscale features of a Mach 2.25 turbulent equilibrium flow parallel to a 90 degree corner (simulation of a $977 \times 473 \times 805$ point grid over a 0.0012 sec. time-window requiring approximately 1.6 TB of data).	3
1.2	Depiction of two-dimensional FEM shape functions (φ_α), enrichment functions ($E_{\alpha j}$), and GFEM shape functions ($\phi_{\alpha j} = \varphi_\alpha E_{\alpha j}$) over node α	5
1.3	Abstract depiction of expanding the FEM approximation space through the GFEM enrichment process.	5
2.1	Patches (ω_α) and the partition of unity composed of linear, Lagrangian shape functions (φ_α) over a one-dimensional, uniformly discretized computational domain (Ω).	19
3.1	Domain (Ω) and Dirichlet boundary conditions ($\mathbf{u} = \mathbf{g}_{\Gamma_D}$) for the elasticity problem.	33
3.2	Reference solution (\mathbf{u}) for the elasticity problem.	33
3.3	Energy norms ($\ \mathbf{u}\ _E$) over a range of Poisson's ratio (ν).	36
3.4	u -displacement absolute error contours ($ u - u_h $) for $\nu = 0.49999$ over an 80x80 element grid.	37
3.5	v -displacement absolute error contours ($ v - v_h $) for $\nu = 0.49999$ over an 80x80 element grid.	38

3.6	Domain (Ω) and Dirichlet boundary conditions ($\mathbf{u} = \mathbf{g}_{\Gamma_D}$) for the lid-driven cavity problem.	40
3.7	Lid-driven cavity velocity field (\mathbf{u}) for 160×160 cubic GFEM solution.	40
3.8	Energy norm ($\ \mathbf{u}\ _E$) versus total degrees of freedom (N_{DOF}) for lid-driven cavity problem.	41
3.9	u -displacement absolute error contours ($ u - u_h $) over an 80×80 element grid.	42
3.10	v -displacement absolute error contours ($ v - v_h $) over an 80×80 element grid.	43
4.1	Optimal stabilization parameter ($\tau_{optimal}$) and the GFEM stabilization parameter (τ_{GFEM}) as the local Péclet number (Pe) increases.	59
4.2	Relative H_1 norm $\left(\frac{\ u_h - u\ _{H_1}}{\ u\ _{H_1}}\right)$ versus total degrees of freedom (N_{DOF}) for a simple advection-diffusion problem.	60
4.3	10-element solutions (u) for a simple advection-diffusion problem.	61
5.1	2000 element cubic GFEM reference solution (u) for the 1D steady advection-diffusion problem with complex volumetric forcing ($f(x)$)	71
5.2	Relative H_1 norm $\left(\frac{\ u_h - u\ _{H_1}}{\ u\ _{H_1}}\right)$ versus degrees of freedom (N_{DOF}) for the 1D steady advection-diffusion problem with complex volumetric forcing ($f(x)$).	72
5.3	48 DOF linear, quadratic, and cubic solutions (a) with and (b) without exponential enrichments.	72
5.4	1000 element cubic GFEM reference solution (u) for the 1D unsteady advection-diffusion problem with complex initial condition ($u_{IC}(x)$).	75
5.5	Relative H_1 norm $\left(\frac{\ u_h - u\ _{H_1}}{\ u\ _{H_1}}\right)$ versus normalized time (\bar{t}) at 24 DOFs for the 1D unsteady advection-diffusion problem with complex initial condition ($u_{IC}(x)$).	75

5.6	24 DOF linear, quadratic, and cubic solutions (u_h) with ((a), (c), (e)) and without ((b), (d), (f)) exponential enrichments for the 1D unsteady advection-diffusion problem with complex initial condition (u_{IC}).	76
5.7	Relative H_1 norm $\left(\frac{\ u_h - u\ _{H_1}}{\ u\ _{H_1}}\right)$ versus total degrees of freedom (N_{DOF}) at various normalized times (\bar{t}) before and after a steep boundary layer forms for the 1D unsteady advection-diffusion problem with complex initial condition (u_{IC}).	77
5.8	Reference solution (u) for the 2D steady advection-diffusion problem with complex volumetric forcing ($f(\mathbf{x})$).	78
5.9	Relative H_1 norm $\left(\frac{\ u_h - u\ _{H_1}}{\ u\ _{H_1}}\right)$ versus total degrees of freedom (N_{DOF}) for the 2D steady advection-diffusion problem with complex volumetric forcing ($f(\mathbf{x})$).	79
5.10	147±3 DOF solutions (u_h) along the slice for the 2D steady advection-diffusion problem with complex volumetric forcing ($f(\mathbf{x})$).	79
5.11	Dirichlet boundary conditions ($d(\mathbf{x})$) for the 2D advection skewed to the grid problem.	81
5.12	400 × 400 element, linear FEM reference solutions (u) at various flow angles (θ) for the 2D advection skewed to the grid problem.	82
5.13	Absolute error contours ($ u_h - u $) for $\theta = 22.5$ deg for the 2D advection skewed to the grid problem.	83
5.14	Absolute error contours ($ u_h - u $) for $\theta = 45$ deg for the 2D advection skewed to the grid problem.	84
5.15	Absolute error contours ($ u_h - u $) for $\theta = 67.5$ deg for the 2D advection skewed to the grid problem.	84
5.16	Relative H_1 norm $\left(\frac{\ u_h - u\ _{H_1}}{\ u\ _{H_1}}\right)$ versus total degrees of freedom (N_{DOF}) at various flow angles (θ) for the 2D advection skewed to the grid problem.	85

5.17	Relative H_1 norm $\left(\frac{\ u_h - u\ _{H_1}}{\ u\ _{H_1}}\right)$ versus $\frac{1}{h}$ at various flow angles (θ) for the 2D advection skewed to the grid problem.	85
5.18	Reference solution (u) for the 2D unsteady advection-diffusion problem with periodic boundary conditions.	89
5.19	Relative H_1 norm $\left(\frac{\ u_h - u\ _{H_1}}{\ u\ _{H_1}}\right)$ versus normalized time (\bar{t}) for the 2D unsteady advection-diffusion problem with periodic boundary conditions.	90
5.20	147 ± 3 DOF solutions (u_h) along slice for the 2D unsteady advection-diffusion problem with periodic boundary conditions.	91
5.21	Relative H_1 norm $\left(\frac{\ u_h - u\ _{H_1}}{\ u\ _{H_1}}\right)$ versus total degrees of freedom (N_{DOF}) at various normalized times (\bar{t}) before and after a steep boundary layer forms with periodic boundary conditions.	92
6.1	Riemann solutions (u) for various initial conditions ($u_I C(x)$).	101
6.2	Reference solution contours (u) for the boundary layer problem over a range of kinematic viscosities (ν)	105
6.3	Linear ($p = 1$) FEM convergence in the relative L_2 norm $\left(\frac{\ u_h - u\ _{L_2}}{\ u\ _{L_2}}\right)$ versus total degrees of freedom (N_{DOF}) for the boundary layer problem at various times (t).	106
6.4	Linear ($p = 1$) FEM convergence in the relative H_1 norm $\left(\frac{\ u_h - u\ _{H_1}}{\ u\ _{H_1}}\right)$ versus total degrees of freedom (N_{DOF}) for the boundary layer problem at various times (t).	107
6.5	11-element, linear ($p = 1$) FEM solution contours (u_h) for the boundary layer problem over a range of kinematic viscosities (ν).	107
6.6	47-element, linear ($p = 1$) FEM solution contours (u_h) for the boundary layer problem over a range of kinematic viscosities (ν).	108
6.7	Convergence in the relative L_2 integral norm $\left(\frac{\ u_h - u\ _{L_2}}{\ u\ _{L_2}}\right)$ versus total degrees of freedom (N_{DOF}) for the boundary layer problem with kinematic viscosity $\nu = \frac{1}{100}$ using exponential enrichments.	109

6.8	Convergence in the relative H_1 integral norm $\left(\frac{\ u_h - u\ _{H_1}}{\ u\ _{H_1}}\right)$ versus total degrees of freedom (N_{DOF}) for the boundary layer problem with kinematic viscosity $\nu = \frac{1}{100}$ using exponential enrichments.	110
6.9	Relative L_2 $\left(\frac{\ u_h - u\ _{L_2}}{\ u\ _{L_2}}\right)$ and H_1 $\left(\frac{\ u_h - u\ _{H_1}}{\ u\ _{H_1}}\right)$ integral norms versus time (t) for 11-element and 95-element FEM and $p = 1 + \text{exp.}$ GFEM for the boundary layer problem with kinematic viscosity $\nu = \frac{1}{100}$	111
6.10	11-element, $p = 1$ FEM (12 DOF) and $p = 1 + \text{exp.}$ GFEM (15 DOF) solution contours (u_h) compared to the reference for the boundary layer problem with $\nu = \frac{1}{100}$	111
6.11	Convergence in the relative L_2 integral norm $\left(\frac{\ u_h - u\ _{L_2}}{\ u\ _{L_2}}\right)$ versus total degrees of freedom (N_{DOF}) for the boundary layer problem with $\nu = 0$ using Heaviside enrichments.	113
6.12	Convergence in the relative H_1 integral norm $\left(\frac{\ u_h - u\ _{H_1}}{\ u\ _{H_1}}\right)$ versus total degrees of freedom (N_{DOF}) for the boundary layer problem with $\nu = 0$ using Heaviside enrichments.	114
6.13	Relative L_2 $\left(\frac{\ u_h - u\ _{L_2}}{\ u\ _{L_2}}\right)$ and H_1 $\left(\frac{\ u_h - u\ _{H_1}}{\ u\ _{H_1}}\right)$ integral norms versus time (t) for 11-element and 95-element FEM and $p = 1 + \text{disc.}$ GFEM for the boundary layer problem with kinematic viscosity $\nu = 0$	114
6.14	11-element $p = 1$ FEM (12 DOF) $p = 1 + \text{disc.}$ GFEM (13 DOF) solution contours (u_h) compared to the reference for the boundary layer problem with kinematic viscosity $\nu = 0$	115
6.15	47-element $p = 1$ FEM (48 DOF) $p = 1 + \text{disc.}$ GFEM (49 DOF) solution contours (u_h) compared to the reference for the boundary layer problem with kinematic viscosity $\nu = 0$	115
6.16	5000-element FEM reference solutions (u) for various kinematic viscosities (ν) for the shock problem.	119

6.17	Relative L_2 norm $L_2 \left(\frac{\ u_h - u\ _{L_2}}{\ u\ _{L_2}} \right)$ versus time (t) for 11-, 23-, 47-, 95-element, and 191-element $p = 1$ FEM and $p = 1 + ss$ GFEM solutions over various kinematic viscosities (ν) for the shock problem.	119
6.18	Relative H_1 norm $H_1 \left(\frac{\ u_h - u\ _{H_1}}{\ u\ _{H_1}} \right)$ versus time (t) for 11-, 23-, 47-, 95-element, and 191-element $p = 1$ FEM and $p = 1 + ss$ GFEM solutions over various kinematic viscosities (ν) for the shock problem.	120
6.19	11-element $p = 1$ FEM and $p = 1 + ss$ GFEM solution contours (u_h) over various kinematic viscosities (ν) for the shock problem. . . .	120
6.20	47-element $p = 1$ FEM and $p = 1 + ss$ GFEM solution contours (u_h) over various kinematic viscosities (ν) for the shock problem. . . .	121
6.21	Convergence the relative L_2 integral norm $\left(\frac{\ u_h - u\ _{L_2}}{\ u\ _{L_2}} \right)$ versus total degrees of freedom (N_{DOF}) for the shock problem with kinematic viscosity $\nu = \frac{1}{50}$	121
6.22	Convergence the relative L_2 integral norm $\left(\frac{\ u_h - u\ _{L_2}}{\ u\ _{L_2}} \right)$ versus total degrees of freedom (N_{DOF}) for the shock problem with kinematic viscosity $\nu = \frac{1}{100}$	122
6.23	Convergence the relative L_2 integral norm $\left(\frac{\ u_h - u\ _{L_2}}{\ u\ _{L_2}} \right)$ versus total degrees of freedom (N_{DOF}) for the shock problem with kinematic viscosity $\nu = \frac{1}{500}$	123
6.24	Convergence the relative L_2 integral norm $\left(\frac{\ u_h - u\ _{L_2}}{\ u\ _{L_2}} \right)$ versus total degrees of freedom (N_{DOF}) for the shock problem with kinematic viscosity $\nu = \frac{1}{1000}$	124
6.25	Convergence the relative H_1 integral norm $\left(\frac{\ u_h - u\ _{H_1}}{\ u\ _{H_1}} \right)$ versus total degrees of freedom (N_{DOF}) for the shock problem with kinematic viscosity $\nu = \frac{1}{50}$	125
6.26	Convergence the relative H_1 integral norm $\left(\frac{\ u_h - u\ _{H_1}}{\ u\ _{H_1}} \right)$ versus total degrees of freedom (N_{DOF}) for the shock problem with kinematic viscosity $\nu = \frac{1}{100}$	126

6.27	Convergence the relative H_1 integral norm $\left(\frac{\ u_h - u\ _{H_1}}{\ u\ _{H_1}}\right)$ versus total degrees of freedom (N_{DOF}) for the shock problem with kinematic viscosity $\nu = \frac{1}{500}$.	127
6.28	Convergence the relative H_1 integral norm $\left(\frac{\ u_h - u\ _{H_1}}{\ u\ _{H_1}}\right)$ versus total degrees of freedom (N_{DOF}) for the shock problem with kinematic viscosity $\nu = \frac{1}{1000}$.	127
6.29	Set of shock enrichments $\left(E_{\alpha j} = \tanh\left[\frac{1}{2\rho}\left(\frac{1}{2} - x\right)\right]\right)$ for various ρ	128
6.30	Relative L_2 $\left(\frac{\ u_h - u\ _{L_2}}{\ u\ _{L_2}}\right)$ and H_1 $\left(\frac{\ u_h - u\ _{H_1}}{\ u\ _{H_1}}\right)$ integral norms versus time (t) for 11-element FEM and GFEM solutions to the shock formation problem when kinematic viscosity $\nu = \frac{1}{500}$.	128
6.31	Relative L_2 $\left(\frac{\ u_h - u\ _{L_2}}{\ u\ _{L_2}}\right)$ and H_1 $\left(\frac{\ u_h - u\ _{H_1}}{\ u\ _{H_1}}\right)$ integral norms versus time (t) for 47-element FEM and GFEM solutions to the shock formation problem when kinematic viscosity $\nu = \frac{1}{500}$.	129
6.32	Convergence the relative L_2 integral norm $\left(\frac{\ u_h - u\ _{L_2}}{\ u\ _{L_2}}\right)$ versus total degrees of freedom (N_{DOF}) for the shock problem with kinematic viscosity $\nu = \frac{1}{500}$.	129
6.33	Convergence the relative H_1 integral norm $\left(\frac{\ u_h - u\ _{H_1}}{\ u\ _{H_1}}\right)$ versus total degrees of freedom (N_{DOF}) for the shock problem with kinematic viscosity $\nu = \frac{1}{500}$.	130

List of Symbols

$a(\cdot, \cdot)$	= bilinear operator
a_x	= rate of advection in the x-direction
a_y	= rate of advection in the y-direction
b	= boundary operator
\mathbf{c}	= vector of weighting coefficients
C	= energy norm constant
C^m	= set of functions continuous up to the n th derivative
E	= Young's modulus
$E_{\alpha j}$	= the j th enrichment function defined over node α
\mathbf{f}, f	= volumetric forcing
g'	= fine/subgrid scale Green's function
\bar{g}'	= approximation of g'
\bar{g}'_e	= elemental Green's function
$\mathbf{g}_{\Gamma_D}, g_{\Gamma_D}$	= Dirichlet boundary conditions
$\mathbf{g}_{\Gamma_N}, g_{\Gamma_N}$	= Neumann boundary conditions
h	= element size
H^1	= first order Hilbert space
\tilde{H}^1	= subset of H^1 satisfying prescribed Dirichlet boundary conditions
\dot{H}^1	= subset of H^1 which vanish on the Dirichlet boundary
k	= rate of diffusion
\mathcal{L}	= linear differential operator

L_2	= space of Lebesgue square-integrable functions
m_α	= dimension of the space χ_α
n	= number of dimensions
$N(h)$	= total number of nodes in the domain Ω , determined by h
p	= polynomial order
Pe	= Peclet number
\mathbb{R}^n	= n -dimensional set of real numbers
Re	= Reynolds number
S_{GFEM}	= GFEM trial space
\mathbf{u}, u	= test/solution field
\mathbf{u}_h, u_h	= FEM/GFEM approximation
\mathbf{u}_0, u_0	= initial condition
\bar{u}	= coarse/resolved scales
u'	= fine/subgrid scales
U	= strain energy
\tilde{V}	= finite-dimensional subspace of \tilde{H}^1
\dot{V}	= finite-dimensional subspace of \dot{H}^1
\mathbf{w}, w	= trial/weighting functions
\mathbf{w}_h, w_h	= FEM/GFEM trial/weighting functions
\bar{w}	= coarse/resolved trial/weighting functions
w'	= fine/subgrid scale trial/weighting functions
\mathbf{x}_α	= coordinate location of node α , where patch ω_α is defined
α	= node in the computational domain
β	= penalty parameter for enforcing Dirichlet boundary conditions
Γ	= domain boundary
Γ_D	= domain boundary where Dirichlet boundary conditions are prescribed
Γ_N	= domain boundary where Neumann boundary conditions are prescribed
δ	= Dirac delta function

ϵ	= penalty pressure parameter
θ	= flow angle
λ	= first Lamé parameter
μ	= second Lamé parameter
ν	= Poisson's ratio or kinematic viscosity
τ	= stabilization parameter
φ	= finite element shape function over node α
$\phi_{\alpha j}$	= the j th GFEM shape function corresponding to node α
χ_{α}	= local approximate space / space of enrichment functions over patch ω_{α}
ω_{α}	= patch defined over node α
Ω	computational domain
$(\cdot, \cdot)_{\Omega}$	= inner product over the domain Ω
\cup	= union
\cap	= intersection
\subset	= subset
\in	= an element of
\forall	= for all
\emptyset	= null set

Chapter 1

Introduction and Objectives

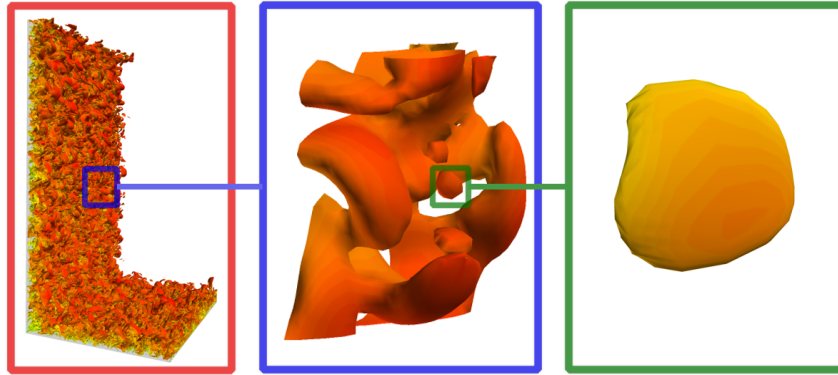
1.1 Introduction

Fluids make up the atmosphere, ocean, and parts of Earth's internal structure. Fluids are essential to life, such as blood flow for transporting oxygen and other essential nutrients to our cells. Fluids are fundamental for developing and improving medical devices, transportation systems, renewable energy systems, and defense systems. Thus, fluids underlie or directly impact a vast range of significant problems. The Navier-Stokes equations describe fluid dynamics at continuum length scales, which assume a fluid obeys the conservation of mass and momentum. The nonlinearity of these equations combined with complex, multiscale phenomena often precludes analytical solutions. Therefore, it is often necessary to conduct experiments and simulate the Navier-Stokes equations with numerical methods to gain quantitative insight.

Computational fluid dynamics (CFD) refers to numerical methods that approx-

imate the Navier-Stokes equations. High-fidelity CFD models provide unprecedented quantitative insights into complex physical systems, aiding experimental work and enabling cheaper and faster design/analysis processes. However, the demand for very fine discretizations to accurately resolve the multiscale behavior of fluids often requires days to weeks to complete, even on high-performance computers. Additionally, the amount of data required for storage quickly becomes unreasonable for simulations with long time records. Consider Fig. 1.1, which shows a high-density, implicit large eddy simulation of a Mach 2.25 turbulent equilibrium flow parallel to a 90 degree corner ($977 \times 473 \times 805$ grid points) [1]. These computations came from the Air Force Research Laboratory's supercomputer "Thunder," performing 1 million iterations with an estimated cost of 1.2M CPU-hrs (i.e., 5,000 cores require approx. 240 hours to complete). To fully capture the multiscale features of the turbulent flow over a time record of 0.0012 seconds requires approximately 1.6 TB of data. Numerical simulation of physically relevant problems often demands time records much larger than those currently attainable. Thus, there is a motivation to pursue more efficient solution strategies for the Navier-Stokes equations.

Numerical schemes typically carried out for CFD use the finite difference (FDM), finite volume (FVM), or finite element (FEM) methods. To date, no scheme is a perfect approach to the numerical solution of fluid dynamics problems. This research focuses on finite elements; FEM has well-known advantages, including the ability to handle complex geometry, incorporate differential-type boundary con-



Data courtesy of Dr. Nicholas Bisek (AFRL)

Figure 1.1: Multiscale features of a Mach 2.25 turbulent equilibrium flow parallel to a 90 degree corner (simulation of a $977 \times 473 \times 805$ point grid over a 0.0012 sec. time-window requiring approximately 1.6 TB of data).

ditions naturally, and a rich mathematical structure that enables theoretical error estimates [5]. However, FEM incurs challenges when applied to the prediction of fluids that restricts widespread use, as solution strategies to these challenges often limit approximation spaces to be relatively low-order. These challenges include: (1) restrictions on allowable velocity-pressure discretization for the solution of incompressible flows, (2) non-physical, spurious oscillations that arise in numerical solutions for advection dominated problems, and (3) capturing steep gradients due to shock waves, boundary layers, and laminar to turbulent boundary layer transition.

A potential solution to these challenges using an enriched finite element framework is the focus of this research. More specifically, this work explores the generalized finite element method (GFEM). GFEM was developed concurrently by Babuska and Melenk at the University of Maryland [6–8], and by Duarte and Oden

at the University of Texas at Austin [9–11]. Work also exists for the eXtended finite element method (XFEM) developed at the Northwestern University [12], which is noted in Gracie et al. [13] as equivalent to the GFEM. As such, the rest of this dissertation opts to use GFEM to refer to both methods. Briefly, the GFEM is an extension of the finite element framework that expands the finite element approximation space through an “enrichment process” [14] (see Fig. 1.2). The appeal of this enrichment process is that it enables the implementation of functions that may be one or more of the following: non-polynomial, analytical, numerical, solution-tailored, and time-dependent (see Fig. 1.3). The versatility of the GFEM has led to success in addressing several challenges, predominantly in solid mechanics and heat transfer problems, such as handling steep gradients [15], capturing discontinuities and singularities [16], and modeling of three-dimensional fatigue crack propagation [17].

This research is focused on a deep study of the role of enrichment functions when applying GFEM to the solution of fluid dynamics problems. Enrichments in this work are considered in two aspects to address the aforementioned numerical challenges incurred in finite elements: (1) stability and (2) high accuracy. In the presented methodology, stable and efficient, high accuracy solutions are interlinked. Specifically, solution-tailored enrichments typically result in stable and high-accuracy solutions that capture relevant features more efficiently compared to status quo methods. As such, this work is focused mainly on numerical stability using enrichment functions, with higher accuracy arising as a result. The following

section details the state-of-the-art finite element methods applied to fluid dynamics for the following numerical challenges: (1) solutions to incompressible flow and (2) solutions to advection-dominated problems.



(a) continuous enrichment

(b) discontinuous enrichment

Figure 1.2: Depiction of two-dimensional FEM shape functions (φ_α), enrichment functions ($E_{\alpha j}$), and GFEM shape functions ($\phi_{\alpha j} = \varphi_\alpha E_{\alpha j}$) over node α .

$$\mathbf{u}_h(\mathbf{x}, t) = \left\{ \sum_{\alpha=1}^{N_{nodes}} \hat{\mathbf{u}}_\alpha(t) \varphi_\alpha(\mathbf{x}) \right\} \text{FEM} + \left\{ \sum_{\alpha=1}^{N_{nodes}} \varphi_\alpha(\mathbf{x}) \sum_{j=1}^{N_{enrich}} \tilde{\mathbf{u}}_{\alpha j}(t) E_j(\mathbf{x}) \right\} \text{Enrichment of FEM}$$

Approximation space (abstraction)

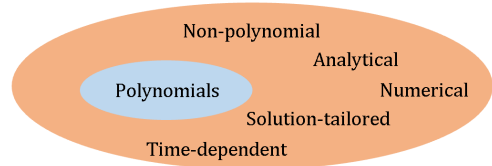


Figure 1.3: Abstract depiction of expanding the FEM approximation space through the GFEM enrichment process.

1.2 Literature Review

1.2.1 Solutions for Incompressible Flow

For flows where the viscous forces overshadow inertial terms, the Navier-Stokes equations simplify to a set of governing equations often referred to as Stokes flow / creeping flow. The governing equations for Stokes flow lead to a class of formulations referred to as saddle-point problems [28, 29]. The approximation of these saddle-point problems using Galerkin finite element methods must satisfy a stability condition known as the Ladyzhenskaya-Babuška-Brezzi (LBB) condition [30–32]. Mixed-element methods [29] use finite element shape functions that satisfy the LBB condition. Unfortunately, the restrictions on the approximation space due to the LBB condition are severe, which has motivated a significant number of efforts to alleviate this shortcoming.

Legrain et al. [33] and Srinivasan et al. [34] explored GFEM application to (near-)incompressible problems involving discontinuities. The result is stable solutions to the saddle-point formulation. However, this process requires the enriched solution space to satisfy the LBB condition; thus, restrictions on the available approximation remain. Furthermore, these approaches are valid only for low-order methods, and further work is necessary to obtain stable high-order solutions.

Perhaps the most widely known class of methods developed to address the LBB condition are the stabilized methods: pressure-stabilizing/Petrov-Galerkin

method [35], Galerkin/least-squares [36], and residual-free bubbles [37]. Hughes later showed in [38] that stabilized methods could be derived from a variational multiscale framework. Essentially, stabilized methods account for the residual error of the discretized solution by modifying the variational form of the governing equations. The result is the stability of approximations that would otherwise not be conformal in the mixed-element framework. Unfortunately, these stabilized methods are generally limited to h -refinement (grid refinement) strategies, and the stabilizing terms do contribute towards improving the rate of convergence of the solution.

Other methods developed to circumvent the LBB condition are divergent-free methods [39] and segregated methods [40]. Divergent-free methods aim to develop a divergence-free approximation space such that the LBB condition is alleviated. However, it is challenging to obtain high-order interpolations that maintain a divergent free space. Segregated methods are a class of iterative methods in which one sequentially solves for the velocities and pressure fields at each iteration. These iterations are not ideal for high-fidelity solutions since it requires carrying them out with large matrices.

In this work, the penalty pressure method is considered [41]. Here the LBB condition is circumvented by adding negligible compressibility to the Stokes flow equations using a penalty parameter. Note that implementing the penalty pressure method to Stokes flow results in equations of equivalent form to elasticity equations for nearly incompressible materials. Thus, this work explores the application

of GFEM to incompressible field problems in general. Typically, the challenge of such an approach is the introduction of *locking* - a phenomenon that results in various finite element schemes returning poor rates of convergence [42].

One commonly employed approach for addressing locking is selective or reduced integration, which demonstrates equivalency to the classical mixed-element methods [41]. Seabra et al. [43] explored the application of the GFEM for nearly incompressible problems involving discontinuities through the use of reduced integration. Here reduced integration schemes were developed for the discontinuous enrichments, which resulted in optimal convergence. There is a large body of literature, generally referred to as B-bar methods [35, 44, 45], encompassing the aforementioned modified integration techniques, along with other similar approaches aimed at augmenting the element formulation to satisfy the incompressibility constraint on an average sense over each element (see, for example, Herrmann [46]), as opposed to attempting enforcement at each integration point. These methods have succeeded in incompressible media problems but generally use standard Lagrangian elements. They thus do not lend themselves to higher-order approximations and improved convergence rates, such as those attainable with the GFEM proposed in this work.

In the GFEM context, there is no requirement to modify the (GFEM) element formulation or use reduced integration schemes to alleviate locking, and thus the potential numerical issues which may arise from the use of reduced numerical integration schemes can be avoided with the GFEM approach. Note Babuska and

Suri [42] explored higher-order FEM using Lagrangian elements *without* reduced integration and found that higher-order elements maintained optimal convergence but observed a shift in the constant in the error estimates. The benefit of such a formulation is that the shift is recoverable through improved convergence rates provided by higher order elements. However, the complexity of implementing a higher-order basis in standard FEM often limits application to quadratic or cubic solutions at best. It is shown in this work that, similar to work done in [42], properties of the GFEM formulation address the effect of locking naturally. The result is a stable GFEM approximation of the Stokes flow equations using the penalty pressure method without reduced integration. This work presents a robust method that enables optimal solution convergence for this class of problems. Details on GFEM solutions to incompressible field problems are found in chapter 3, for GFEM applied to a 2D elasticity problem driven by volumetric forcing, as well as a 2D lid-driven cavity problem.

1.2.2 Solutions for Advection Dominated Problems

For advection-dominated problems in traditional finite element approaches, spurious node-to-node oscillations manifest in the solution due to the inherent truncation error of the discretized Galerkin approximation [47]. One of the first approaches to surface that addressed this challenge was the streamline upwind/Petrov-Galerkin method (SUPG) developed by Brooks and Hughes in [5]. SUPG ad-

dressed shortcomings of classical upwind techniques by only adding artificial diffusion in the streamlined direction. The result is no artificial diffusion perpendicular to the flow direction; thus, oscillation-free solutions are obtainable with convergence behavior comparable to classical Galerkin methods.

In the years to follow, the advancing mathematical theory resulted in several improvements. Most notable are the Galerkin/least-squares (GLS) [36], [48] and residual-free bubble methods [37], [49]. The GLS method is essentially a generalization of the SUPG method motivated by mathematical analysis rather than artificial diffusion. For residual-free bubbles, the basic idea is to use bubble functions (functions that vanish on element boundaries) to approximate the residual error introduced by the standard FEM. The use of these bubble functions allows the elimination of the additional degrees of freedom by static condensation, which ultimately results in a stabilization term added to the standard Galerkin FEM formulation.

Eventually, the observed similarities between the methods above, now often denoted stabilized methods, resulted in the development of the variational multi-scale (VMS) method by Hughes [38], [50]. The VMS method is a general framework that stabilized methods are derivable through. Fundamentally, the VMS method decomposes a solution into coarse/resolved scales and fine/subgrid scales. A stable solution for the coarse scales is obtainable when using an analytical representation for the fine scales. However, for most problems, and the analytical fine-scale solution is not available. Therefore additional assumptions are required

which tailor stabilized methods to a particular set of governing equations. Unfortunately, these assumptions often result in low-order methods [51]. Thus, a high-order method necessarily requires alleviation of some assumptions made in classical stabilized methods.

Turner et al. previously explored GFEM application for advection-dominated problems in [52], using both analytical and numerical functions as enrichments for the steady advection-diffusion equation. The work resulted in stable solutions at Péclet numbers above one. Additionally, Turner et al. briefly made connections between the GFEM, GLS, and residual-free bubble methods. In these contexts, this work explores the GFEM for advection-dominated problems and the connection to the VMS method. This work expands upon the work of Turner et al. in the following ways: (1) a generalized formulation is used to decompose GFEM consistently with the VMS method, highlighting the natural capability of the GFEM enrichment process for stabilization of a linear differential operator, (2) stabilizing enrichments are obtained based on the fundamental solutions of the linear differential operator, providing a deeper understanding of the underlying solution features necessary for stabilizing advection dominated solutions, and (3) the applied GFEM framework expands to time-dependent advection-diffusion problems and the nonlinear Burgers' equation.

1.3 Objectives of this Dissertation

The overarching goal of this research is to develop and assess the GFEM for the numerical solution of the Navier-Stokes equations. However, the solution to the complete Navier-Stokes equations involves addressing several challenges at once. Thus, an approach is taken in this work to decompose issues in solving the Navier-Stokes equations into manageable pieces. First is focus on the Stokes flow equations for instabilities in incompressible flow, a simplified version of the incompressible Navier-Stokes equations. Essentially, the nonlinear advection term is removed in Stokes flow while maintaining the challenge of incompressibility. For advection-dominated problems, this work initially focuses on the linear advection-diffusion equation. Numerical discretization of this equation exhibits similar instabilities in the advection term as the Navier-Stokes equations; however, it avoids additional complexity introduced by the nonlinear term and additional variables of interest: density, pressure, temperature. Nonlinearity is considered by focusing on the Burgers' equation, equivalent to the advection-diffusion equation, except the advection rate is replaced with the solution variable itself. This equation has many features similar to the Navier-Stokes equations and is used to clarify the interaction between temporal, dissipative, and nonlinear terms.

The specific objectives of this work are to:

1. Develop insights into the GFEM enrichment process for numerical stability

of incompressible flows.

2. Assess the GFEM enrichment process such that the role of enrichments for the stability of advection-dominated problems is well understood.
3. Identify solution-tailored enrichments that demonstrate the capability of GFEM for both stable and high-accuracy solutions to fluid problems.

The remainder of this dissertation is arranged as follows: the fundamentals necessary for constructing the GFEM approximation space and system of equations are outlined in chapter 2; the GFEM for addressing locking in nearly incompressible field problems is discussed in chapter 3 along with numerical examples; the capability of the GFEM to naturally stabilize advection dominated problems is the focus of chapter 4; numerical examples applying solution-tailored enrichments for the advection-diffusion equation and Burgers' equation are shown in chapters 5 and 6, respectively; and lastly principle conclusions and suggested future work are provided in chapter 7.

1.4 Key Novel Contributions of this Dissertation

The principal contributions of this work are summarized as follows:

1. Demonstrates the GFEM combined with the penalty pressure method circumvents the LBB condition and naturally addresses challenges associated with locking in traditional finite element methods for nearly incompressible,

viscous dominated problems. This alleviation is due to the singular matrix obtained from linear dependencies of the polynomial enrichments in GFEM.

2. Several assumptions made in traditional stabilized methods are alleviated through the enrichment process in the GFEM. The result is that very few restrictions are placed on the enrichment selection process, thus allowing the choice of solution-tailored enrichments with local solution conformity.
3. Obtains stable, high-accuracy GFEM solutions using generalizable, solution-tailored, exponential, and hyperbolic tangent enrichments, which effectively capture the formation of local, steep boundary layer/shock features in the advection-diffusion equation and Burgers' equation.

Chapter 2

Methodology

This chapter covers the fundamentals necessary for constructing the GFEM approximation space and corresponding GFEM system of equations. Additional details include time discretization, initial conditions, and enforcement of Dirichlet boundary conditions.

2.1 Preliminaries

Let Ω be an open set contained in \mathbb{R}^n , $n \geq 1$, with a piecewise smooth boundary Γ . Vector and tensor fields defined on Ω are in boldface notation with lowercase and uppercase variables, respectively (e.g., vector \mathbf{y} and tensor \mathbf{A}). For prescribing boundary conditions, it is necessary to define $\Gamma = \Gamma_D \cup \Gamma_N$ such that $\Gamma_D \cap \Gamma_N = \emptyset$, where Γ_D denotes part of the boundary for prescribed Dirichlet boundary conditions, and Γ_N denotes part of the boundary for prescribed Neumann boundary conditions. The majority of the subsequent chapters considers abstract, linear,

boundary value problems of the following form: Find \mathbf{u} such that:

$$\begin{aligned}
 \mathcal{L}\mathbf{u}(\mathbf{x}, t) &= \mathbf{f}(\mathbf{x}, t) \quad \text{on } \Omega \\
 \mathbf{u}(\mathbf{x}, t) &= \mathbf{g}_{\Gamma_D}(\mathbf{x}, t) \quad \text{on } \Gamma_D \\
 \frac{\partial \mathbf{u}}{\partial \mathbf{n}}(\mathbf{x}, t) &= \mathbf{g}_{\Gamma_N}(\mathbf{x}, t) \quad \text{on } \Gamma_N \\
 \mathbf{u}(\mathbf{x}, 0) &= \mathbf{u}_0(\mathbf{x}) \quad \text{on } \Omega
 \end{aligned} \tag{2.1}$$

where \mathcal{L} is a linear differential operator on \mathbf{u} , \mathbf{f} is volumetric forcing, \mathbf{g}_{Γ_D} are prescribed Dirichlet boundary conditions, \mathbf{g}_{Γ_N} are prescribed Neumann boundary conditions, and \mathbf{u}_0 is the initial condition at $t = 0$. Note for boundary value problems where the solution is not a vector, the boldface notation is dropped (e.g., \mathbf{u} is presented as u).

In subsequent sections the weak, Galerkin, and GFEM formulation for differential equations like Eq. 2.1 is developed. These sections assume a basic understanding of the functional analysis tools necessary for developing the variational formulation of differential equations. If necessary, a thorough introduction to the functional analysis tools required for finite element methods are in [53] and for a more general introduction to functional analysis, see [54].

2.2 Weak and Galerkin Formulation

The weak formulation of the boundary value problem (Eq. 2.1), is obtained by multiplying by weighting functions \mathbf{w} and integrating over the domain Ω . The

formulation is as follows: find $\mathbf{u} \in \tilde{H}^1$ such that for all $\mathbf{w} \in \dot{H}^1$:

$$a(\mathbf{w}, \mathbf{u}) = (\mathbf{w}, \mathbf{f})_\Omega \quad \text{on } \Omega \quad (2.2)$$

where $(\cdot, \cdot)_\Omega$ is the standard inner product over the domain Ω , $a(\cdot, \cdot) = (\cdot, \mathcal{L}(\cdot))_\Omega$ is a bilinear operator, and

$$\tilde{H}^1 = \{\mathbf{u} \in H^1 \mid \mathbf{u} = \mathbf{g}_{\Gamma_D} \text{ on } \Gamma_D\} \quad (2.3)$$

and

$$\dot{H}^1 = \{\mathbf{w} \in H^1 \mid \mathbf{w} = \mathbf{0} \text{ on } \Gamma_D\} \quad (2.4)$$

where H^1 is a first order Hilbert space. The Galerkin formulation is obtained by assuming finite-dimensional approximations of the test and trial functions. That is, let \tilde{V} be a finite-dimensional subspace of the space \tilde{H}^1 , such that $\bar{\mathbf{u}} \in \tilde{V}$ is a finite-dimensional approximate solution to the weak form of the boundary value problem (Eq. 2.2). Similarly, define \dot{V} to be a finite dimensional subspace of the space \dot{H}^1 . The Galerkin formulation is as follows: Find $\bar{\mathbf{u}} \in \tilde{V}$ such that for all $\bar{\mathbf{w}} \in \dot{V}$

$$a(\bar{\mathbf{w}}, \bar{\mathbf{u}}) = (\bar{\mathbf{w}}, \mathbf{f})_\Omega \quad \text{on } \Omega \quad (2.5)$$

In the context of FEM/GFEM, subscript h will be added to the test and trial

functions such that $\bar{\mathbf{u}} = \bar{\mathbf{u}}_h$ and $\bar{\mathbf{w}} = \bar{\mathbf{w}}_h$.

2.3 GFEM Approximation Space

Construction of the GFEM approximation space consists of three components: a) patches, b) a partition of unity, c) and local approximation spaces.

a) *Patches*: build an open covering defined such that for a parameter $h > 0$,

$$\Omega \subset \bigcup_{\alpha=1}^{N(h)} \omega_{\alpha} \quad (2.6)$$

where ω_{α} are patches defined over \mathbf{x}_{α} , $\alpha = 1, \dots, N(h)$. Any $\mathbf{x} \in \Omega$ belongs to at most $M \leq N(h)$ elements of the set $\{\omega_{\alpha}\}_{\alpha=1}^{N(h)}$. In the generalized finite element method, ω_{α} is given by the union of finite elements sharing node α of the finite element mesh covering Ω . Additionally, $N(h)$ is defined to be the number of nodes in the domain Ω . Note that Fig. 2.1 provides a visual representation of patches typically used in GFEM for a one-dimensional domain.

b) *Partition of unity*: let $\{\varphi_{\alpha}\}_{\alpha=1}^{N(h)}$ be piecewise C^0 functions defined on Ω satisfying:

$$\sum_{\alpha=1}^{N(h)} \varphi_{\alpha}(\mathbf{x}) = 1, \quad \forall \mathbf{x} \in \Omega \quad (2.7)$$

Then the set $\{\varphi_{\alpha}\}_{\alpha=1}^{N(h)}$ forms a partition of unity with respect to the open cover

set $\{\omega_\alpha\}_{\alpha=1}^{N(h)}$. In the generalized finite element method, the set $\{\varphi_\alpha\}_{\alpha=1}^{N(h)}$ is typically chosen as linear, Lagrangian shape functions (see Fig. 2.1).

- c) *Local approximation spaces*: For each patch ω_α we associate an m_α -dimensional space $\chi_\alpha(\omega_\alpha)$ of functions, denoted the local approximate space, such that:

$$\chi_\alpha = \text{span}\{E_{\alpha j}, 1 \leq j \leq m_\alpha, E_{\alpha j} \in H^1\} \quad (2.8)$$

where the functions $E_{\alpha j} \in \chi_\alpha$ are known as *enrichment functions*. It is assumed each χ_α contain a constant function. The inclusion of a constant function allows for the set $\{\varphi_\alpha\}_{\alpha=1}^{N(h)}$ to be contained in the trial space.

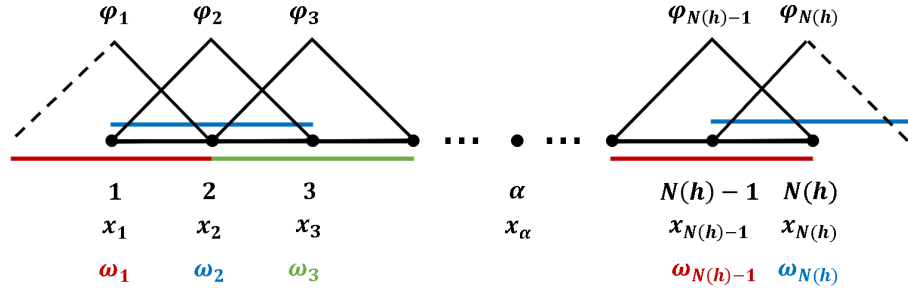


Figure 2.1: Patches (ω_α) and the partition of unity composed of linear, Lagrangian shape functions (φ_α) over a one-dimensional, uniformly discretized computational domain (Ω).

The GFEM trial space is given by:

$$S^{GFEM}(\Omega) = \text{span}\{\phi_{\alpha j} = \varphi_\alpha E_{\alpha j} \text{ (no sum over } \alpha), 1 \leq \alpha \leq N(h), 1 \leq j \leq m_\alpha\} \quad (2.9)$$

where ϕ_{α_j} are called the *GFEM shape functions*. Thus, any trial function $\mathbf{u}_h \in S^{GFEM} \subset \tilde{V}$ may be written in vector notation as:

$$\mathbf{u}_h = \begin{bmatrix} u_h \\ v_h \\ \vdots \end{bmatrix} = \begin{bmatrix} \phi_u^T \mathbf{c}_u \\ \phi_v^T \mathbf{c}_v \\ \vdots \end{bmatrix} = \boldsymbol{\phi}^T \mathbf{c} \quad (2.10)$$

where $\boldsymbol{\phi}$ is the vector of GFEM shape functions and \mathbf{c} is the vector of corresponding weighting coefficients. GFEM test functions \mathbf{w}_h are defined identically. Finally, substitution of Eq. 2.10 into Eq. 2.5 results in a system of equations of the general form:

$$\begin{aligned} \mathbf{Kc} &= \mathbf{b} \quad (\text{steady case}) \\ \mathbf{M}\dot{\mathbf{c}} + \mathbf{Kc} &= \mathbf{b} \quad (\text{unsteady case}) \end{aligned} \quad (2.11)$$

Note the system of equations in Eq. 2.11 is generalized to be inclusive of any abstract, boundary value problem (Eq. 2.1). The specific terms which make up \mathbf{M} , \mathbf{K} and \mathbf{b} depend on the differential operator, volumetric forcing, boundary conditions, and initial conditions. Subsequent chapters will provide the specific formulation of \mathbf{M} , \mathbf{K} and \mathbf{b} for: the governing equations of an elastic medium, the governing equations for a creeping flow, the advection-diffusion equation, and the Burgers' equation.

2.4 Time Discretization and Initial Conditions

For the unsteady problems presented in this dissertation, the temporal term in Eq. 2.11 is discretized using the θ -scheme, such that:

$$\mathbf{M}\left(\frac{\mathbf{c}^{n+1} - \mathbf{c}^n}{\Delta t}\right) = \theta\left[\mathbf{b}^{n+1} - \mathbf{K}^{n+1}\mathbf{c}^{n+1}\right] + (1 - \theta)\left[\mathbf{b}^n - \mathbf{K}^n\mathbf{c}^n\right] \quad (2.12)$$

where $\theta = 0$ is the forward Euler scheme, $\theta = 1$ is the backward Euler scheme, and $\theta = 0.5$ is the Crank-Nicolson scheme. The formulation in Eq. 2.12 may be condensed and presented as:

$$\tilde{\mathbf{M}}\mathbf{c}^{n+1} = \tilde{\mathbf{b}} \quad (2.13)$$

where $\tilde{\mathbf{M}} = \frac{\mathbf{M}}{\Delta t} + \theta\mathbf{K}^{n+1}$ and $\tilde{\mathbf{b}} = \frac{\mathbf{M}}{\Delta t}\mathbf{c}^n + (\theta - 1)\mathbf{K}^n\mathbf{c}^n + \theta\mathbf{b}^n + (1 - \theta)\mathbf{b}^{n+1}$.

Solution of the above system of equations requires an initial solution vector, \mathbf{c}^0 . To obtain the initial solution vector, \mathbf{c}^0 , the following initial value problem is solved:

$$\mathbf{u}_h(\mathbf{x}, 0) = \boldsymbol{\phi}^T(\mathbf{x})\mathbf{c}^0 \approx \mathbf{u}_0(\mathbf{x}). \quad (2.14)$$

The degrees of freedom are obtained by solving the Galerkin formulation of Eq. 2.14, following the same methodology presented in section 2.2.

2.5 Enforcing Dirichlet Boundary Conditions

In the Lagrangian finite element method, the Kronecker delta property of the shape functions allows the direct enforcement of Dirichlet boundary conditions by setting the coefficients equal to the desired solution values. However, the addition of enrichments in the GFEM formulation results in multiple degrees of freedom per node, making this approach nontrivial. For one-dimensional problems that have enrichments shifted by nodal values, Dirichlet boundary conditions may be enforced by following the traditional approach of subtracting out columns of the matrix that correspond to the boundary. Specifically, by defining enrichments $E_{\alpha j}$ such that $E_{\alpha j}(\mathbf{x}_\alpha) = 0$, the only active functions on the one-dimensional boundary (Γ_D) are the finite element shape functions (φ_α), thus allowing direct enforcement of the boundary conditions through the FEM degrees of freedom. For dimensions, $n \geq 2$, the FEM degrees of freedom are still directly enforceable if using shifted enrichments. However, the GFEM shape functions ($\phi_{\alpha j}$) are typically nonzero in between nodes on the domain boundary (Γ_D). For these GFEM degrees of freedom, a penalty approach may be adopted to enforce Dirichlet boundary conditions. Specifically, to enforce desired Dirichlet boundary conditions in GFEM, add a penalty term to both sides of the matrix form (Eq. 2.11 for steady problems, or Eq. 2.13 for unsteady problems) such that:

$$\begin{aligned}
(\mathbf{K} + \mathbf{M}_{\Gamma_D})\mathbf{c} &= \mathbf{b} + \mathbf{b}_{\Gamma_D} \quad (\text{steady case}) \\
(\tilde{\mathbf{M}} + \mathbf{M}_{\Gamma_D})\mathbf{c}^{n+1} &= \tilde{\mathbf{b}} + \mathbf{b}_{\Gamma_D} \quad (\text{unsteady case})
\end{aligned} \tag{2.15}$$

where

$$\mathbf{M}_{\Gamma_D} = \beta(\boldsymbol{\phi}, \boldsymbol{\phi})_{\Gamma_D} \tag{2.16}$$

$$\mathbf{b}_{\Gamma_D} = \beta(\boldsymbol{\phi}, \mathbf{g}_{\Gamma_D})_{\Gamma_D} \tag{2.17}$$

and β is the penalty parameter that is typically very large in relation to the other matrix components contained in \mathbf{K} and $\tilde{\mathbf{M}}$. For a sufficiently large β , Dirichlet boundary conditions may be accurately enforced. Note that because of the linear dependencies of the GFEM formulation when using polynomial enrichments (see [55]), the iterative algorithm presented in [56] and displayed in Algo. 1 is used to solve the potentially indefinite system of equations. For the subsequent numerical examples contained in chapters 3-6 $\epsilon_1 = \epsilon_2 = 10^{-10}$ is used.

Algorithm 1: Solution to the system of equations $\tilde{\mathbf{A}}\tilde{\mathbf{c}} = \tilde{\mathbf{b}}$

INPUT: $\tilde{\mathbf{A}}, \tilde{\mathbf{b}}$, perturbation $\epsilon_1 \ll 1$, and criterion $\epsilon_2 \ll 1$ **OUTPUT:** $\tilde{\mathbf{c}} = \mathbf{c}_i$

Initialization:

Precondition $\tilde{\mathbf{A}}\tilde{\mathbf{c}} = \tilde{\mathbf{b}}$ to equivalent system $\mathbf{A}\mathbf{c} = \mathbf{b}$ by defining:

$$T_{ij} = \frac{\delta_{ij}}{\sqrt{\tilde{A}_{ij}}}$$

$$\mathbf{A} = \mathbf{T}\tilde{\mathbf{A}}\mathbf{T}$$

$$\mathbf{c} = \mathbf{T}^{-1}\tilde{\mathbf{c}}$$

$$\mathbf{b} = \mathbf{T}\tilde{\mathbf{b}}$$

Perturbed matrix: $\mathbf{A}_\epsilon = \mathbf{A} + \epsilon_1\mathbf{I}$;Approximate system of equations solution vector: $\mathbf{c}_0 = \mathbf{A}_\epsilon^{-1}\mathbf{b}$;Residual error of approximate system of equations: $\mathbf{r}_0 = \mathbf{b} - \mathbf{A}\mathbf{c}_0$;Residual error of solution vector: $\mathbf{e}_0 = \mathbf{c} - \mathbf{c}_0 \approx \mathbf{A}_\epsilon^{-1}\mathbf{r}_0$;

while $\left| \frac{e_i A e_i}{c_i A c_i} \right| > \epsilon_2$ **do**

$\mathbf{r}_i = \mathbf{r}_{i-1} - \sum_{j=0}^{i-1} \mathbf{A}\mathbf{e}_j$
$\mathbf{e}_i = \mathbf{A}_\epsilon^{-1}\mathbf{r}_i$
$\mathbf{c}_i = \mathbf{c}_0 + \sum_{j=0}^{i-1} \mathbf{e}_j$

end**return** $\tilde{\mathbf{c}} = \mathbf{T}\mathbf{c}_i$

Chapter 3

Nearly Incompressible Field Problems

This chapter focuses on developing the GFEM formulation for Stokes flow, a regime where viscous forces are dominant compared to inertial terms. The governing equations for Stokes flow lead to a class of formulations referred to as saddle-point problems, which require Galerkin finite element methods to satisfy the LBB condition. In this chapter, using the penalty pressure method circumvents the LBB condition. The penalty pressure method introduces slight compressibility to the Stokes equations through the use of a penalty parameter. Typically, the challenge of this approach is locking. However, it is shown in a subsequent section that the GFEM formulation naturally alleviates challenges associated with locking. Additionally, implementation of the penalty pressure method to Stokes flow results in equations of equivalent form to elasticity equations for incompressible materials. Thus, this work explores the application of GFEM to incompressible field problems in general.

The remaining outline of this chapter is as follows: First, the governing equa-

tions for an elastic medium are presented, followed by the specific GFEM matrix formulation for the two-dimensional case. Next, the effect of locking in the incompressible limit is discussed along with the GFEM enrichment process to address this challenge naturally. Stokes flow using a penalty pressure method is then discussed, along with its form equivalence to the elasticity equations. Lastly, GFEM solutions of a two-dimensional elasticity equation with a variable Poisson's ratio and a two-dimensional lid-driven cavity Stokes flow are presented, followed by a general discussion of the results.

3.1 Boundary Value Problem: Linear Elasticity

3.1.1 Governing Equations

The governing equations for an elastic medium in \mathbb{R}^n are:

$$\begin{aligned} \mu \Delta \mathbf{u} + (\mu + \lambda) \nabla (\nabla \cdot \mathbf{u}) + \mathbf{f} &= \mathbf{0} \quad \text{on } \Omega \\ \mathbf{u} &= \mathbf{g}_{\Gamma_D} \quad \text{on } \Gamma_D \\ \frac{\partial \mathbf{u}}{\partial \mathbf{n}} &= \mathbf{g}_{\Gamma_N} \quad \text{on } \Gamma_N \end{aligned} \tag{3.1}$$

where \mathbf{u} is the displacement field, \mathbf{f} is the volumetric forcing vector, and μ and λ are the first and second Lamé parameters, respectively. Further defining Lamé parameters in terms of Young's modulus, E , and Poisson's ratio, ν , gives:

$$\mu = \frac{E}{2(1 + \nu)} \quad \lambda = \frac{E\nu}{(1 + \nu)(1 - 2\nu)} \quad (3.2)$$

As Poisson's ratio, ν , approaches 0.5, the material becomes increasingly incompressible. For the limiting case of $\nu = 0.5$, an exact solution \mathbf{u} must satisfy the constraint:

$$\nabla \cdot \mathbf{u} \approx 0 \quad (\text{nearly incompressible, } \nu \approx 0.5) \quad (3.3)$$

$$\nabla \cdot \mathbf{u} = 0 \quad (\text{incompressible limit, } \nu = 0.5)$$

The imposition of Eq. 3.3 on a numerical approximation is what leads to locking.

3.1.2 Matrix Formulation

Substituting the GFEM approximation space Eq. 2.10 into the Galerkin formulation of Eq. 3.1 results in the following system of equations for a 2D problem:

$$\mathbf{Kc} = \mathbf{b} \rightarrow \begin{bmatrix} \mathbf{K}_u & \mathbf{C}_{uv} \\ (\mathbf{C}_{uv})^T & \mathbf{K}_v \end{bmatrix} \begin{bmatrix} \mathbf{c}_u \\ \mathbf{c}_v \end{bmatrix} = \begin{bmatrix} \mathbf{f}_u \\ \mathbf{f}_v \end{bmatrix} \quad (3.4)$$

where:

$$\mathbf{K}_u = \mu \int_{\Omega} \left(\frac{\partial \phi_u}{\partial x} \frac{\partial \phi_u^T}{\partial x} + \frac{\partial \phi_u}{\partial y} \frac{\partial \phi_u^T}{\partial y} \right) d\Omega + (\mu + \lambda) \int_{\Omega} \left(\frac{\partial \phi_u}{\partial x} \frac{\partial \phi_u^T}{\partial x} \right) d\Omega \quad (3.5)$$

$$\mathbf{K}_v = \mu \int_{\Omega} \left(\frac{\partial \phi_v}{\partial x} \frac{\partial \phi_v^T}{\partial x} + \frac{\partial \phi_v}{\partial y} \frac{\partial \phi_v^T}{\partial y} \right) d\Omega + (\mu + \lambda) \int_{\Omega} \left(\frac{\partial \phi_v}{\partial y} \frac{\partial \phi_v^T}{\partial y} \right) d\Omega \quad (3.6)$$

$$\mathbf{C}_{uv} = (\mu + \lambda) \int_{\Omega} \left(\frac{\partial \phi_u}{\partial x} \frac{\partial \phi_v^T}{\partial y} \right) d\Omega \quad (3.7)$$

$$\mathbf{f}_u = \int_{\Omega} \phi_u^T f_1 d\Omega \quad (3.8)$$

$$\mathbf{f}_v = \int_{\Omega} \phi_v^T f_2 d\Omega \quad (3.9)$$

Recall that for nearly incompressible problems, the Poisson's ratio, ν , approaches a value of 0.5. In return, Lamé's first parameter, λ , tends toward ∞ . From Eq. 3.4, we may write:

$$\begin{bmatrix} \mathbf{K}_u & \mathbf{C}_{uv} \\ (\mathbf{C}_{uv})^T & \mathbf{K}_v \end{bmatrix} = \begin{bmatrix} \mathbf{K}_u & \mathbf{C}_{uv} \\ (\mathbf{C}_{uv})^T & \mathbf{K}_v \end{bmatrix}_{\mu} + \begin{bmatrix} \mathbf{K}_u & \mathbf{C}_{uv} \\ (\mathbf{C}_{uv})^T & \mathbf{K}_v \end{bmatrix}_{\lambda} \quad (3.10)$$

where matrices $[\cdot]_{\mu}$ and $[\cdot]_{\lambda}$ are proportional to μ and λ , respectively. It is evident that if matrix $[\cdot]_{\lambda}$ is nonsingular, then as $\lambda \rightarrow \infty$, the corresponding displacements $\mathbf{u}_h \rightarrow \mathbf{0}$ for any homogeneous Dirichlet boundary condition problem. Further details on the requirements of a singular matrix in order to obtain non-trivial solutions for problems involving internal constraints (i.e., incompressible materials) can be found in most standard finite element textbooks, for instance, by Hughes [57], Cook [58], Donea and Huerta [59], and Onate [60]. Standard Lagrangian finite

element shape functions result in a non-singular, constrained matrix for this term when using exact integration [41]. For standard finite element methods, alleviation of this locking phenomena is possible by introducing a singular matrix through selective reduced integration as detailed, for instance in [61]. In the GFEM context, the enrichment process using polynomials is well-known to result in linear dependencies in the shape functions [56, 62–64], resulting in a singular matrix.

3.2 Boundary Value Problem: Stokes Flow

3.2.1 Governing Equations and the Penalty Pressure Method

The equations for a creeping flow, where viscous forces dominate over the advective inertial forces, are denoted as Stokes equations and are given by:

$$\begin{aligned}
 \Delta \mathbf{u} - \nabla p + \mathbf{f} &= \mathbf{0} \quad \text{on } \Omega \\
 \nabla \cdot \mathbf{u} &= 0 \quad \text{on } \Omega \\
 \mathbf{u} &= \mathbf{g}_{\Gamma_D} \quad \text{on } \Gamma_D \\
 \frac{\partial \mathbf{u}}{\partial \mathbf{n}} &= \mathbf{g}_{\Gamma_N} \quad \text{on } \Gamma_N
 \end{aligned} \tag{3.11}$$

where \mathbf{u} is the velocity field, and p is the pressure. Note Stokes flow is characterized by a low Reynold's number ($\text{Re} \ll 1$). This Reynold's number does not appear explicitly in the normalized equations (Eq. 3.11).

The penalty pressure method aims to alleviate challenges encountered in the

saddle-point problem (Ref. [29]) Eq. 3.11 by approximating pressure as:

$$p = -\frac{1}{\epsilon} \nabla \cdot \mathbf{u} \quad (3.12)$$

where ϵ is the penalty pressure parameter. Substitution of Eq. 3.12 into the original Stokes flow equations (Eq. 3.11) results in the following set of equations:

$$\begin{aligned} \Delta \mathbf{u} + \frac{1}{\epsilon} \nabla (\nabla \cdot \mathbf{u}) + \mathbf{f} &= \mathbf{0} \quad \text{on } \Omega \\ \mathbf{u} &= \mathbf{g}_{\Gamma_D} \quad \text{on } \Gamma_D \\ \frac{\partial \mathbf{u}}{\partial \mathbf{n}} &= \mathbf{g}_{\Gamma_N} \quad \text{on } \Gamma_N \end{aligned} \quad (3.13)$$

It can immediately be observed that the penalty pressure method applied to Stokes flow (Eq. 3.13) is form identical to the elasticity equations (Eq. 3.1). It should be noted that $\frac{1}{\epsilon}$ is analogous to the first Lamé parameter, λ , which approaches ∞ for nearly incompressible problems. Thus the penalty pressure parameter term, ϵ , is chosen to be small. Convergence of the solution of the penalty-pressure formulation Eq. 3.1 to the Stokes flow solution Eq. 3.11 is proved in [66]. The GFEM matrices for this boundary-value problem are excluded, as they are identical to that of the elasticity equations (Eq. 3.5) with different material coefficients.

3.2.2 A Note on Locking

It is important to note that there exist specific conditions under which the effect of locking is negligible for numerical solution to the field equations 3.1, 3.11. Recall

in the incompressible limit that λ and $\frac{1}{\epsilon} \rightarrow \infty$. If the matrix corresponding to these terms is non-singular, the numerical approximation is essentially solving the following Galerkin problem: find $\mathbf{u}_h \in \tilde{\mathbf{V}}$ such that for all $\mathbf{w}_h \in \dot{\mathbf{V}}$

$$\int_{\Omega} (\nabla \cdot \mathbf{w}_h)(\nabla \cdot \mathbf{u}_h) d\Omega = \mathcal{O}\left(\frac{\mu}{\lambda}, \epsilon\right) \approx 0 \quad (3.14)$$

The corresponding strong formulation results in the following boundary value problem: find $\mathbf{u} \in \mathbb{R}^n$ such that:

$$\begin{aligned} \nabla(\nabla \cdot \mathbf{u}) &\approx \mathbf{0} \quad \text{on } \Omega \\ \mathbf{u} &= \mathbf{g}_{\Gamma_D} \quad \text{on } \Gamma_D \\ \frac{\partial \mathbf{u}}{\partial \mathbf{n}} &= \mathbf{g}_{\Gamma_N} \quad \text{on } \Gamma_N \end{aligned} \quad (3.15)$$

That is, locking results in numerical approximation of the boundary value problem Eq. 3.15, as opposed to Eqns. 3.1, 3.11. Through comparison, conditions for which the solution to Eq. 3.15 is equivalent to the solution in Eqns. 3.1, 3.11 are obtained. Specifically for problems not subject to volumetric forcing (i.e. $\mathbf{f} = \mathbf{0}$), field solutions of the following form are solvable:

$$\begin{aligned} u &= a_1x + a_2y + a_3 \\ v &= b_1x + b_2y + b_3 \end{aligned} \quad (3.16)$$

where a_n, b_n are arbitrary constants. Solutions of this form are trivial solutions to Eqns. 3.1, 3.11, and thus real world application is severely limited and often unnec-

essary. It should be noted that in the case of real world application, the additional requirement that $\nabla \cdot \mathbf{u} \rightarrow 0$ as the solution field approaches the incompressible limit will result in $a_1 = -b_2$. The subsequent section focuses on the GFEM solution of two nontrivial example problem: (1) the two-dimensional, nearly incompressible elasticity equations with volumetric forcing, and (2) a two-dimensional lid-driven cavity problem.

3.3 Numerical Results

3.3.1 2D Elasticity Equations with Volumetric Forcing

First consider the 2D elasticity equations (Eq. 3.1). The problem is defined over a unit square domain and subject to homogeneous Dirichlet boundary conditions everywhere ($\mathbf{g}_{\Gamma_D} = 0$) as shown in Fig. 3.1. Using the method of manufactured solutions [67], the analytical displacement fields (shown in Fig. 3.1) are chosen as:

$$\begin{aligned} u &= \sin 2\pi y (\cos 2\pi x - 1) + \frac{\sin \pi x \sin \pi y}{1 + \lambda} \\ v &= \sin 2\pi x (1 - \cos 2\pi y) + \frac{\sin \pi x \sin \pi y}{1 + \lambda} \end{aligned} \quad (3.17)$$

and the corresponding volumetric forcing terms are:

$$\mathbf{f} = -\pi^2 \begin{bmatrix} \left(\frac{\lambda + \mu}{\lambda + 1} \right) \cos \pi(x + y) - \mu \left(\sin 2\pi y (8 \cos 2\pi x - 4) + \frac{2 \sin \pi x \sin \pi y}{\lambda + 1} \right) \\ \left(\frac{\lambda + \mu}{\lambda + 1} \right) \cos \pi(x + y) - \mu \left(\sin 2\pi x (4 - 8 \cos 2\pi y) + \frac{2 \sin \pi x \sin \pi y}{\lambda + 1} \right) \end{bmatrix} \quad (3.18)$$

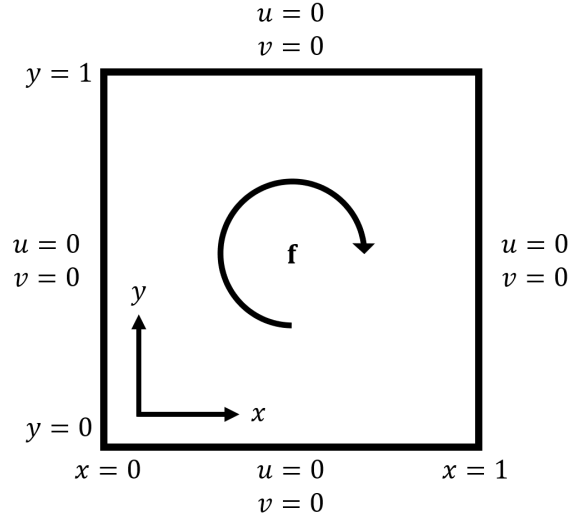


Figure 3.1: Domain (Ω) and Dirichlet boundary conditions ($\mathbf{u} = \mathbf{g}_{\Gamma_D}$) for the elasticity problem.

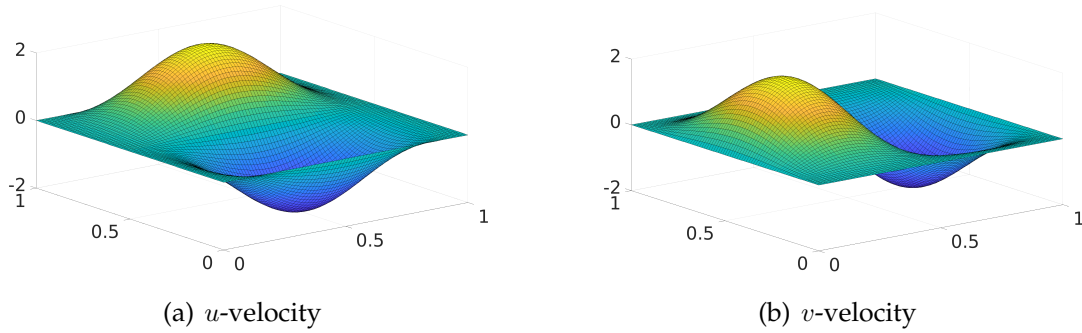


Figure 3.2: Reference solution (\mathbf{u}) for the elasticity problem.

Clearly as $\lambda \rightarrow \infty$, the solution becomes divergent-free (i.e. $\nabla \cdot \mathbf{u} \rightarrow 0$). This problem is solved over uniform grids ($h = \left[\frac{1}{5}, \frac{1}{10}, \frac{1}{20}, \frac{1}{30}, \frac{1}{40}, \frac{1}{60}, \frac{1}{80} \right]$) using bilinear and quadratic Lagrangian FEM with and without reduced integration, as well as a bilinear Lagrangian FEM enriched with linear and quadratic polynomial enrichments, resulting in quadratic and cubic approximation spaces, using full integration. The local approximation space for GFEM is defined as:

$$\chi_\alpha = \text{span} \left\{ 1, \frac{x - x_\alpha}{h}, \frac{y - y_\alpha}{h}, \frac{(x - x_\alpha)^2}{h^2}, \frac{(y - y_\alpha)^2}{h^2} \right\} \quad (3.19)$$

Note that a quadratic GFEM solution uses only the first three elements of the set in Eq. 3.19, whereas a cubic solution uses the complete set. A Young's modulus of $E = 1500$ is used, and a material Poisson's ratio of $\nu = [0.3, 0.4, 0.49, 0.499, 0.4999, 0.49999]$ is used to assess locking as the domain approaches the incompressible limit. The corresponding values of the Lamé parameters (Eq. 3.2) are shown in Table 3.1, which demonstrates the increasing value of λ as the incompressible limit is approached. The convergence of the energy norm for various Poisson's ratios are shown Fig. 3.3. The actual convergence rate of the two finest grids studied is present for each of the cases. Theoretical convergence rates are 0.5 (linear), 1.0 (quadratic), and 1.5 (cubic). The quadratic FEM and quadratic GFEM solutions without reduced integration return similar errors, except GFEM does so at fewer DOFs. As expected, since 0.3 and 0.4 are well below the incompressible limit of 0.5, all polynomial orders converge optimally. However, as ν increases to 0.499, the linear FEM begins to show signs of locking. In the most extreme case of $\nu = 0.49999$, linear FEM is essentially completely locked and yields poor solution accuracy, returning errors of 93% for 80×80 elements. The quadratic GFEM solution correspondingly yields sub-optimal convergence but returns errors of 3.3% at the same number of degrees of freedom. As the order of the GFEM solution increases to cubic, the result is optimal convergence with returned errors of 0.77%. The linear and

quadratic FEM with reduced integration return errors of 2.5% and 0.1%, respectively. As Poisson’s ratio approaches 0.5, a shift in the constant for the error in the energy norm is apparent for all solutions without reduced integration. However, the increased convergence rates offered by the higher-order methods eventually surpass the reduced integration schemes even with this shift present. Absolute error contours of the computed displacement fields \mathbf{u}_h are shown in Figs. 3.4 - 3.5 for the finest grid size of 80×80 elements and $\nu = 0.49999$. By comparing the scales of the contours, it is evident that all high-order solutions or solutions using reduced integration compare favorably to the reference solution over the entire domain. In contrast, linear FEM captures the shape of the solution but is off by several orders of magnitude.

Table 3.1: Lamé parameters (μ, λ) for $E = 1500$ and ν

ν	μ	λ
0.3	5.769×10^2	8.654×10^2
0.4	5.357×10^2	2.143×10^3
0.49	5.034×10^2	2.466×10^4
0.499	5.003×10^2	2.497×10^5
0.4999	5.000×10^2	2.500×10^6
0.49999	5.000×10^2	2.500×10^7

3.3.2 2D Stokes Flow: Lid-Driven Cavity Problem

The second problem of interest is the lid-driven cavity problem defined over a unit domain with the top wall moving in the x -direction with a velocity given in Fig. 3.6. The choice of these boundary conditions is such that no singularities

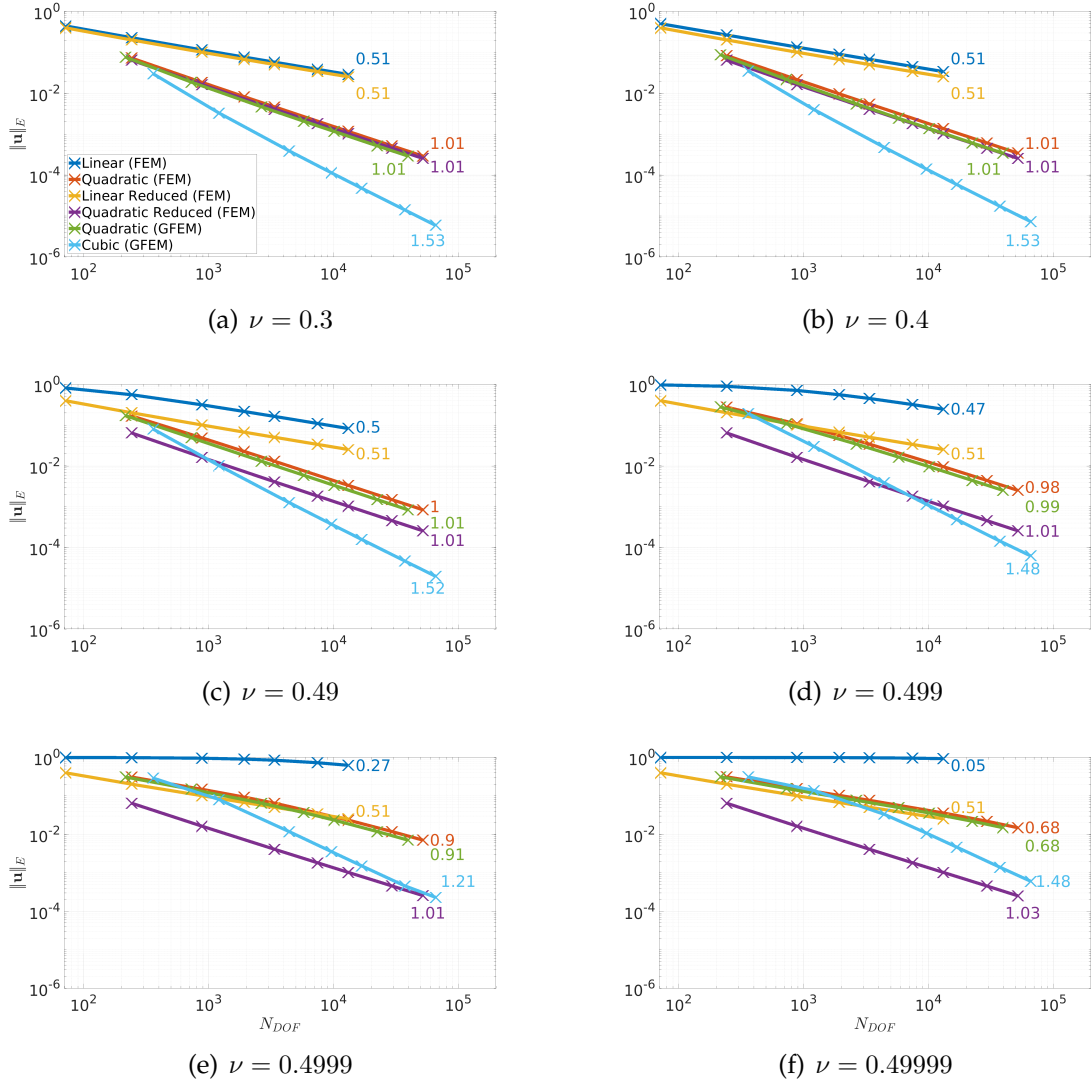


Figure 3.3: Energy norms ($\|\mathbf{u}\|_E$) over a range of Poisson's ratio (ν).

are present in either the solution or gradient fields. The used penalty pressure parameter is $\epsilon = 10^{-5}$. Note this value is equivalent to an elasticity problem with Young's modulus of $E = 2.99999$ and Poisson's ratio of $\nu = 0.499995$. No analytical solution is available, so an extrapolation strategy for the strain energy of the system is used (see [68]). Specifically, the theoretical error estimate is given by:

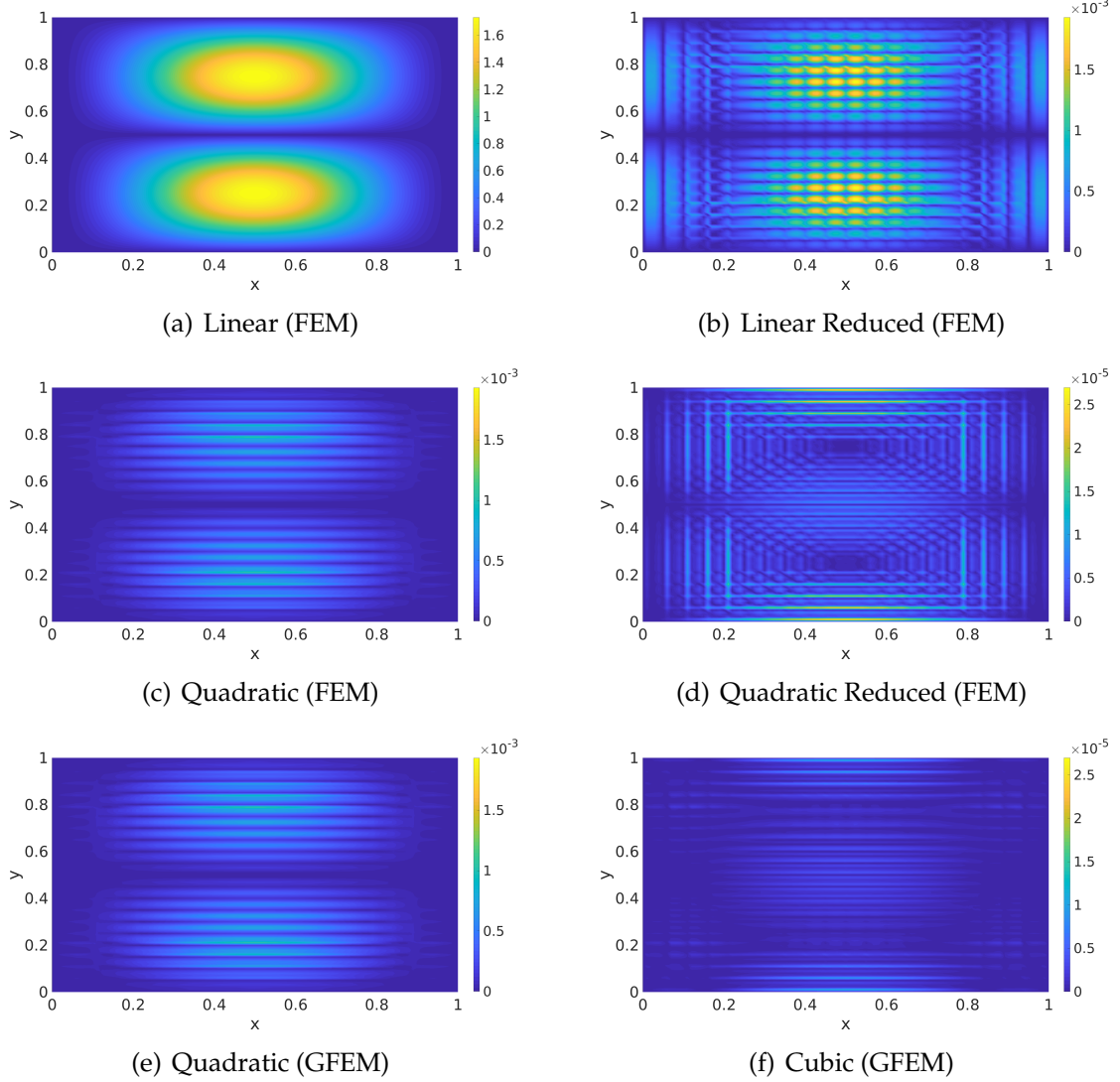


Figure 3.4: u -displacement absolute error contours ($|u - u_h|$) for $\nu = 0.49999$ over an 80×80 element grid.

$$\|U - U_h\| = \sqrt{U - U_h} = Ch^{\frac{p}{n}} \quad (3.20)$$

where h is the element size, p is the polynomial order of the approximation, n is the number of dimensions, and C is an arbitrary constant. Consider the known

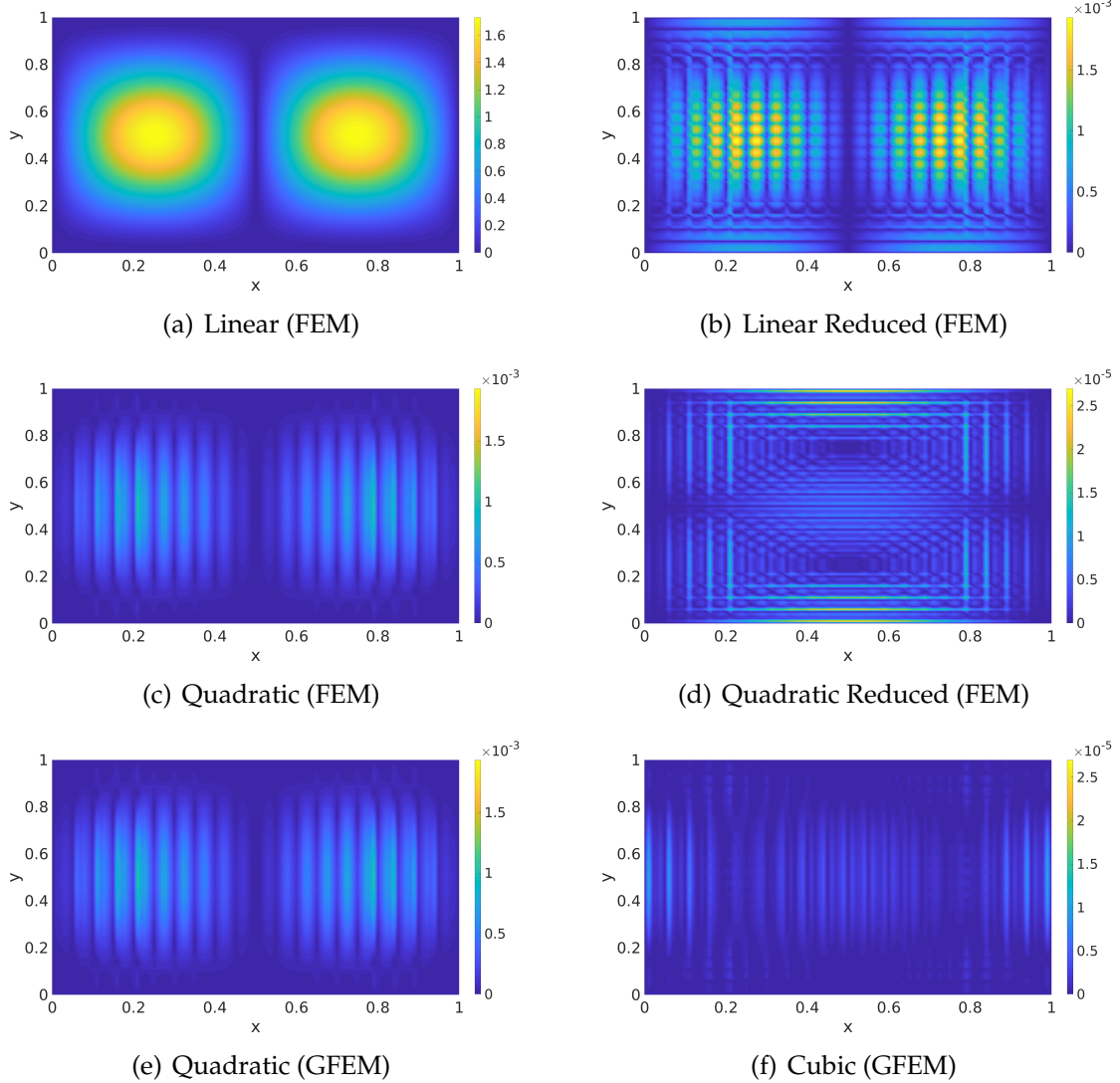


Figure 3.5: v -displacement absolute error contours ($|v - v_h|$) for $\nu = 0.49999$ over an 80×80 element grid.

strain energies, U_{h_0} , U_{h_1} , and U_{h_2} , and their corresponding grid sizes h_0 , h_1 , and h_2 .

The following three equations are obtained through substitution into Eq. 3.20:

$$\begin{aligned}
(a) : \quad \|U - U_{h_0}\| &= \sqrt{U - U_{h_0}} = Ch_0^{\frac{p}{2}} \\
(b) : \quad \|U - U_{h_1}\| &= \sqrt{U - U_{h_1}} = Ch_1^{\frac{p}{2}} \\
(c) : \quad \|U - U_{h_2}\| &= \sqrt{U - U_{h_2}} = Ch_2^{\frac{p}{2}}
\end{aligned} \tag{3.21}$$

Taking $\frac{\log \frac{(a)}{(b)}}{\log \frac{(b)}{(c)}}$ from Eq. 3.21 and simplifying results in the following nonlinear equation:

$$f(U) = \log \left(\frac{U - U_{h_0}}{U - U_{h_1}} \right) - \frac{\log \left(\frac{h_0}{h_1} \right)}{\log \left(\frac{h_1}{h_2} \right)} \log \left(\frac{U - U_{h_1}}{U - U_{h_2}} \right) = 0 \tag{3.22}$$

Thus, by solving for the roots of Eq. 3.22, the exact strain energy U can be estimated using known values. The known values used were obtained from quadratic FEM using reduced integration over grid sizes of 60×60 , 70×70 , and 80×80 elements ($h = \frac{1}{60}, \frac{1}{70}, \frac{1}{80}$, respectively). The resulting reference strain energy is $U = 16893.71040039219$. An example velocity field is shown in Fig. 3.7, using a 160×160 cubic GFEM solution.

Similar to the first example, this problem is solved over uniform grids ($h = \left[\frac{1}{10}, \frac{1}{20}, \frac{1}{30}, \frac{1}{40}, \frac{1}{50}, \frac{1}{60}, \frac{1}{70}, \frac{1}{80} \right]$) using linear and quadratic Lagrangian FEM with and without reduced integration, as well as GFEM using linear and quadratic polynomial enrichment. The convergence of the energy norm versus the total number of degrees of freedom is shown in Fig. 3.8. The true convergence rate of the two finest grids studied is present for each of the cases. Theoretical convergence rates are 0.5 (linear), 1.0 (quadratic), and 1.5 (cubic). The high error levels of the linear

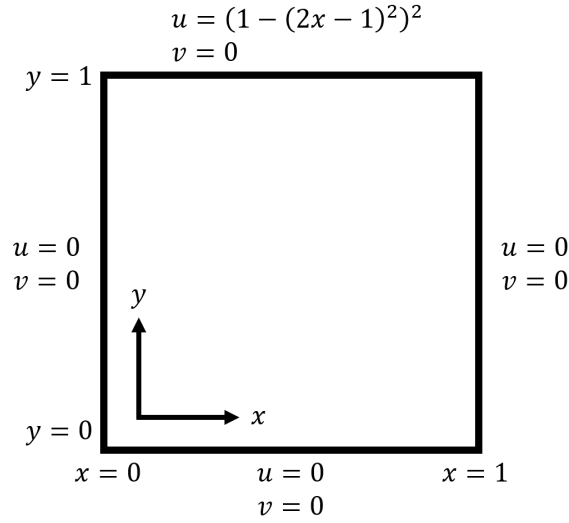


Figure 3.6: Domain (Ω) and Dirichlet boundary conditions ($\mathbf{u} = \mathbf{g}_{\Gamma_D}$) for the lid-driven cavity problem.

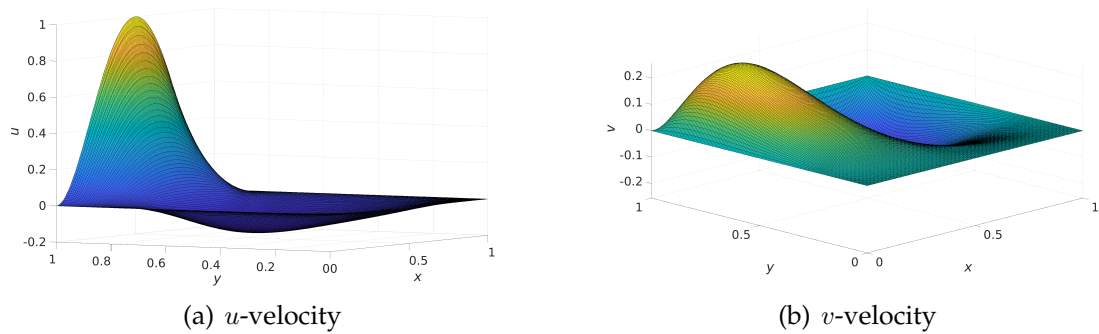


Figure 3.7: Lid-driven cavity velocity field (\mathbf{u}) for 160×160 cubic GFEM solution.

FEM arise from a combination of locking and direct enforcement of the Dirichlet boundary conditions. That is, linear FEM converges optimally over Γ_D due to direct enforcement of boundary conditions, however the effect of locking leads to poor solution convergence in the interior domain Ω . The result is errors of 385% at a grid size of 80×80 elements. Similar to the first example, the quadratic GFEM solution correspondingly yields suboptimal convergence, but returns errors of 4.0%

at the same number of degrees of freedom. As the order of the GFEM solution is increased to cubic, optimal convergence is maintained, and errors of 1.9% are returned. The linear and quadratic FEM with reduced integration return errors of 0.57% and 0.055%, respectively. Absolute error contours of the computed displacement fields \mathbf{u}_h are shown in Figs. 3.9 - 3.10 for the finest grid size of 80×80 elements and $\nu = 0.49999$. By comparing the scales of the contours, it is evident that all high-order solutions or solutions using reduced integration compare favorably to the reference solution over the entire domain. In contrast, linear FEM fails to capture the shape of the reference solution in Ω even when accurately enforcing boundary conditions.

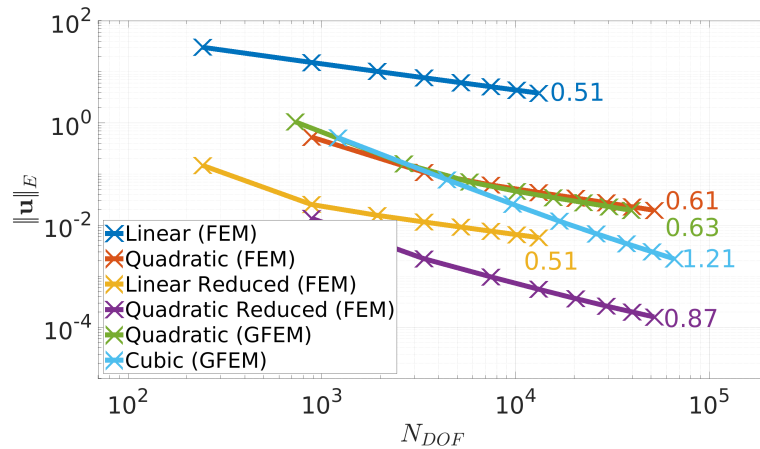


Figure 3.8: Energy norm ($\|\mathbf{u}\|_E$) versus total degrees of freedom (N_{DOF}) for lid-driven cavity problem.

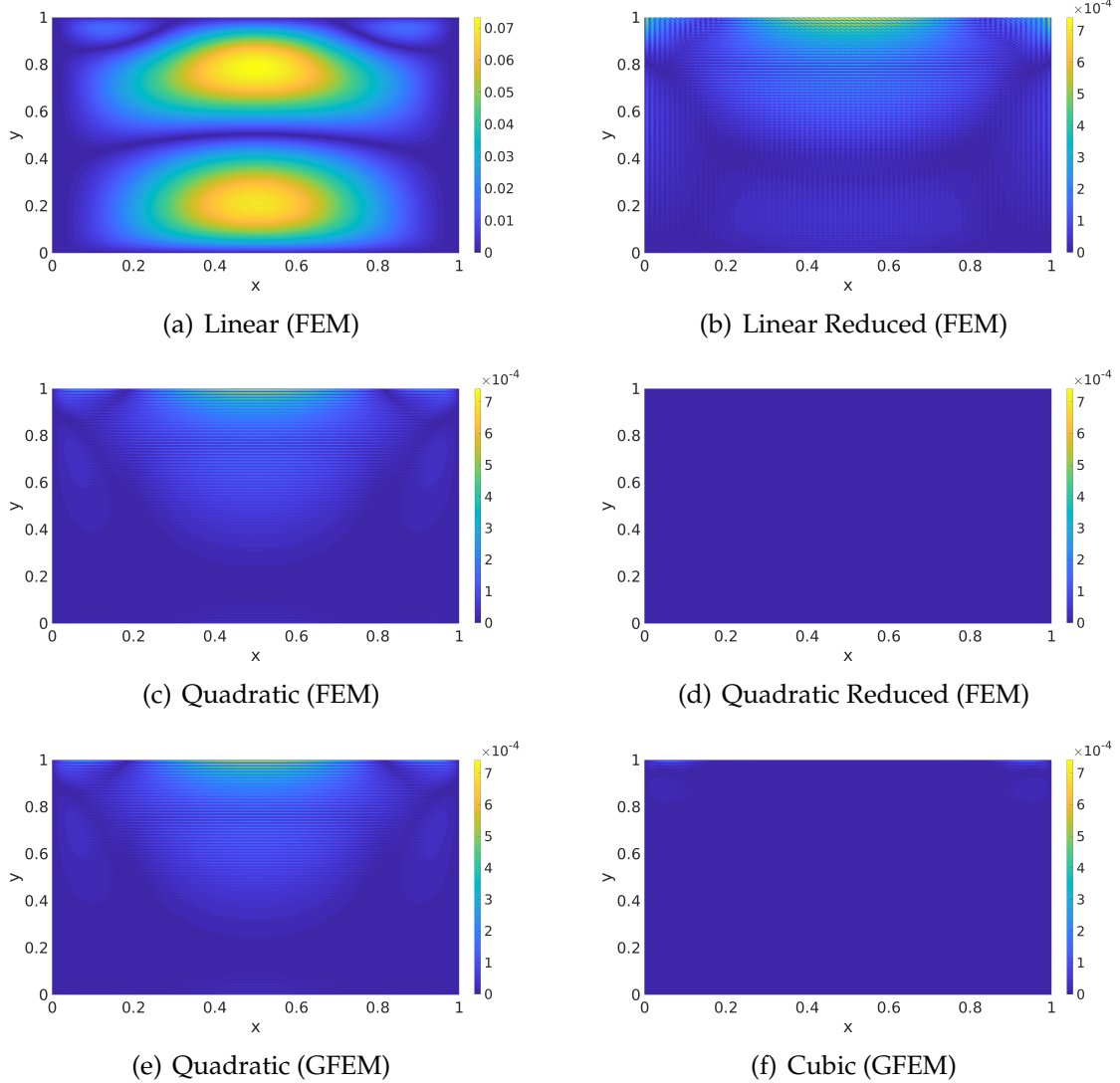


Figure 3.9: u -displacement absolute error contours ($|u - u_h|$) over an 80×80 element grid.

3.4 General Discussion

In this chapter, GFEM formulation for nearly incompressible field problems is examined and compared to traditional FEM formulations. Quadratic and cubic GFEM solutions compared against Lagrangian FEM -both with and without re-

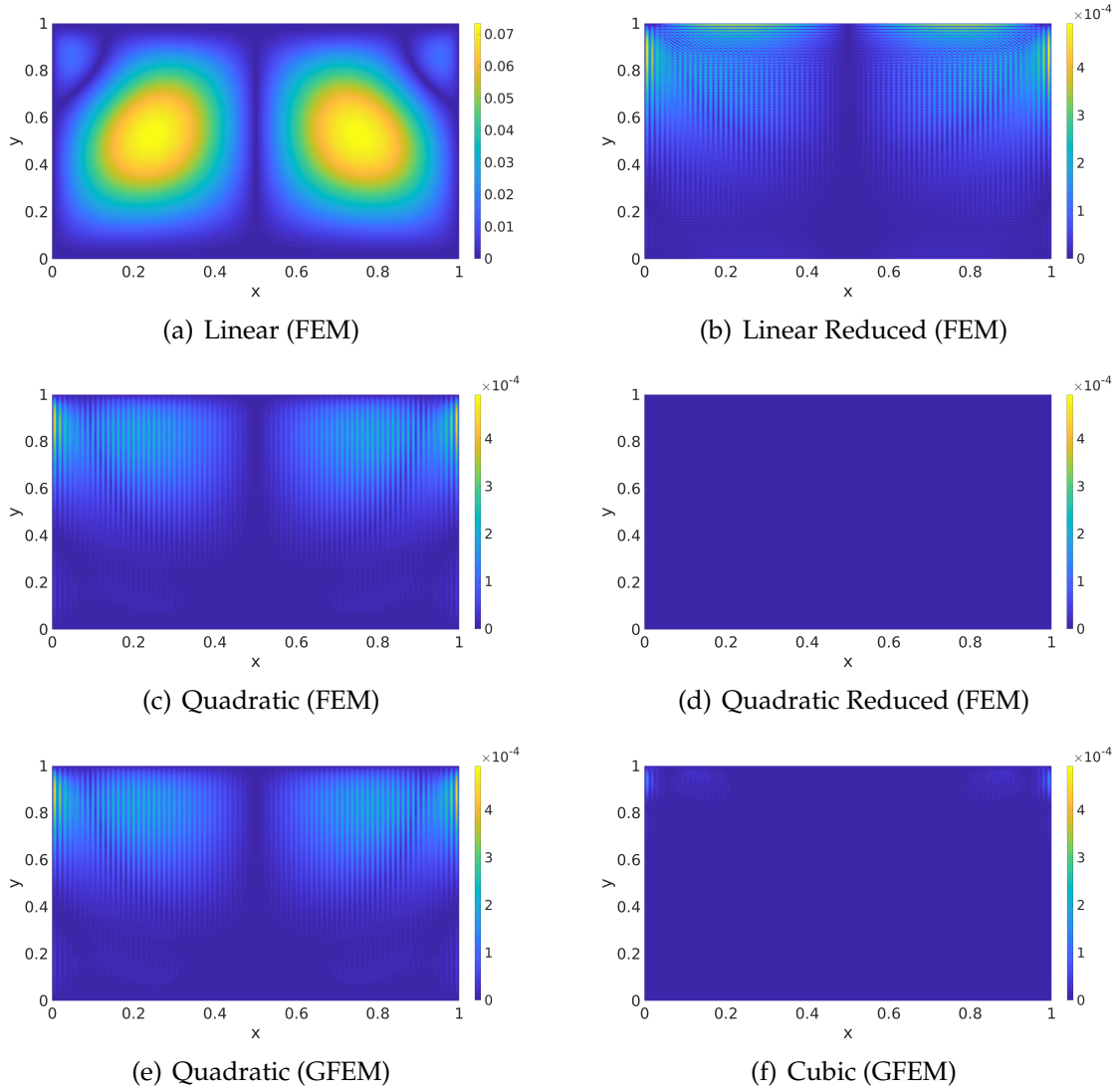


Figure 3.10: v -displacement absolute error contours ($|v - v_h|$) over an 80×80 element grid.

duced integration - for 2D nearly incompressible elasticity equations driven by volumetric forcing and 2D Stokes flow of a lid-driven cavity yield the following conclusions:

1. Consistent with higher-order Lagrangian elements, the use of polynomial enrichments in the GFEM significantly improves convergence relative to linear

FEM in the incompressible limit.

2. Optimal convergence is noted in the 2D nearly incompressible elasticity problem for quadratic GFEM up to a Poisson's ratio of $\nu = 0.499$, and for cubic GFEM at least up to Poisson's ratio of $\nu = 0.49999$. The Stokes flow example ran closer to the incompressible limit, with observed degradation in the convergence rates for each high-order solution considered. Cubic GFEM yielded between 1.4 - 2 times the convergence rate of quadratic Lagrangian FEM and quadratic GFEM.
3. Both GFEM and Lagrangian FEM experience a shift in the energy norm values when approaching the incompressible limit. This shift is not present in the reduced integration schemes of the Lagrangian FEM. However, this shift is ultimately overcome with cubic GFEM by grid refinement.

Chapter 4

Stabilization of Advection Dominated Problems

The previous chapter focused on GFEM solutions to Stokes flow and the form equivalent elasticity equations. Stokes flow represents a regime where viscous forces dominate the advective inertial forces, and the previous chapter shows that the GFEM is well-suited to naturally address stability concerns in this regime. For the remainder of this work, a shift to the other extreme will be the focus. That is problems where advective inertial forces dominate over the viscous forces. Traditional finite element approaches are well-known to introduce spurious oscillations when applied to advection-dominated problems. This chapter explores alleviation of this issue from the perspective of GFEM, which enables the stabilization of a linear differential operator through enrichments based on fundamental solutions. Improvements offered by the GFEM enrichment process are illuminated through a consistent decomposition of the variational multiscale method, enabling compari-

son with classical stabilized methods.

The chapter outline is as follows: first, details of the VMS are provided, along with some assumptions made to obtain practical stabilized methods. Next, the GFEM is reformulated for comparison to these methods, highlighting the potential of the enrichment selection process for stabilizing advection-dominated problems. Lastly, details for deriving analytical, exponential enrichments are shown using the VMS framework connected with GFEM. Chapters 5 and 6 present stable solutions using these exponential enrichments for the steady/unsteady one- and two-dimensional advection-diffusion problems and the nonlinear, one-dimensional Burgers' equation.

4.1 The GFEM as a Stabilized Method

4.1.1 Variational Multiscale Method

The VMS procedure begins with a sum decomposition of the solution (u) into coarse/resolved scales (\bar{u}) and fine/subgrid scales (u'), such that $u = \bar{u} + u'$. An *exact* equation for the coarse scales, and thus stable solutions, can be obtained when u' is derivable analytically [51]:

$$a(\bar{w}, \bar{u}) + (\mathcal{L}^* \bar{w}, u')_{\Omega} = (\bar{w}, f)_{\Omega} \quad \text{on } \Omega \quad (4.1)$$

where the fine scales depend on the coarse-scale residual error ($\mathcal{L}u - f$), and a

fine-scale Green's function (g'):

$$u'(\mathbf{x}) = - \int_{\Omega_s} g'(\mathbf{x}, \mathbf{s})(\mathcal{L}\bar{u} - f)(\mathbf{s})d\Omega_s \quad (4.2)$$

Note Eq. 4.1 is essentially a modification of the classical Galerkin method given in Eq. 2.5. Additionally, Eq. 4.2 assumes smoothness of \bar{u} . In the case of the FEM, in which the gradients of the basis have discontinuities across element boundaries, additional jump terms are necessary. For this rough case, fine scales are given by:

$$u'_h(\mathbf{x}) = - \sum_{e=1}^{n_{el}} \left(\int_{\Omega_s^e} g'(\mathbf{x}, \mathbf{s})(\mathcal{L}\bar{u}_h - f)(\mathbf{s})d\Omega_s^e + \int_{\Gamma_s^e} g'(\mathbf{x}, \mathbf{s})(b\bar{u}_h)(\mathbf{s})d\Gamma_s^e \right) \quad (4.3)$$

where b is a boundary operator and n_{el} are the total number of finite elements.

The challenge of this formulation is determining the analytical fine-scale Green's function g' . Typically, the exact analytical fine-scale Green's function is unknown; thus, additional assumptions are necessary in practice. That is, an approximation is made on the fine-scale Green's function such that $g' \approx \bar{g}'$. One such assumption, as is shown in the early VMS work by Hughes in [69], is to replace the global Green's function with elemental Green's functions, which are zero on element boundaries such that:

$$\begin{aligned}
\bar{g}'(\mathbf{x}, \mathbf{s}) &= g'_e(\mathbf{x}, \mathbf{s}) & \forall \mathbf{x}, \mathbf{s} \in \Omega^e, e = 1, 2, \dots, n_{el} \\
g'_e(\mathbf{x}, \mathbf{s}) &= 0 & \text{on } \Gamma^e, e = 1, 2, \dots, n_{el}
\end{aligned}
\tag{4.4}$$

Here, subgrid scales get confined within element interiors by vanishing on element boundaries. This process is known as *static condensation*, which results in the removal of the additional degrees of freedom the subgrid scales introduce. Note that the concept of element Green's functions has many similarities to that of residual-free bubbles. For information on this connection, see [51].

4.1.2 Stabilized Methods

Classical stabilized methods for the FEM make two additional assumptions beyond elemental Green's functions that lead to practical methods. First, the coarse-scale residual error ($\mathcal{L}\bar{u} - f$) is assumed constant over each element. Note this is only exactly true in the case of one-dimensional problems where volumetric forcing, f , is constant over each element and the linear operator, \mathcal{L} , contains only derivatives. Second, the elemental Green's function is assumed constant over each element, with the optimal value given by the mean. The result, as shown in [51], are stabilized methods of the following form:

$$a(\bar{w}_h, \bar{u}_h) + (\mathbf{L}\bar{w}_h, \tau(\mathcal{L}\bar{u}_h - f))_\Omega = (\bar{w}_h, f)_\Omega \quad \text{on } \Omega
\tag{4.5}$$

where τ is the mean value of the element Green's function given by:

$$\tau = \frac{1}{\text{meas}(\Omega^e)} \int_{\Omega_x^e} \int_{\Omega_s^e} g'_e(\mathbf{x}, \mathbf{s}) d\Omega_s^e d\Omega_x^e \quad (4.6)$$

and \mathbf{L} is a differential operator given by:

$$\begin{aligned} \mathbf{L} &= \mathcal{L}_{adv} \quad \text{SUPG} \\ \mathbf{L} &= \mathcal{L} \quad \text{GLS} \\ \mathbf{L} &= -\mathcal{L}^* \quad \text{Multiscale} \end{aligned} \quad (4.7)$$

This approximation is adequate for low-order, h -refinement methods. However, for high-order, p -refinement methods, the variation of τ over an element may be required [51]. The subsequent section outlines the GFEM and shows its relation to VMS/stabilized methods as a high-order, naturally stabilizing method.

4.1.3 Reformulation of the GFEM

Recall the GFEM approximation in Eq. 2.10. This approximation can similarly be expressed in terms of the FEM portion/"coarse scales" and enriched portion/"fine scales" such that:

$$u_h = \bar{u}_h + u'_h \quad (4.8)$$

where

$$\begin{aligned}
\bar{u}_h &= \sum_{\alpha=1}^{N(h)} \bar{c}_\alpha \varphi_\alpha = (\bar{\phi})^T \bar{\mathbf{c}} \\
u'_h &= \sum_{\alpha=1}^{N(h)} \varphi_\alpha \sum_{j=1}^M c'_{\alpha j} E_{\alpha j} = (\phi')^T \mathbf{c}'
\end{aligned} \tag{4.9}$$

Note that the coarse scales need not contain only FEM shape functions. For example, one could consider the coarse scales as all GFEM shape functions containing products of linear FEM shape functions with constant and linear enrichments (i.e., $p = 2$ GFEM solution).

Substitution of Eq. 4.8 into the Galerkin formulation (Eq. 2.5) results in two subproblems:

$$\begin{aligned}
a(\bar{w}_h, \bar{u}_h) + (\mathcal{L}^* \bar{w}_h, u'_h)_\Omega &= (\bar{w}_h, f)_\Omega \\
a(w'_h, \bar{u}_h) + (\mathcal{L}^* w'_h, u'_h)_\Omega &= (w'_h, f)_\Omega
\end{aligned} \tag{4.10}$$

The latter equation can be rearranged such that:

$$(\mathcal{L}^* w'_h, u'_h)_\Omega = -(w'_h, (\mathcal{L} \bar{u}_h - f))_\Omega \tag{4.11}$$

Substitution of Eq. 4.9 into Eq. 4.11 and solving for u'_h :

$$u'_h = -(\phi')^T (\mathbf{K}')^{-1} (\phi', (\mathcal{L} \bar{u}_h - f))_\Omega \tag{4.12}$$

where

$$\mathbf{K}' = (\mathcal{L}^*(\phi'), (\phi')^T)_\Omega \quad (4.13)$$

Note to solve for the fine scales as done in Eq. 4.12, knowledge of the residual error of the coarse scales is necessary. For the purpose of comparing the GFEM to stabilized methods, assuming the residual error of the coarse scales is known is valid, as both coarse and fine scales are solved for simultaneously in the GFEM in Eq. 2.11. Finally, substitution of Eq. 4.12 into the first equation of Eq. 4.10 results in the following solution for the coarse scales:

$$a(\bar{w}_h, \bar{u}_h) - (\mathcal{L}^* \bar{w}_h, (\phi')^T (\mathbf{K}')^{-1} (\phi', (\mathcal{L} \bar{u}_h - f)))_\Omega = (\bar{w}_h, f)_\Omega \quad (4.14)$$

Comparison of the GFEM formulation (Eq. 4.14) to the VMS formulation (Eq. 4.1) and classical stabilized methods (Eq. 4.5), yields the following insights:

1. Similar to the VMS and stabilized methods, the "fine scales" of the GFEM solution are driven by the residual error of the "coarse scales." This is observed in Eq. 4.12, where the fine scales of the GFEM solution (u'_h) depend directly on the residual error of the coarse scales ($\mathcal{L} \bar{u}_h - f$).
2. Unlike the VMS, the GFEM solution does *not* require the fine scales be zero on element boundaries. Specifically, no assumptions are made on the GFEM enrichments chosen to construct the local approximation space in Eq. 2.8.
3. Unlike classical stabilized methods, the GFEM solution accounts for spatial

variance over each element, thus making it better suited for p -refinement. Specifically, the GFEM shape functions (ϕ) are spatially variant, unlike the stabilization parameter (τ) in the stabilized methods.

4. The coarse-scale residual error need not be assumed constant over each element to lead to a practical method.
5. Using static condensation in GFEM is helpful for theoretical comparison with alternative multiscale/stabilization techniques but not required in practice. In the GFEM approach, the fine scales stabilize the coarse scales and contribute to the convergence rate.
6. In the GFEM, only the basis of the fine scales is chosen *a priori*, with the corresponding weights determined simultaneously with the coarse scales through Galerkin's method. The benefit of simultaneously solving the weights of both the coarse and fine scales is that the fine-scale basis is better applied over general meshes, as the corresponding fine-scale weights adjust accordingly to grid refinement. Selection of only the fine-scale basis in GFEM offers an improvement over stabilized methods, where the stabilization parameter is chosen *a priori* and depends more strictly on specific grid discretization.

Regarding the last two points above, some nuances warrant an expanded discussion. The implementation of GFEM in this work does not make use of static condensation. Thus, calculation of the additional degrees of freedom introduced

by the fine scales in GFEM requires the inversion of a larger matrix than those obtained by using static condensation. As a result, the computational costs of the GFEM are greater than standard FEM over equivalent grid sizes. However, as demonstrated for a given mesh size, GFEM with solution-tailored enrichments has substantially reduced errors compared to standard FEM. Alternatively, GFEM achieves the same error levels of standard FEM with far fewer degrees of freedom, which has yielded a computational speed-up when applied on other multiscale problems [70]. A detailed investigation of the computational cost-benefit comparison against standard FEM approaches is not the focus of the current work but is likely in future studies, particularly those involving three-dimensional advection-dominated physics. For problems where static condensation is desired or deemed advantageous, an algorithm suitable for the solution of hierarchically-enriched finite element methods, such as the GFEM proposed in this work, is provided in [71] and used in application to 3D linear elastic fracture mechanics [70] and transient heat conduction [72] in the open literature. Note that the algorithm is algebraically equivalent to the direct solution of the enriched systems of equations, and merely alters the efficiency with which the equations can be solved, and exploits an ability to re-use large portions of the factorized system matrices if using a time-evolving enrichment strategy. The algorithm does not restrict enrichment selection and applies to polynomial, non-polynomial, numerical, and time-dependent enrichment bases. The algorithm is readily available to address the advection-diffusion equation should a detailed comparison of computational efficiency against alternative

approaches be of primary interest.

In the current work, the *a priori* chosen enrichment bases are derived from fundamental solutions to the governing equations. For more general applicability, there is a growing body of literature for GFEM with global-local enrichments [71] where the enrichment basis is computed on the fly, using two-way communication between a coarse, global discretization and a potentially highly-adapted local boundary value problem defined in regions of localized interest. The local boundary value problems obtain boundary conditions from the coarse global solutions, and the solution of the local BVP made an enrichment for the coarse global model. The two-way information transfer dramatically improves the accuracy of the method [73] as compared to more standard global-local FEM approaches [74]. Regardless of the computational size of the local BVP, the use of the local solution as enrichment adds a minimal number of degrees of freedom to each enriched node in the global model, equal to the dimensionality of the solution to the field problem under consideration - one DOF is added per node in a scalar field problem such as heat conduction [75], and three DOFs are added per node for a vector field problem, such as three-dimensional elasticity [71]. Additional computational efficiency is achievable through the parallel solution of local BVPs in scenarios where the local BVP(s) become large as compared to the size of the global problem [76]. It is important to note there is no requirement involving conformity between the coarse and fine scales as this property is retained through the solution of the resulting problem inclusive of all relevant scales of interest, as is the case with any

conforming finite element approach. Alternative approaches require assumptions of strict locality (use of elemental Green's functions/bubble functions) over subgrid scales to avoid the need for iterations between resolved and subgrid scales, as well as between adjacent subgrid-scale problems to maintain C^0 continuity across the solution domain [69, 77, 78].

4.2 Example: Stabilization of a Steady, 1D Advection-Diffusion Equation

To demonstrate the stabilizing property of GFEM enrichments, consider the following simple 1D steady advection-diffusion equation with constant volumetric forcing:

$$\begin{aligned} \mathcal{L}u &= \left(a_x \frac{du}{dx} \right) + \left(-k \frac{d^2u}{dx^2} \right) = 100 \quad \text{on } \Omega = [0, 1] \\ u &= 0 \quad \text{on } \Gamma_D = \{0, 1\} \end{aligned} \tag{4.15}$$

and a_x and k are the rate of advection and rate of diffusion, respectively. This problem has an analytical solution given by:

$$u = \frac{100k(1 - x - e^{\frac{a_x}{k}x} + xe^{\frac{a_x}{k}})}{a_x(e^{\frac{a_x}{k}} - 1)} \tag{4.16}$$

Hughes shows in [51] the exact elemental Green's function is given by:

$$g'_e(x, s) = \begin{cases} C_1(s)(1 - e^{-2Pe\frac{x}{h}}) & x \leq s \\ C_2(s)(e^{-2Pe\frac{x}{h}} - e^{-2Pe}) & x > s \end{cases} \quad (4.17)$$

where

$$\begin{aligned} C_1(s) &= \frac{1 - e^{-2Pe(1-\frac{s}{h})}}{a_x(1 - e^{-2Pe})} \\ C_2(s) &= \frac{e^{-2Pe(1-\frac{s}{h})}}{a_x(1 - e^{-2Pe})} \end{aligned} \quad (4.18)$$

and $Pe = \frac{a_x h}{2k}$ is the elemental Péclet number. Without stabilization, $p = 1$ FEM will exhibit spurious oscillations when $Pe > 1$. From Eqs. 4.6 and 4.17, the optimal value for τ in the stabilized methods applied to 4.15 is given by:

$$\tau_{optimal} = \frac{h}{2a_x} \left(\coth Pe - \frac{1}{Pe} \right) \quad (4.19)$$

For direct comparison of GFEM to stabilized methods, consider Eq. 4.14. For the simple problem 4.15, volumetric forcing is constant and the Galerkin formulation is concerned only with gradients. Thus the residual error of the $p = 1$ FEM solution $(\mathcal{L}\bar{u}_h - f)$ may be extracted from the integrand such that:

$$a(\bar{w}_h, \bar{u}_h) - (\mathcal{L}^* \bar{w}_h, \tau_{GFEM}(x)(\mathcal{L}\bar{u}_h - f))_{\Omega} = (\bar{w}_h, f)_{\Omega} \quad (4.20)$$

where

$$\tau_{GFEM}(x) = (\boldsymbol{\phi}')^T (\mathbf{K}')^{-1} (\boldsymbol{\phi}', 1)_{\Omega} \quad (4.21)$$

Here, Eq. 4.20 is form identical to the multiscale method Eq. 4.5, except τ_{GFEM} is spatially variant.

This example was solved over uniform grids sizes of $h = \{\frac{1}{5}, \frac{1}{10}, \frac{1}{15}, \frac{1}{20}, \frac{1}{30}, \frac{1}{40}, \frac{1}{50}, \frac{1}{60}, \frac{1}{80}, \frac{1}{100}\}$ over a range of Péclet numbers. To vary the Péclet number, the rate of diffusion was fixed at $k = 1$, and the rate of advection was varied with $a_x = \{10, 20, 40, 100, 200, 400\}$. Eq. 4.15 was solved using linear ($p = 1$) FEM, and quadratic ($p = 2$) thru ($p = 6$) polynomial GFEM. The GFEM local approximation space (Eq. 2.8) is given by:

$$\chi_{\alpha} = \text{span} \left\{ 1, \frac{x - x_{\alpha}}{h}, \frac{(x - x_{\alpha})^2}{h^2}, \dots, \frac{(x - x_{\alpha})^5}{h^5} \right\} \quad (4.22)$$

Note $p = 2$ GFEM uses only the first two elements of Eq. 4.22 as enrichments, $p = 3$ GFEM uses only the first three elements, and this trend continues up to $p = 6$ GFEM, where the entire set is used. A plot of the normalized optimal stabilization parameter in Eq. 4.19 is shown in Fig. 4.1. For Péclet numbers slightly above 1, the instabilities in the $p = 1$ FEM solution are small, thus a small value of τ is necessary to stabilize. However, as the Péclet number increases, the advection term becomes more dominant and requires a larger τ to stabilize. The mean value of $\tau_{GFEM}(x)$ from Eq. 4.21 is also shown in Fig. 4.1. Here, for increasing enrichment order, the GFEM solution follows the optimal τ over increasing ranges of Pe. Relative H_1

norms versus total degrees of freedom are shown in Fig. 4.2 for various Pe . The finest grids studied are used for each of the cases for computing true convergence rates. As Pe increases, error levels increase, and convergence rates decrease over coarse grids. Note when Pe is "small" (i.e. Fig. 4.2a, b, and c), the higher-order polynomial solutions converge to the reference solution over fine grids, returning errors on the order of $\mathcal{O}(10^{-7})$. In these cases, the errors returned for the finest two grids studied begin to oscillate with increasing resolution, so the convergence rate before asymptotic behavior is shown instead. When $Pe = 200h$, none of the polynomial solutions return near-optimal convergence, even for the finest grid sizes studied. Solutions for a fixed grid of 10 elements is shown in Fig. 4.3. For $Pe = 0.5$ and $Pe = 1$, no oscillations are observed in any polynomial solutions as expected. When $Pe = 2$ and $Pe = 5$ instabilities in the $p = 1$ FEM and $p = 2$ GFEM solution are observed, with oscillations in the $p = 2$ GFEM solution being less severe. When $Pe = 10$, the $p = 4$ GFEM solution begins to exhibit oscillations. Lastly, at $Pe = 20$ all solutions exhibit spurious oscillations.

This simple example demonstrates the natural stabilizing property of enrichments in the GFEM without the additional assumptions made in traditional stabilized methods. However, enrichment quality remains essential for solution convergence. The standard polynomial set often used in GFEM does not efficiently capture the upwind behavior of an advection-dominated problem, therefore motivating the use of solution-tailored enrichments for more effective stabilization, which is the focus of the following section.

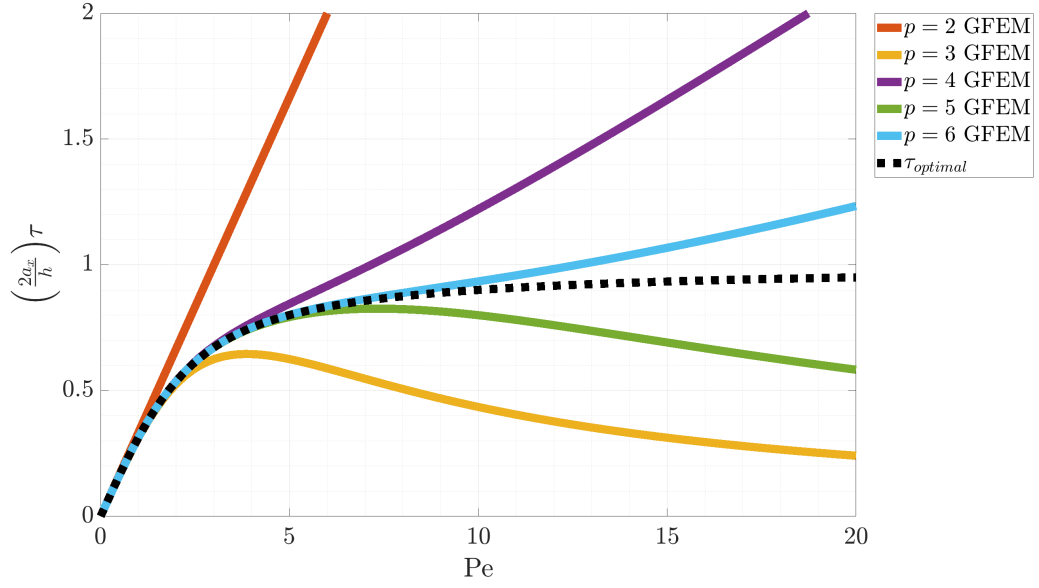


Figure 4.1: Optimal stabilization parameter ($\tau_{optimal}$) and the GFEM stabilization parameter (τ_{GFEM}) as the local Péclet number (Pe) increases.

4.3 Obtaining Stabilizing Enrichments in GFEM

This section makes use of fine-scale Green's functions in the VMS to provide insight into enrichments for GFEM. Consider Eq. 2.1. Substitution of $u = \bar{u} + u'$ and solving for the fine scales results in the following equation:

$$\begin{aligned}
 \mathcal{L}u'(\mathbf{x}) &= -(\mathcal{L}\bar{u} - f)(\mathbf{x}) \quad \text{on } \Omega \\
 u'(\mathbf{x}) &= -(\bar{u} - g_{\Gamma_D})(\mathbf{x}) \quad \text{on } \Gamma_D \\
 \frac{\partial u'(\mathbf{x})}{\partial n} &= -\left(\frac{\partial \bar{u}}{\partial n} - g_{\Gamma_N}\right)(\mathbf{x}) \quad \text{on } \Gamma_N
 \end{aligned} \tag{4.23}$$

Consider a Green's function of the fine scales problem Eq. 4.23, g' , such that:

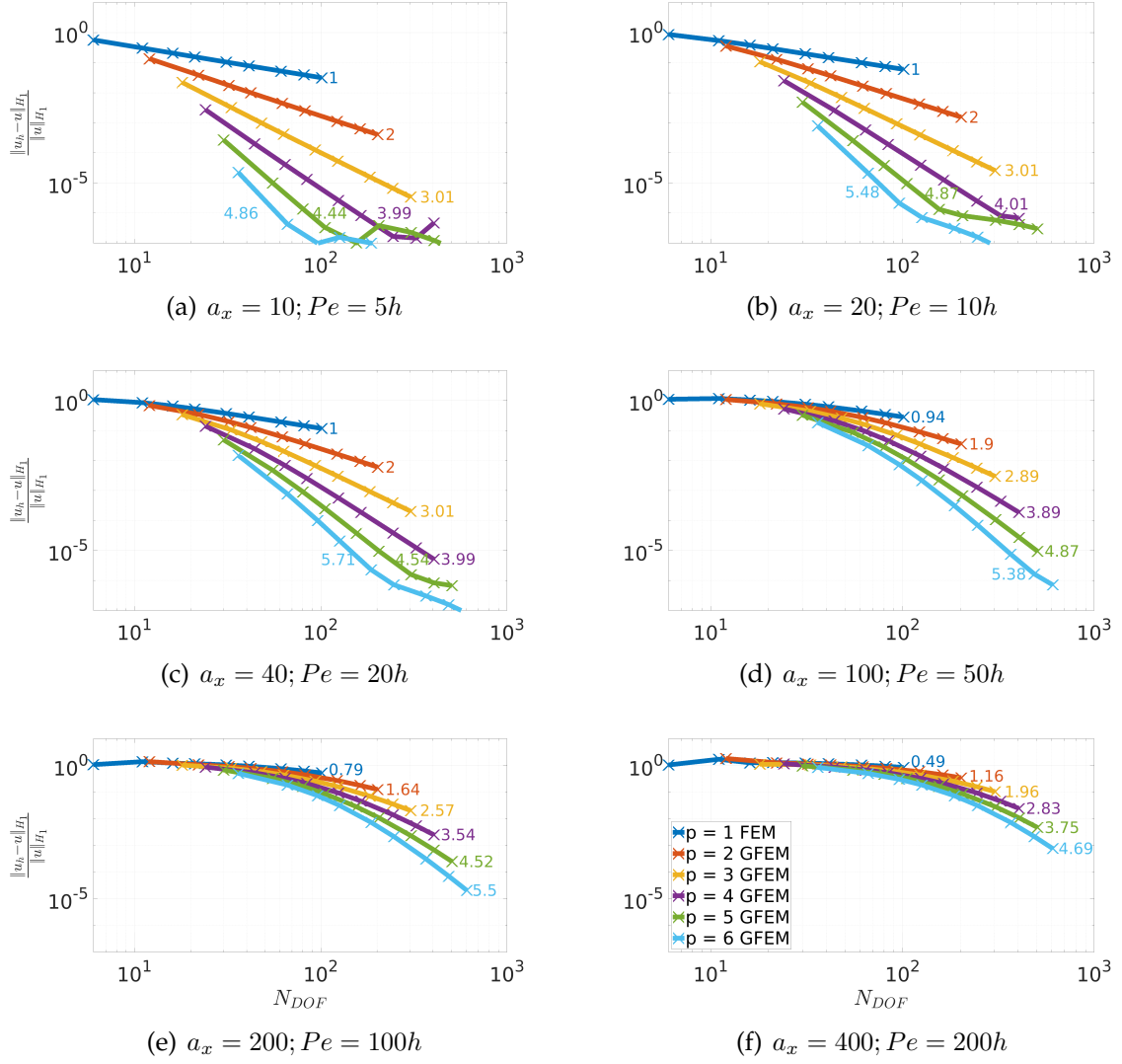


Figure 4.2: Relative H_1 norm $\left(\frac{\|u_h - u\|_{H_1}}{\|u\|_{H_1}}\right)$ versus total degrees of freedom (N_{DOF}) for a simple advection-diffusion problem.

$$\mathcal{L}g'(\mathbf{x}, \mathbf{s}) = \delta(\mathbf{s} - \mathbf{x}) \quad \text{on } \Omega \quad (4.24)$$

where δ is the Dirac delta function. Multiply Eq. 4.24 by $-(\mathcal{L}\bar{u} - f)(\mathbf{s})$ and integrate with respect to \mathbf{s} :

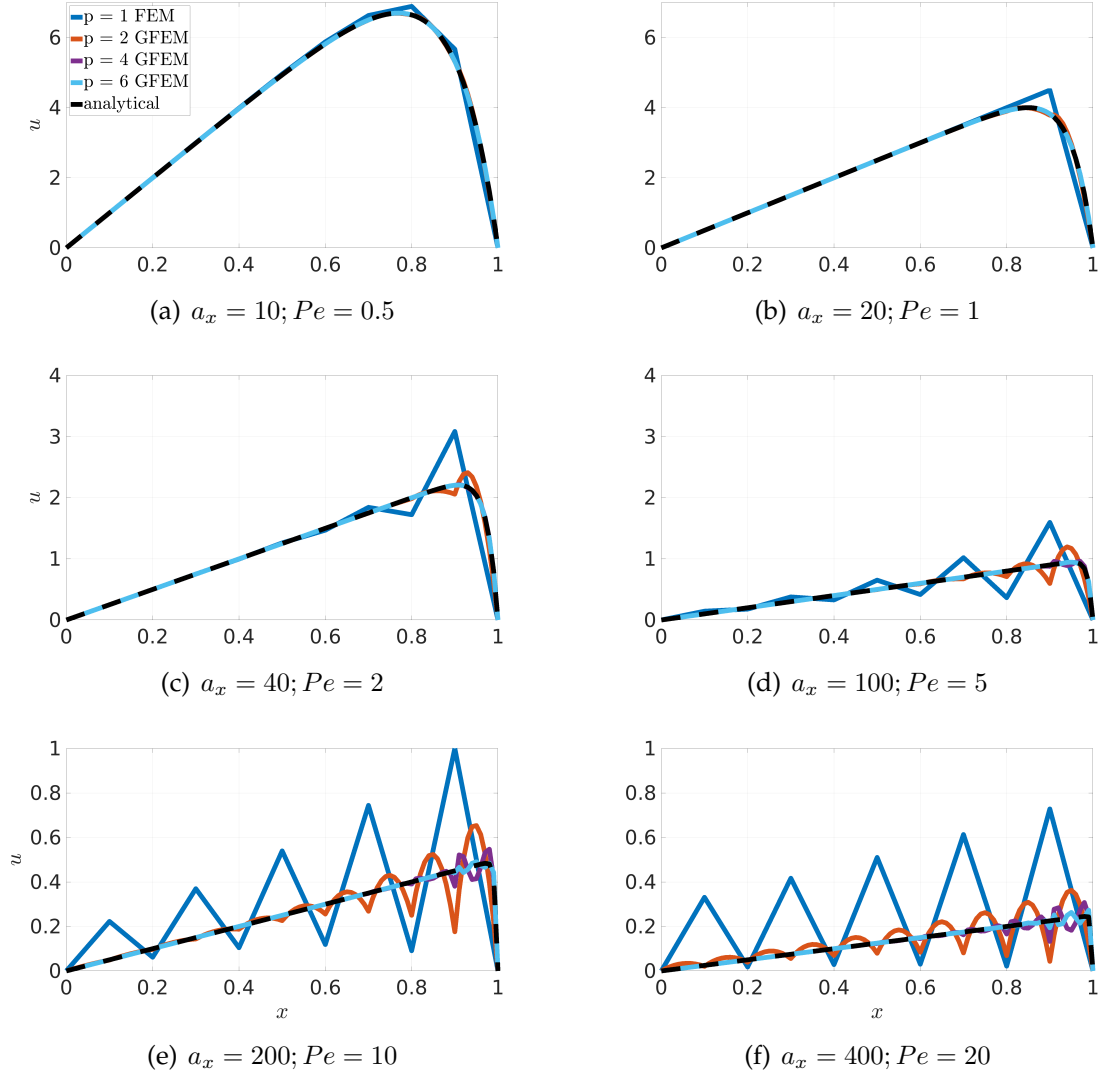


Figure 4.3: 10-element solutions (u) for a simple advection-diffusion problem.

$$-\int_{\Omega_s} \mathcal{L}g'(\mathbf{x}, \mathbf{s})(\mathcal{L}\bar{u} - f)(\mathbf{s}) = -\int_{\Omega_s} \delta(\mathbf{s} - \mathbf{x})(\mathcal{L}\bar{u} - f)(\mathbf{s}) = -(\mathcal{L}\bar{u} - f)(\mathbf{x}) \quad (4.25)$$

Since \mathcal{L} operates only on \mathbf{x} , it can be extracted from the integrand. Comparing to Eq. 4.23, reveals:

$$u'(\mathbf{x}) = - \int_{\Omega_s} g'(\mathbf{x}, \mathbf{s})(\mathcal{L}\bar{u} - f)(\mathbf{s}) \quad (4.26)$$

This is the smooth VMS solution shown in Eq. 4.2. In the case of the FEM, the additional jump error terms in Eq. 4.3 must be included. Consider Eq. 4.24. If $\mathbf{x} \neq \mathbf{s}$, then the problem becomes one of finding the homogeneous solution of g' . Since \mathcal{L} is a linear operator, g' is separable such that $g'(\mathbf{x}, \mathbf{s}) = g'_1(\mathbf{x})g'_2(\mathbf{s})$, and Eq. 4.24 can be used to solve for $g'_1(\mathbf{x})$ such that:

$$\mathcal{L}g'_1(\mathbf{x}) = 0 \quad \text{on } \Omega \quad (4.27)$$

Additionally, Eq. 4.3 simplifies to:

$$u'_h(\mathbf{x}) = -g'_1(\mathbf{x}) \sum_{e=1}^{n_{el}} \left(\int_{\Omega_s} g'_2(\mathbf{s})(\mathcal{L}\bar{u}_h - f)(\mathbf{s}) + \int_{\Gamma_s^e} g'_2(\mathbf{s})(b\bar{u}_h)(\mathbf{s})d\Gamma_s^e \right) \quad (4.28)$$

In the GFEM, the fine scales are given by Eq. 4.9. Substitution into Eq. 4.28:

$$\phi'(\mathbf{x})^T \mathbf{c}' = g'_1(\mathbf{x}) \sum_{e=1}^{n_{el}} \left(- \int_{\Omega_s} g'_2(\mathbf{s})(\mathcal{L}\bar{u} - f)(\mathbf{s}) - \int_{\Gamma_s^e} g'_2(\mathbf{s})(b\bar{u}_h)(\mathbf{s})d\Gamma_s^e \right) \quad (4.29)$$

By direct comparison of the left- and right-hand side of Eq. 4.29, solution tailored enrichments are obtainable if one knows the solution to $g'_1(\mathbf{x})$. The solution

of $g'_1(\mathbf{x})$ can be obtained from Eq. 4.27 as a summation of the fundamental solutions y_i product with corresponding coefficients c_i . For example, if $g_1(\mathbf{x})$ has two fundamental solutions, then $g_1(\mathbf{x}) = c_1 y_1(\mathbf{x}) + c_2 y_2(\mathbf{x})$. Since the coefficients c_i are only used to enforced boundary conditions, they are not necessary for deriving enrichments for the GFEM. That is, useful enrichments for any linear problem $\mathcal{L}u = f$ are observed if one knows one or more of the fundamental solutions to the homogeneous problem $\mathcal{L}u = 0$. (i.e. $E_{\alpha_j}(\mathbf{x}) = y_j(\mathbf{x})$). Due to the superposition principle of linear systems, these enrichments are applicable to any problems of the form $\mathcal{L}u = f$, regardless of boundary conditions or forcing f . The following section shows fundamental solutions for the one- and two-dimensional advection-diffusion equation.

4.3.1 Fundamental Solutions to the 1D and 2D Advection-Diffusion Equation

For the one- and two-dimensional advection-diffusion equation, the fundamental solutions are:

- 1D ($\mathcal{L} = -k \frac{d^2(\cdot)}{dx^2} + a_x \frac{d(\cdot)}{dx}$):

$$y_1 = 1 \text{ and } y_2 = \exp\left(\frac{a_x}{k} x\right)$$

- 2D ($\mathcal{L} = -k\Delta(\cdot) + \mathbf{a} \cdot \nabla(\cdot)$):

$$y_1 = 1, y_2 = \exp\left(\frac{a_x}{k} x\right), y_3 = \exp\left(\frac{a_y}{k} y\right), \text{ and } y_4 = \exp\left(\frac{a_x + a_y}{2k} (x + y)\right)$$

Chapter 5 provides solutions to the one- and two-dimensional steady/unsteady advection-diffusion equation. All GFEM solutions displaying “+ exp.” at the end of the polynomial order indicate using the exponential enrichments from this section. For example, a 1D, $p = 2 + \text{exp.}$ GFEM solution to the steady advection-diffusion equation will include constant and linear polynomial enrichments as well as the exponential enrichment $\exp\left(\frac{ax}{k}\right)$. Although the exponential functions presented here are analytical solutions to the homogeneous problem, they are numerically ill-suited for huge exponents due to machine precision. Specifically, for exponents of around 700 or larger, the value is no longer storable using double-precision. A simple solution to alleviate this is to shift the exponential enrichments by the node they are defined over. For example, if node x_α is enriched by $\exp\left(\frac{ax}{k}\right)$, an equivalent enrichment which is better suited for large exponents is given by $\exp\left(\frac{ax}{k}(x - x_\alpha)\right)$. These enrichments represent equivalent approximation spaces because the shift in constant is recoverable in the corresponding weights.

4.3.2 *A Priori* Error Estimations

A priori error estimates are well-known for polynomial approximation spaces: for $\Omega \subset \mathbb{R}^n$ with Lipschitz boundary, a p -degree polynomial solution converges in the L_2 and H_1 norm versus total degrees of freedom at a theoretical convergence rate of $\frac{p+1}{n}$ and $\frac{p}{n}$, respectively. Theoretical convergence rates are not developed formally for approximation spaces containing the exponential enrichments in the

previous section. However, insights on expected convergence behavior are provided by considering the relevance of the exponential enrichment. Specifically, for linear BVPs ($\mathcal{L}u = f$), u may be split in terms of the complementary and particular solutions, such that $u = u_c + u_p$. Furthermore, the complementary solution u_c may be described through superposition as $u_c = c_1y_1 + c_2y_2 + \dots + c_iy_i$, where y_i are the fundamental solutions of the homogeneous problem, and c_i are corresponding coefficients used to enforce boundary conditions. Since the exponential enrichments in the previous section represent y_i *exactly* (for $\mathcal{L} \equiv$ advection-diffusion equation), it is reasonable to assume removal from the problem for the remaining polynomial approximation space. Thus, for sufficiently smooth boundary conditions and particular solutions, one should expect similar convergence rates to the theoretical rates provided above, of at least $\frac{p}{n}$. If the particular solution plus boundary conditions do not include gradients of the approximation, then convergence rates of $\frac{p+1}{n}$ may be achieved. For problems where polynomials exactly represent the particular solution plus boundary conditions, one should expect the numerical solution to be the same order as the reference solution.

Chapter 5

GFEM Solution to the Advection-Diffusion Equation

The focus of the next two chapters is to explore solution-tailored enrichments for the stabilization of advection-dominated problems. In this chapter the exponential enrichments obtained in chapter 4 are applied for solutions to the advection-diffusion equation. Advection-diffusion equations exhibit similar instabilities in the advection term as the Navier-Stokes equations. However, it avoids additional complexity introduced by the nonlinear term and additional variables of interest: density, pressure, and temperature. The focus of chapter 6 is to reintroduce the nonlinearity of the Navier-Stokes equations by solving the Burgers' equation. The Burgers' equation is equivalent to the advection-diffusion equation, except the rate of advection is replaced with the solution variable itself. The result is a nonlinear advection term with many similarities to the Navier-Stokes equations. The Burgers' equation is useful to study the interaction between transient, dissipative, and

nonlinear terms.

The outline of this chapter is as follows: first, the governing equations for the advection-diffusion equation are presented, followed by the corresponding GFEM matrix formulation. Then, GFEM solutions to the steady/unsteady one- and two-dimensional advection-diffusion equations are presented, followed by a general discussion of the results.

5.1 Governing Equation and GFEM Linear System of Equations

For the advection-diffusion equation with constant rates of advection and diffusion, the linear differential operator is given by $\mathcal{L}(\cdot) = \frac{\partial(\cdot)}{\partial t} + \mathbf{a} \cdot \nabla(\cdot) - k\Delta(\cdot)$. The resulting differential equation becomes:

$$\begin{aligned} \frac{\partial u}{\partial t} + \mathbf{a} \cdot \nabla u - k\Delta u &= f \quad \text{on } \Omega \\ u &= g_{\Gamma_D} \quad \text{on } \Gamma_D \\ \nabla u \cdot \mathbf{n} &= g_{\Gamma_N} \quad \text{on } \Gamma_N \\ u(\mathbf{x}, 0) &= u_0 \quad \text{on } \Omega \end{aligned} \tag{5.1}$$

Substitution of the GFEM approximation Eq. 2.10 into Eq. 5.1 and following the Galerkin method procedure outlined in Chapter 2 results in the following:

$$\mathbf{M}\dot{\mathbf{c}} + (\mathbf{A} + \mathbf{K})\mathbf{c} = \mathbf{f} \quad (5.2)$$

where

$$\mathbf{M} = (\boldsymbol{\phi}, \boldsymbol{\phi}^T)_{\Omega} \quad (5.3)$$

$$\mathbf{A} = \mathbf{a} \cdot (\boldsymbol{\phi}, \nabla \boldsymbol{\phi})_{\Omega} \quad (5.4)$$

$$\mathbf{K} = k(\nabla \boldsymbol{\phi} \cdot (\nabla \boldsymbol{\phi})^T)_{\Omega} \quad (5.5)$$

$$\mathbf{f} = (\boldsymbol{\phi}, f)_{\Omega} + (\boldsymbol{\phi}, \nabla u \cdot \mathbf{n})_{\Gamma_N} \quad (5.6)$$

After applying the Crank-Nicolson method (Eq. 2.13) and enforcing Dirichlet boundary conditions (Eq. 2.15) to Eq. 5.2, the final system of equations is:

$$[\tilde{\mathbf{M}} + \mathbf{M}_{\Gamma_D}]\mathbf{c}^{n+1} = \tilde{\mathbf{b}} + \mathbf{b}_{\Gamma_D} \quad (5.7)$$

where $\tilde{\mathbf{M}} = \frac{1}{\Delta t}\mathbf{M} + \frac{1}{2}(\mathbf{A} + \mathbf{K})$, $\tilde{\mathbf{b}} = \frac{1}{\Delta t}\mathbf{M}\mathbf{c}^n + \frac{1}{2}[\mathbf{f}^{n+1} + \mathbf{f}^n - (\mathbf{A} + \mathbf{K})\mathbf{c}^n]$, and \mathbf{M}_{Γ_D} and \mathbf{b}_{Γ_D} are defined in Eqs. 2.16 and 2.17, respectively.

5.2 Numerical Results

This chapter presents solutions to several advection-diffusion problems up to two dimensions. For the following examples, please note:

1. All enrichments are shift by their nodal values to retain the physical meaning of the standard FEM DOFs at each node.
2. Special consideration is necessary to integrate the exponential enrichment functions accurately. The computational cost of integrating the enrichments is trivial in the following examples since the elemental matrices are not time-dependent. As such, the following work uses a conservative number of Gaussian quadrature points for each grid refinement. For example, we use ten-point Gaussian quadrature on the most refined meshes considered (approx. $\frac{1}{80}$ element size); while we use sixty-point Gaussian quadrature for the coarsest meshes considered (approx. $\frac{1}{10}$ element size). For problems where the elemental matrices are time-dependent, evaluation of the elemental matrices at each time step using Gaussian quadrature may increase costs considerably. More efficient integration strategies may be beneficial for these problems, such as the Gauss-Laguerre quadrature, an extension of Gaussian quadrature for integrating exponential functions.

5.2.1 Example: 1D Steady Advection-Diffusion Equation with Complex Volumetric Forcing

First consider the following 1D steady advection-diffusion equation:

$$\begin{aligned}
-k \frac{d^2 u(x)}{dx^2} + a_x \frac{du(x)}{dx} &= f(x) \quad \text{on } \Omega = [0, 1] \\
u &= \{0, 1\} \quad \text{on } \Gamma = \{0, 1\}
\end{aligned} \tag{5.8}$$

where a_x is the rate of advection in the x-direction, k is the rate of diffusion, and f is the volumetric forcing. For this example, $a_x = 200$, $k = 1$, and $f(x) = 100x + 2000 \sin^2 4\pi x$. A reference solution for this problem was generated using a 2000 element cubic GFEM solution, and is shown in Fig. 5.1. The highly advective nature of the problem is observed with a steep boundary layer forming around $x = 1$. Stability of the $p = 1$ FEM solution occurs at a grid size greater than or equal to 100 elements/101 DOFs. Eq. 5.8 is solved over uniform grids using $p = 1$ FEM, $p = 2$, $p = 3$, $p = 1 + \text{exp.}$, $p = 2 + \text{exp.}$, and $p = 3 + \text{exp.}$ GFEM. The local approximation space for GFEM is defined as:

$$\chi_\alpha = \text{span} \left\{ 1, \frac{x - x_\alpha}{h}, \frac{(x - x_\alpha)^2}{h^2}, e^{\frac{a_x}{k} x} - e^{\frac{a_x}{k} x_\alpha} \right\} \tag{5.9}$$

Relative H_1 norm versus total number of degrees of freedom is shown in Fig. 5.2. The vertical dashed line represents 101 DOFs at which the $p = 1$ FEM solution becomes stable. Here, the addition of linear and quadratic enrichments in GFEM only slightly improves the solution's convergence, whereas the addition of the exponential enrichments yields significant improvement. 48 DOFs solution plots are shown in Fig. 5.3. Linear, quadratic, and cubic solutions *without* use of the exponential enrichment are shown in Fig. 5.3a. Although quadratic and cubic GFEM

solutions exhibit less severe oscillations than the linear FEM, they are still present around the steep boundary layer at $x = 1$. Linear, quadratic, and cubic solutions *with* use of the exponential enrichment are shown in Fig. 5.3b. Here no instabilities are observed, and all the solutions compare favorably with the reference. Note these solutions are well below the stable limit of 101 DOFs.

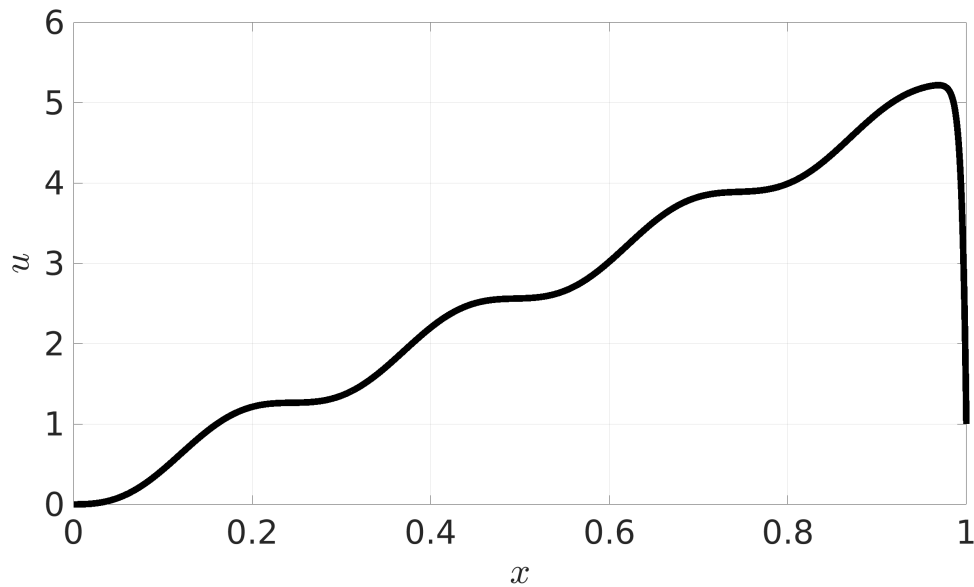


Figure 5.1: 2000 element cubic GFEM reference solution (u) for the 1D steady advection-diffusion problem with complex volumetric forcing ($f(x)$)

5.2.2 Example: 1D Unsteady Advection-Diffusion Equation with Complex Initial Condition

This extension is made to the unsteady case as well. Consider the following unsteady problem:

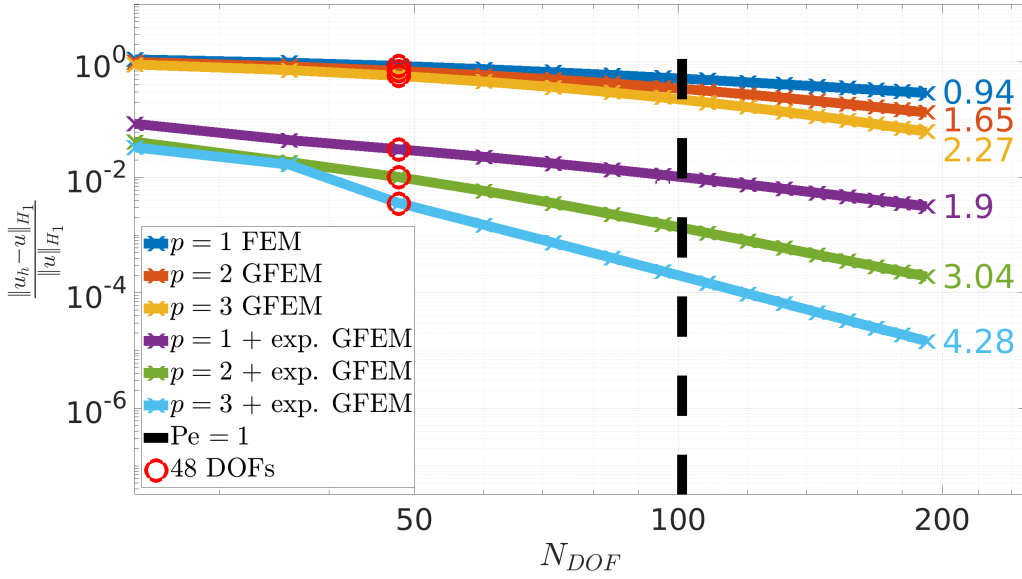


Figure 5.2: Relative H_1 norm $\left(\frac{\|u_h - u\|_{H_1}}{\|u\|_{H_1}}\right)$ versus degrees of freedom (N_{DOF}) for the 1D steady advection-diffusion problem with complex volumetric forcing ($f(x)$).

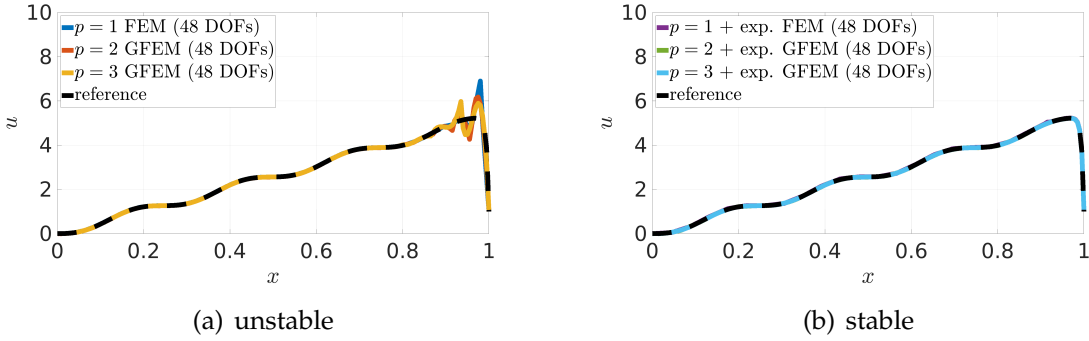


Figure 5.3: 48 DOF linear, quadratic, and cubic solutions (a) with and (b) without exponential enrichments.

$$\begin{aligned}
 \frac{\partial u(x, t)}{\partial t} &= k \frac{\partial^2 u(x, t)}{\partial x^2} - a_x \frac{\partial u(x, t)}{\partial x} & \text{on } \Omega &= [0, 1] \\
 u &= \{1, 0\} & \text{on } \Gamma &= \{0, 1\} \\
 u(x, 0) &= 0.5(1 + \tanh(5 - 50x)) & \text{on } \Omega &= [0, 1]
 \end{aligned} \tag{5.10}$$

For this example, $a_x = 100$, $k = 1$, and $t = [0, 0.02]$. For all figures in this section, time t is normalized to be $\bar{t} = [0, 1]$. A reference solution for this problem was generated using a 1000 element cubic GFEM solution, and is shown in Fig. 5.4 for various normalized times, \bar{t} . The Crank-Nicolson method was used for temporal discretization with 1000 time steps. Initially there is no presence of upwind behavior, but as $\bar{t} \rightarrow 1.0$, a steep boundary layer forms around $x = 1$. Stability of the linear FEM solution occurs at a grid size greater than or equal to 50 elements / 51 DOFs. Similar to the steady case, this problem was solved over uniform grids using linear $p = 1$ FEM, $p = 2$, $p = 3$, $p = 1 + \text{exp.}$, $p = 2 + \text{exp.}$, and $p = 3 + \text{exp.}$ GFEM. The local GFEM approximation space is defined in 5.9. Relative H_1 norms of the 24 DOFs solutions versus normalized time are shown in 5.5. Initially no presence of upwind behavior is observed, thus the polynomial solutions with and without exponential enrichments solutions return similar error. The initially larger errors in the exponential solutions is explained by considering the complexity of the initial condition. The shape of the initial condition $u(x, 0) = 0.5(1 + \tanh(5 - 50x))$ behaves similarly to a discontinuity in the domain, and requires h -refinement to resolve unless proper enrichment is used to capture it. Since equal DOFs are considered, the addition of the exponential enrichments coarsens the grid, resulting in increased error as both the polynomial enrichments and exponential enrichments are inefficient at capturing the shape of the initial condition. However, around $\bar{t} = 0.4$, upwind behavior is observed. The result is spurious oscillations in the solutions without exponential enrichments, and improved convergence of those

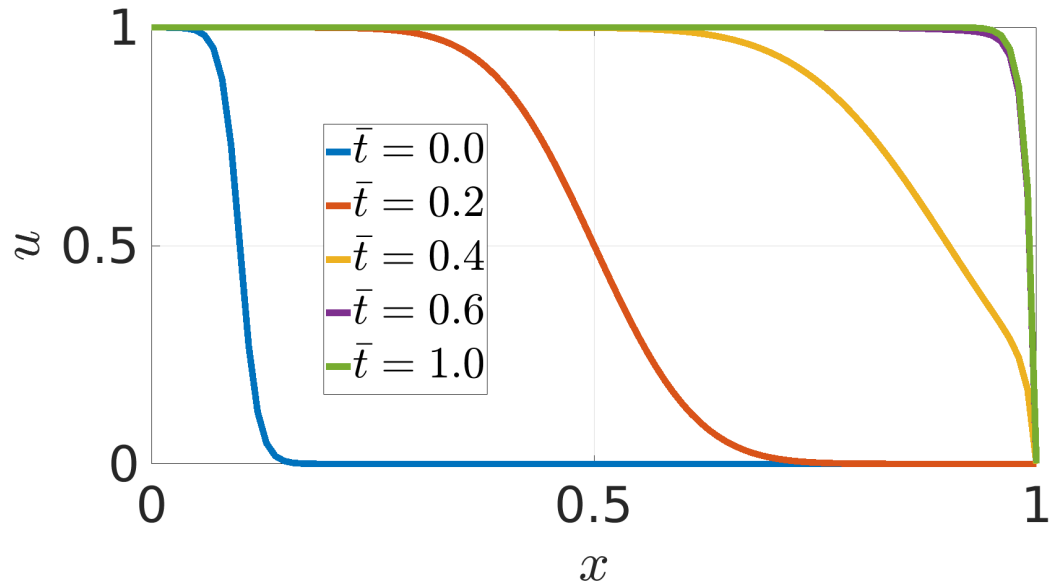
with them. This is observed in Fig. 5.6, which displays 24 DOF solutions versus normalized time. Lastly, Fig. 5.7 shows the relative H_1 norm versus total degrees of freedom at various time instances. The errors returned by the polynomial solutions with and without the exponential enrichment prior to the formation of the boundary layer are similar, as shown by Figs. 5.7 (a) and 5.7 (b). However, once the boundary layer begins to form, the oscillations affect convergence of the polynomial solutions without exponential enrichments as seen in Fig. 5.7 (c) and Fig. 5.7 (d). Note that error from the GFEM solutions using exponential enrichments approaches a constant value later due to convergence to the numerical reference. At $\bar{t} = 1$ relative errors in the H_1 norm are around 0.01% or less. In the steady-state, the problem simplifies down to a homogeneous problem, which the exponential enrichments capture exactly since the boundary conditions are not complex.

5.2.3 Example: 2D Steady Advection-Diffusion Equation with Complex Volumetric Forcing

Consider the following 2D steady advection-diffusion equation:

$$\begin{aligned}
 -k\Delta u(\mathbf{x}) + \mathbf{a} \cdot \nabla u(\mathbf{x}) &= f(\mathbf{x}) & \text{on } \Omega = [0, 1] \times [0, 1] \\
 u(\mathbf{x}) &= 0 & \text{on } \Gamma
 \end{aligned}
 \tag{5.11}$$

For this example, $a_x = 64$, $a_y = 64$, $k = 1$, and $f(x) = 500 \sin 2\pi(1 - x)(1 - y)$. A reference solution for this problem was generated using a 100×100 element cubic



q

Figure 5.4: 1000 element cubic GFEM reference solution (u) for the 1D unsteady advection-diffusion problem with complex initial condition ($u_{IC}(x)$).

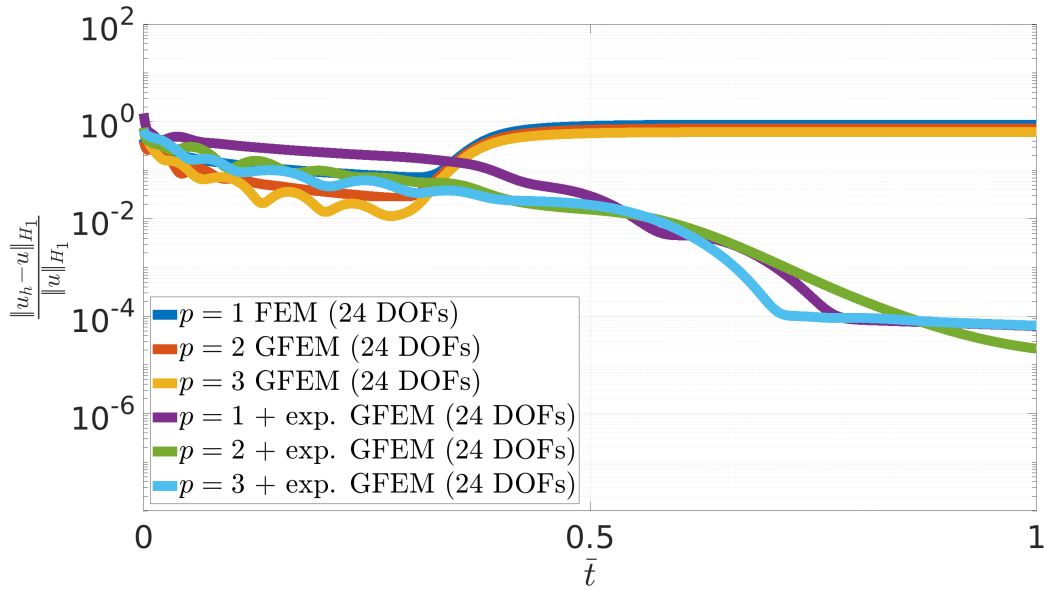
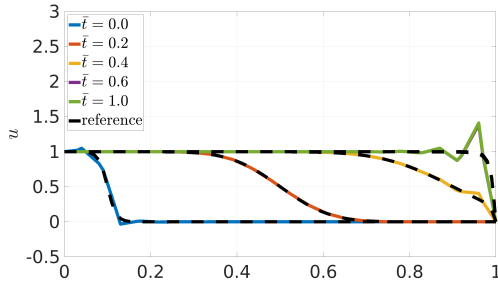
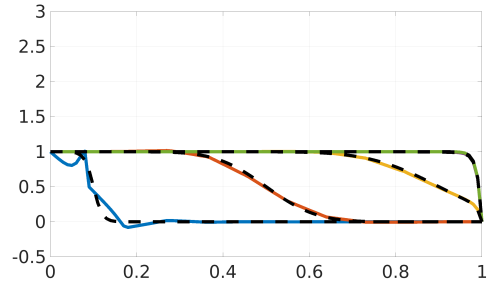


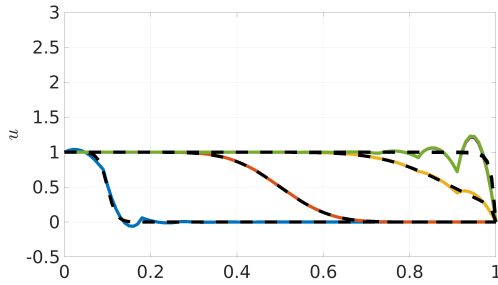
Figure 5.5: Relative H_1 norm $\left(\frac{\|u_h - u\|_{H_1}}{\|u\|_{H_1}}\right)$ versus normalized time (\bar{t}) at 24 DOFs for the 1D unsteady advection-diffusion problem with complex initial condition ($u_{IC}(x)$).



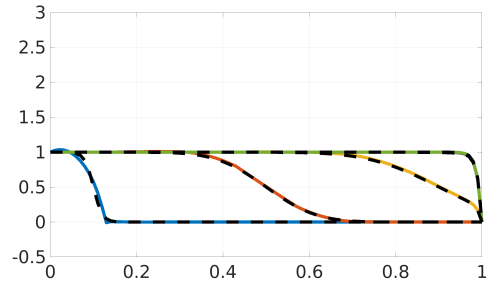
(a) Linear ($p = 1$) FEM



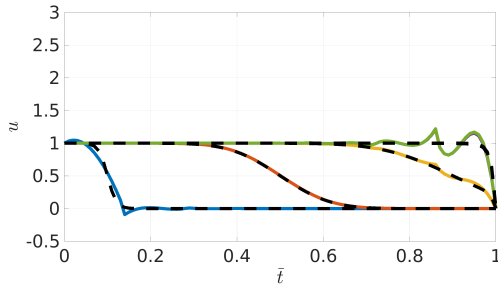
(b) Linear + exponential ($p = 1 + \text{exp.}$) GFEM



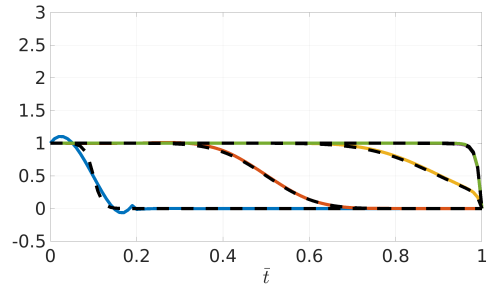
(c) Quadratic ($p = 2$) GFEM



(d) Quadratic + exponential ($p = 2 + \text{exp.}$) GFEM



(e) Cubic ($p = 3$) GFEM



(f) Cubic + exponential ($p = 3 + \text{exp.}$) GFEM

Figure 5.6: 24 DOF linear, quadratic, and cubic solutions (u_h) with ((a), (c), (e)) and without ((b), (d), (f)) exponential enrichments for the 1D unsteady advection-diffusion problem with complex initial condition (u_{IC}).

GFEM solution, and is shown in Fig. 5.8. Steep boundary layers are observed along the $x = 1$ and $y = 1$ walls.

Stability of the $p = 1$ FEM occurs at a grid size greater than or equal to 32×32 elements / 1089 DOFs. This problem was solved over uniform grids using $p = 1$

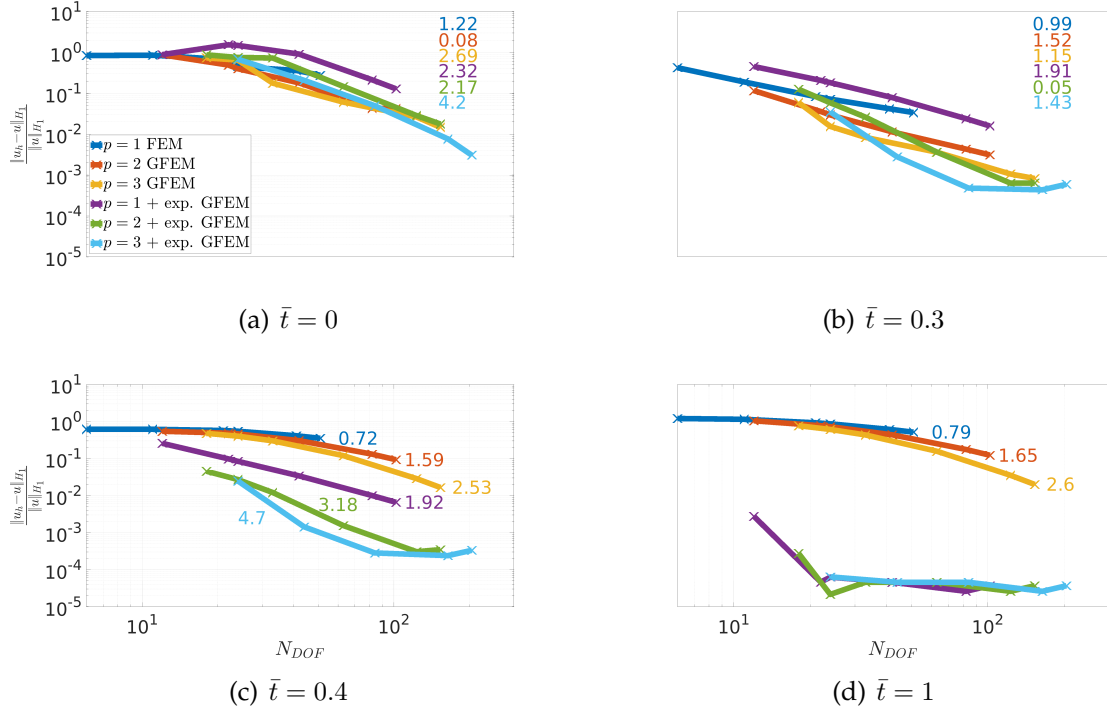


Figure 5.7: Relative H_1 norm $\left(\frac{\|u_h - u\|_{H_1}}{\|u\|_{H_1}}\right)$ versus total degrees of freedom (N_{DOF}) at various normalized times (\bar{t}) before and after a steep boundary layer forms for the 1D unsteady advection-diffusion problem with complex initial condition (u_{IC}).

FEM, $p = 2$, $p = 1 + \text{exp.}$, and $p = 2 + \text{exp.}$ GFEM. The GFEM local approximation space is:

$$\chi_\alpha = \text{span}\left\{1, \frac{x - x_\alpha}{h}, \frac{y - y_\alpha}{h}, e^{\frac{a_x}{k}x} - e^{\frac{a_x}{k}x_\alpha}, e^{\frac{a_y}{k}y} - e^{\frac{a_y}{k}y_\alpha}, e^{\frac{a_x + a_y}{2k}(x+y)} - e^{\frac{a_x + a_y}{2k}(x_\alpha + y_\alpha)}\right\} \quad (5.12)$$

Relative H_1 norm versus total number of degrees of freedom is shown in Fig. 5.9. The vertical dashed line represents 1089 DOFs at which the linear FEM solution becomes stable. Here the addition of linear enrichments only slightly im-

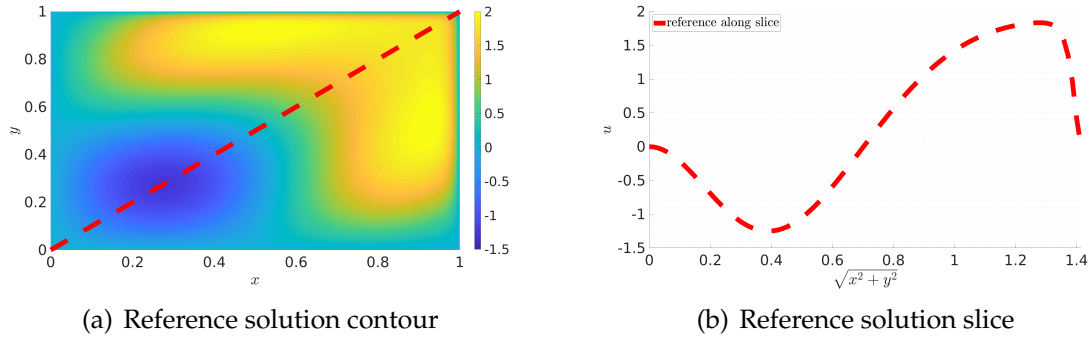


Figure 5.8: Reference solution (u) for the 2D steady advection-diffusion problem with complex volumetric forcing ($f(\mathbf{x})$).

proves the convergence of the GFEM solution over coarse grids, whereas the addition of the exponential enrichments leads to significantly improved convergence. Note that error from the $p = 2 + \text{exp.}$ solution approaches a constant value over fine grids due to their solutions converging to the numerical reference. Solutions along the slice formed 45 degrees to the grid for DOFs 147 ± 3 are shown in Fig. 5.10. Oscillations are observed for both the $p = 1$ FEM and $p = 2$ GFEM solutions, whereas when exponential enrichments are added no oscillations are observed and the $p = 2 + \text{exp.}$ GFEM solution visually matches the reference. Note that these solutions are 147 ± 3 DOFs, which is over a seven times reduction in DOFs from the stable limit of 1089.

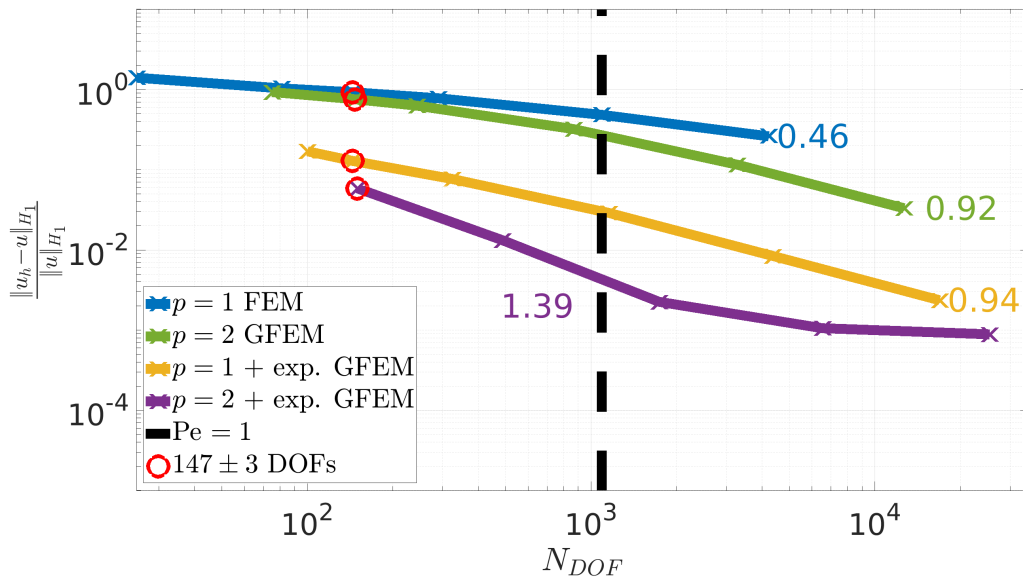


Figure 5.9: Relative H_1 norm $\left(\frac{\|u_h - u\|_{H_1}}{\|u\|_{H_1}}\right)$ versus total degrees of freedom (N_{DOF}) for the 2D steady advection-diffusion problem with complex volumetric forcing ($f(\mathbf{x})$).

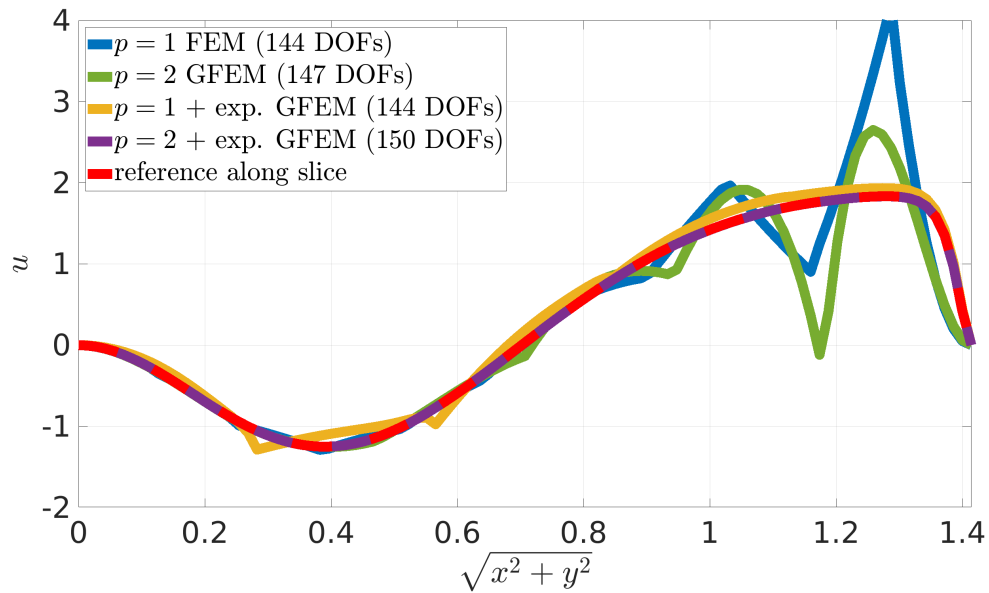


Figure 5.10: 147 ± 3 DOF solutions (u_h) along the slice for the 2D steady advection-diffusion problem with complex volumetric forcing ($f(\mathbf{x})$).

5.2.4 Example: 2D Steady Advection-Diffusion Equation with Advection Skewed to the Grid

Consider another 2D steady problem, this time driven by boundary conditions:

$$\begin{aligned} -k\Delta u(\mathbf{x}) + \mathbf{a} \cdot \nabla u(\mathbf{x}) &= 0 & \text{on } \Omega = [0, 1] \times [0, 1] \\ u(\mathbf{x}) &= d(\mathbf{x}) & \text{on } \Gamma \end{aligned} \tag{5.13}$$

where $d(\mathbf{x})$ are the Dirichlet boundary conditions given in Fig. 5.11. Note two discontinuities exist along the boundary at $(x, y) = (0, 0.2)$ and $(x, y) = (1, 0)$. For this problem, $k = \frac{1}{64\sqrt{2}}$, and $\mathbf{a} = [\cos \theta, \sin \theta]$, where θ represents the flow direction of the solution u . Reference solutions to this problem for $\theta = [22.5, 45, 67.5]$ degrees were generated using 400×400 element, $p = 1$ FEM, and solution are shown in 5.12. For all θ , a steep boundary layer is formed along the wall $(1, y)$, with the boundary layer thickness increasing as θ increases. For $\theta = 45$ and 67.5 degrees a boundary layer also forms along the $(x, 1)$ wall. This set of problems were solved numerically over uniform grids using $p = 1$ FEM, $p = 2$, $p = 1 + \text{exp.}$, and $p = 2 + \text{exp.}$ GFEM. The GFEM local approximation space is given by Eq. 5.12.

Note since the source of flow comes directly from the boundary conditions (specifically where $u(\mathbf{x}) = d(\mathbf{x}) = 1$ on Γ), traditional convergence rates for this example problem are not well established. That is, along the walls $(x, 0)$ and $(0, y)$, the discontinuities are approximated by a finite number of elements, resulting in

either an over- or under-prediction of the true flow through the boundary. Specific to this problem, the inclusion of $u(0, 0.2) = 1$ in Fig. 5.11 results in an over-prediction of the flow since for grid size h , a linear interpolation from $u(0, 0.2) = 1$ to $u(0, 0.2 + h) = 0$ occurs. Similarly, the exclusion at $(1, 0)$ will result in an under-prediction of the flow. To ensure the FEM and GFEM solutions have identical boundary conditions over a specific grid discretization, the nodes along the walls $(x, 0)$ and $(0, y)$ are not enriched. This results in a linear interpolation of the discontinuities along these walls, regardless of the approximation space provided.

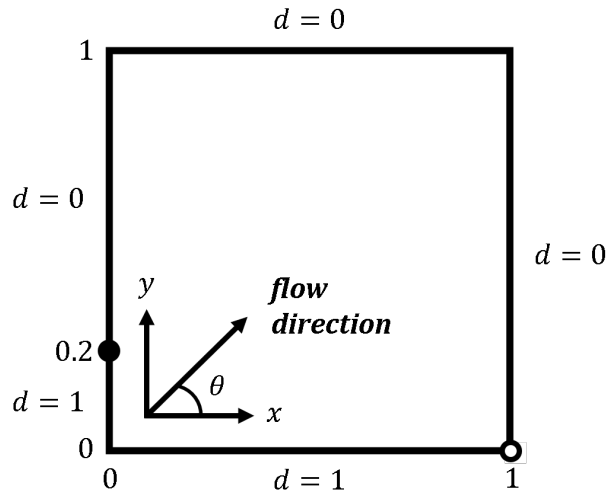


Figure 5.11: Dirichlet boundary conditions ($d(\mathbf{x})$) for the 2D advection skewed to the grid problem.

Absolute error contours for $\theta = 22.5$ degrees are shown in Fig. 5.13 for 10×10 and 40×40 element solutions. Here it is observed for the 10×10 element solutions, oscillations are present in the $p = 1$ and $p = 2$ solutions without the exponential enrichments. When the exponential enrichments are used, no oscillations are present.

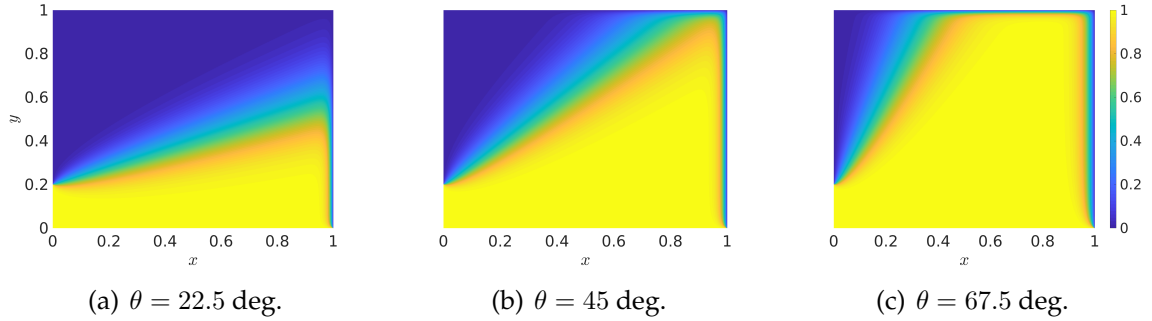


Figure 5.12: 400×400 element, linear FEM reference solutions (u) at various flow angles (θ) for the 2D advection skewed to the grid problem.

However, as mentioned prior, the over- and under-prediction of the flow through the boundary results in a propagation of error in the domain along the flow direction θ . Unless specific enrichments are used to capture the boundary exactly, only h -refinement is capable of reducing the error propagation observed. This is shown in the 40×40 solutions, where all the solutions with and without exponential enrichments visually return similar error, and both the magnitude and area of influence of the propagated error is reduced. Note that minor oscillations are still observed for the $p = 1$ FEM solutions. Similar results are obtained for $\theta = 45$ and 67.5 degrees, as shown in Figs. 5.14 and 5.15, respectively, except the oscillations are observed along the $(x, 1)$ wall as well. Relative H_1 norm versus total degrees of freedom is shown in Fig. 5.16 for these three flow angles. Here the oscillations in the coarse grid, $p = 1$ and $p = 2$ solutions result in larger errors than those with the exponential enrichments at the same number of degrees of freedom. Since the exponential enrichments capture exactly the steep boundary layers forming along walls $(x, 0)$ and $(0, y)$, the dominant error in the GFEM solutions comes from the

boundary conditions.

This is observed in Fig. 5.17, which shows the same relative H_1 norm now versus $\frac{1}{h}$. Here it is shown that the $p = 1 + \text{exp.}$ GFEM and $p = 2 + \text{exp.}$ GFEM solutions are nearly identical at every grid size studied, indicating only h -refinement is capable of improving error for the given approximation spaces. Additionally for fine grids where the $p = 2$ GFEM solution no longer exhibits instability, the error returned is almost identical to the exponential solutions.

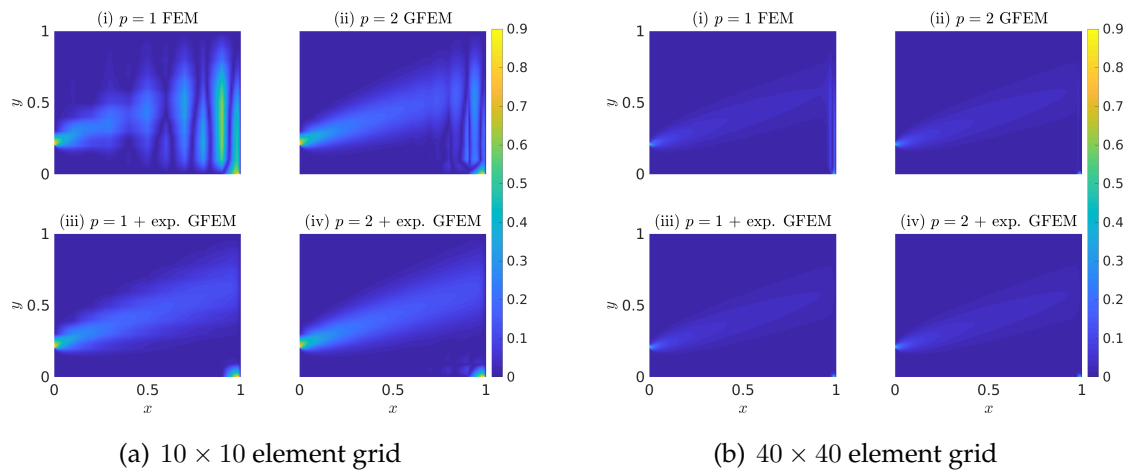


Figure 5.13: Absolute error contours ($|u_h - u|$) for $\theta = 22.5$ deg for the 2D advection skewed to the grid problem.

5.2.5 Example: 2D Unsteady Advection-Diffusion Equation with Periodic Boundary Conditions

Finally, consider the 2D unsteady advection-diffusion equations with periodic boundary conditions:

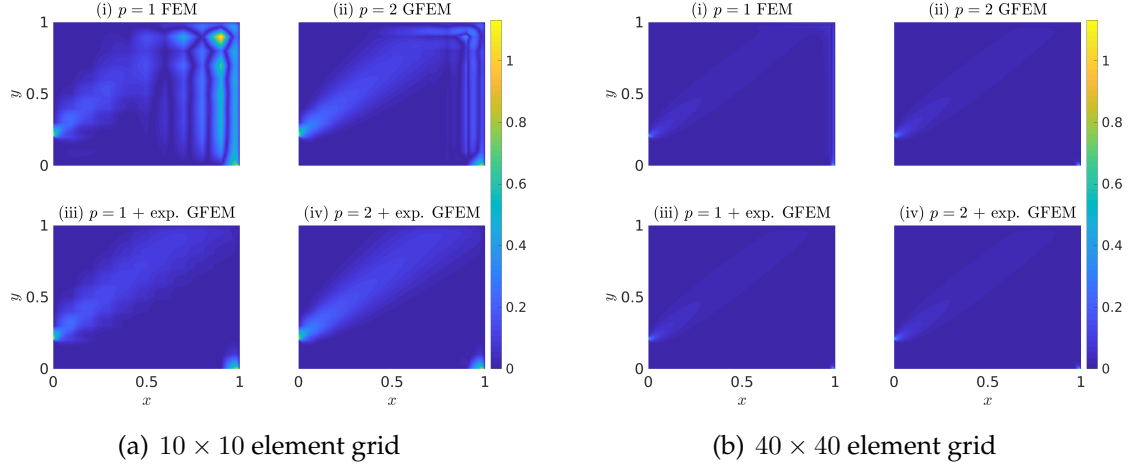


Figure 5.14: Absolute error contours ($|u_h - u|$) for $\theta = 45$ deg for the 2D advection skewed to the grid problem.

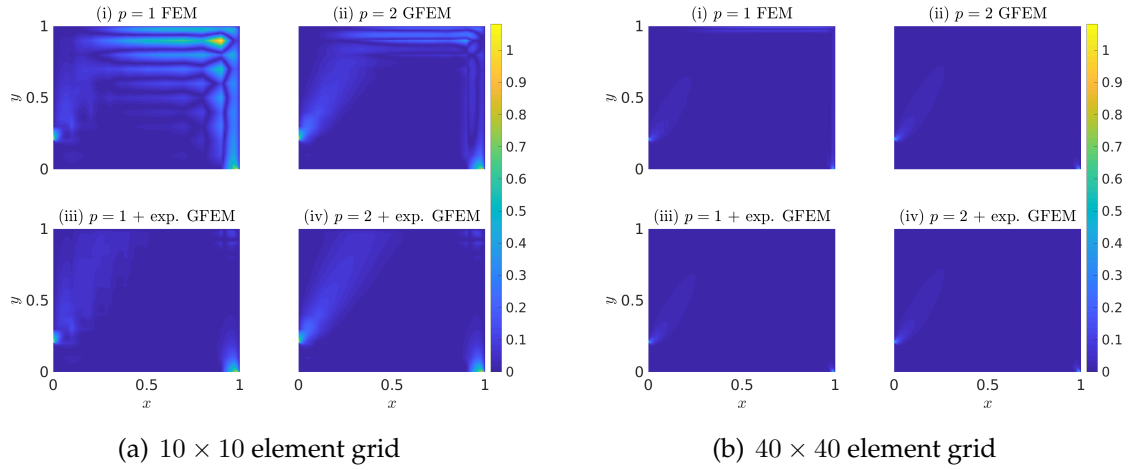


Figure 5.15: Absolute error contours ($|u_h - u|$) for $\theta = 67.5$ deg for the 2D advection skewed to the grid problem.

$$\begin{aligned}
 \frac{\partial u(\mathbf{x}, t)}{\partial t} &= k \Delta u(\mathbf{x}, t) - \nabla \cdot (\mathbf{a}u(\mathbf{x}, t)) && \text{on } \Omega = [0, 1] \times [0, 1] \\
 u &= \sin^2(64\pi t) \sin\left(\frac{\pi}{2}(x-1)(y-1)\right) && \text{on } \Gamma = \{0, 1\} \times \{0, 1\} \\
 u(\mathbf{x}, 0) &= 0 && \text{on } \Omega = [0, 1] \times [0, 1]
 \end{aligned} \tag{5.14}$$

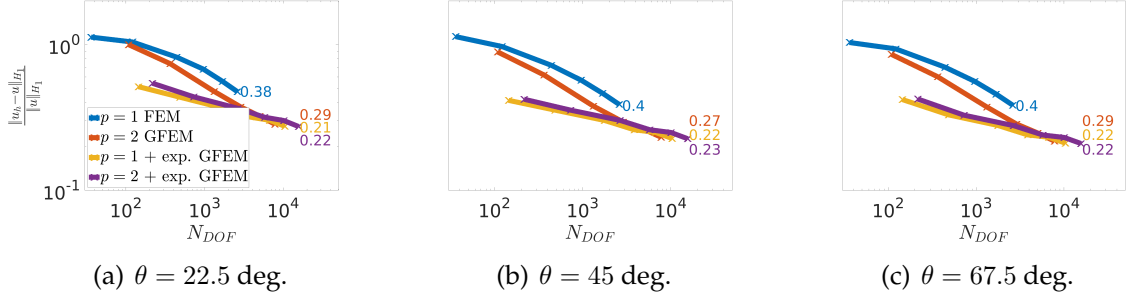


Figure 5.16: Relative H_1 norm $\left(\frac{\|u_h - u\|_{H_1}}{\|u\|_{H_1}}\right)$ versus total degrees of freedom (N_{DOF}) at various flow angles (θ) for the 2D advection skewed to the grid problem.

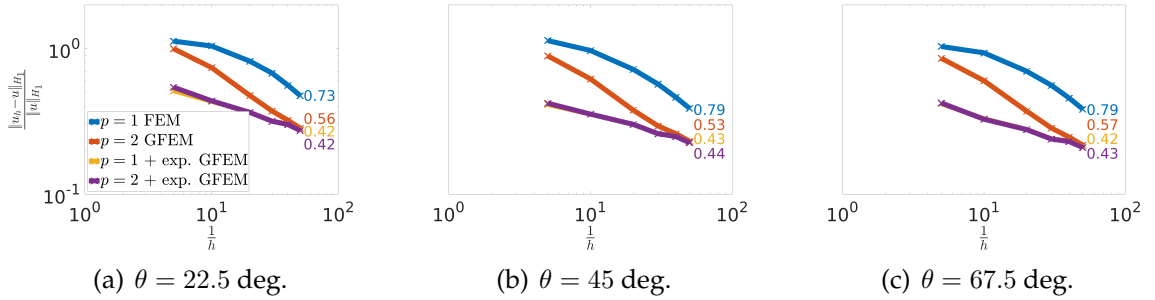


Figure 5.17: Relative H_1 norm $\left(\frac{\|u_h - u\|_{H_1}}{\|u\|_{H_1}}\right)$ versus $\frac{1}{h}$ at various flow angles (θ) for the 2D advection skewed to the grid problem.

For this example, $a_x = 64$, $a_y = 64$, $k = 1$, and $t = [0, \frac{3}{64}]$. For all upcoming figures, time t is normalized to be $\bar{t} = [0, 1]$. The boundary conditions have a period of $T = \frac{1}{64}$, thus three full periods are observed. A reference solution for this problem was generated using an 81×81 element cubic GFEM solution, and is shown in Fig. 5.18 for various normalized times, \bar{t} . The Crank-Nicolson method is used for discretization of the temporal term with 40 time steps. Initially there is no presence of advection, but around $\bar{t} = \frac{1}{3}$, a boundary layer forms around $(x, y) = (1, 1)$. Stability of the linear FEM solution occurs at a grid size greater than

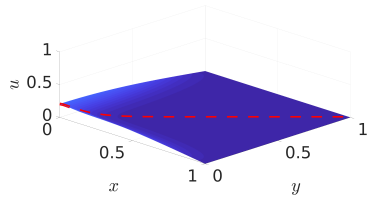
or equal to 32×32 elements / 1089 DOFs. Similar to the 2D steady case, this problem was solved over uniform grids using linear $p = 1$ FEM, and $p = 2$, $p = 1 + \text{exp.}$, and $p = 2 + \text{exp.}$ GFEM. The GFEM local approximation space is given in 5.12. Relative H_1 norms of the 147 ± 3 DOF solutions versus normalized time are shown in 5.19. At $\bar{t} = 0$, all solutions are trivial, thus no error is introduced. For the next few time steps it is observed initially the presence of upwind behavior is small, thus the polynomial solutions with and without stabilized enrichments agree relatively well. However, starting around $\bar{t} = 0.225$ oscillations in the polynomial solutions without exponential enrichments are observed and improved errors are noted with those which use them. 147 ± 3 DOF solutions along the contour slice are presented in Fig. 5.20. Similar to the steady cases, oscillations are observed near the steep boundary layer point $(x,y) = (1,1)$ for the $p = 1$ FEM and $p = 2$ GFEM solutions *without* exponential enrichments. Introduction of the exponential enrichments results in an error spread that is more uniform, with no oscillations present in the numerical solutions even though the total DOFs are far fewer than the stable limit of 1089 DOFs. Lastly, the convergence rates of the relative H_1 norm versus total degrees of freedom is presented in Fig. 5.21. Initially before the boundary begins to form around $\bar{t} = 0.225$, the errors in the solutions with and without the exponential enrichments are similar. However, afterwards the exponential solutions return significantly reduced errors than those without.

5.3 General Discussion

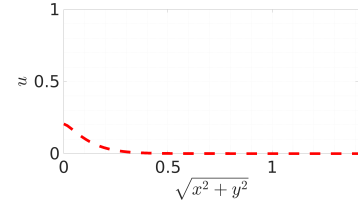
Chapter 4 details the potential of GFEM to naturally stabilize highly advective problems through comparison with classical stabilized methods using a consistent decomposition with the variational multiscale method. Additionally, Chapter 4 provides insights into stabilizing linear differential operators based on fundamental solutions, suggesting that GFEM may stabilize any linear differential operator. Unlike stabilized methods, no restrictions are placed on the enrichment selection process, thus allowing the choice of solution-tailored enrichments while maintaining local solution conformity. For the class of advection-diffusion problems considered in this chapter, the results demonstrate significant improvements when using solution-tailored enrichments for both stability and error convergence, relative to linear FEM and GFEM using only polynomial enrichments. An advantage of using fundamental solutions as enrichments is the independence of boundary conditions and forcing.

For the advection-diffusion problems considered, which assume constant rates of advection and diffusion, the fundamental solutions are exponential functions. For spatially variant rates of advection, $\mathbf{a}(\mathbf{x})$, and diffusion, $k(\mathbf{x})$ (such as the advection in a rotating flow field presented in [5]), or a different linear operator, other enrichments are likely necessary. For more complex problems, where fundamental solutions may not be theoretically derivable, enrichments may be obtainable using

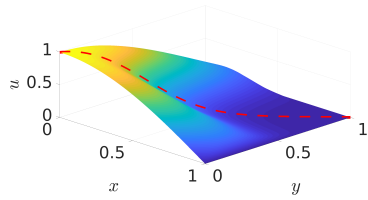
the GFEM global-local method [71]. Also, note that for all the examples presented, the entire domain Ω was enriched. However, since the fine scales in the GFEM approach depend on the residual error of the coarse scales, DOFs in the GFEM may be further reduced by enriching only a portion of the domain where the steep boundary layer is present.



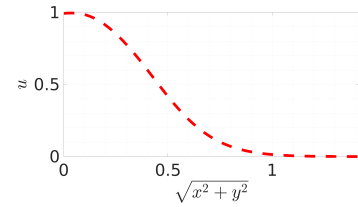
(a) $\bar{t} = 0.05 = 0.15T$ reference contour



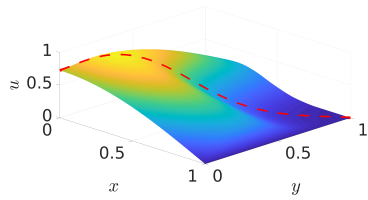
(b) $\bar{t} = 0.05 = 0.15T$ reference slice



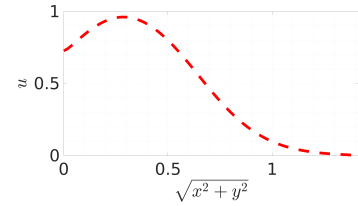
(c) $\bar{t} = 0.175 = 0.525T$ reference contour



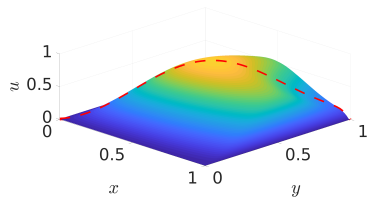
(d) $\bar{t} = 0.175 = 0.525T$ reference slice



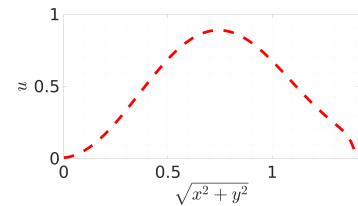
(e) $\bar{t} = 0.225 = 0.675T$ reference contour



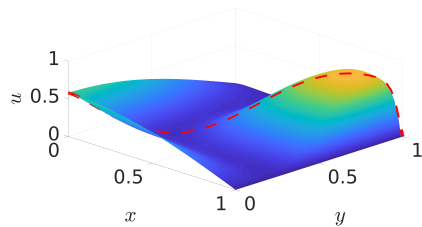
(f) $\bar{t} = 0.225 = 0.675T$ reference slice



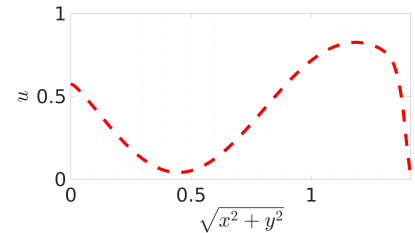
(g) $\bar{t} = 0.325 = 0.975T$ reference contour



(h) $\bar{t} = 0.325 = 0.975T$ reference slice



(i) $\bar{t} = 0.425 = 1.275T$ reference contour



(j) $\bar{t} = 0.425 = 1.275T$ reference slice

Figure 5.18: Reference solution (u) for the 2D unsteady advection-diffusion problem with periodic boundary conditions.

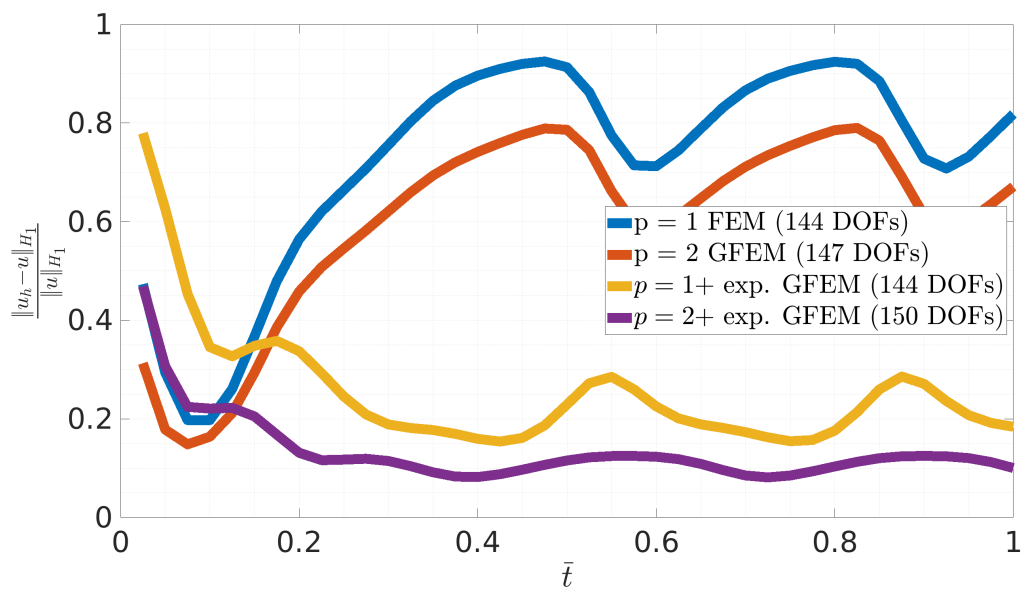


Figure 5.19: Relative H_1 norm $\left(\frac{\|u_h - u\|_{H_1}}{\|u\|_{H_1}}\right)$ versus normalized time (\bar{t}) for the 2D unsteady advection-diffusion problem with periodic boundary conditions.

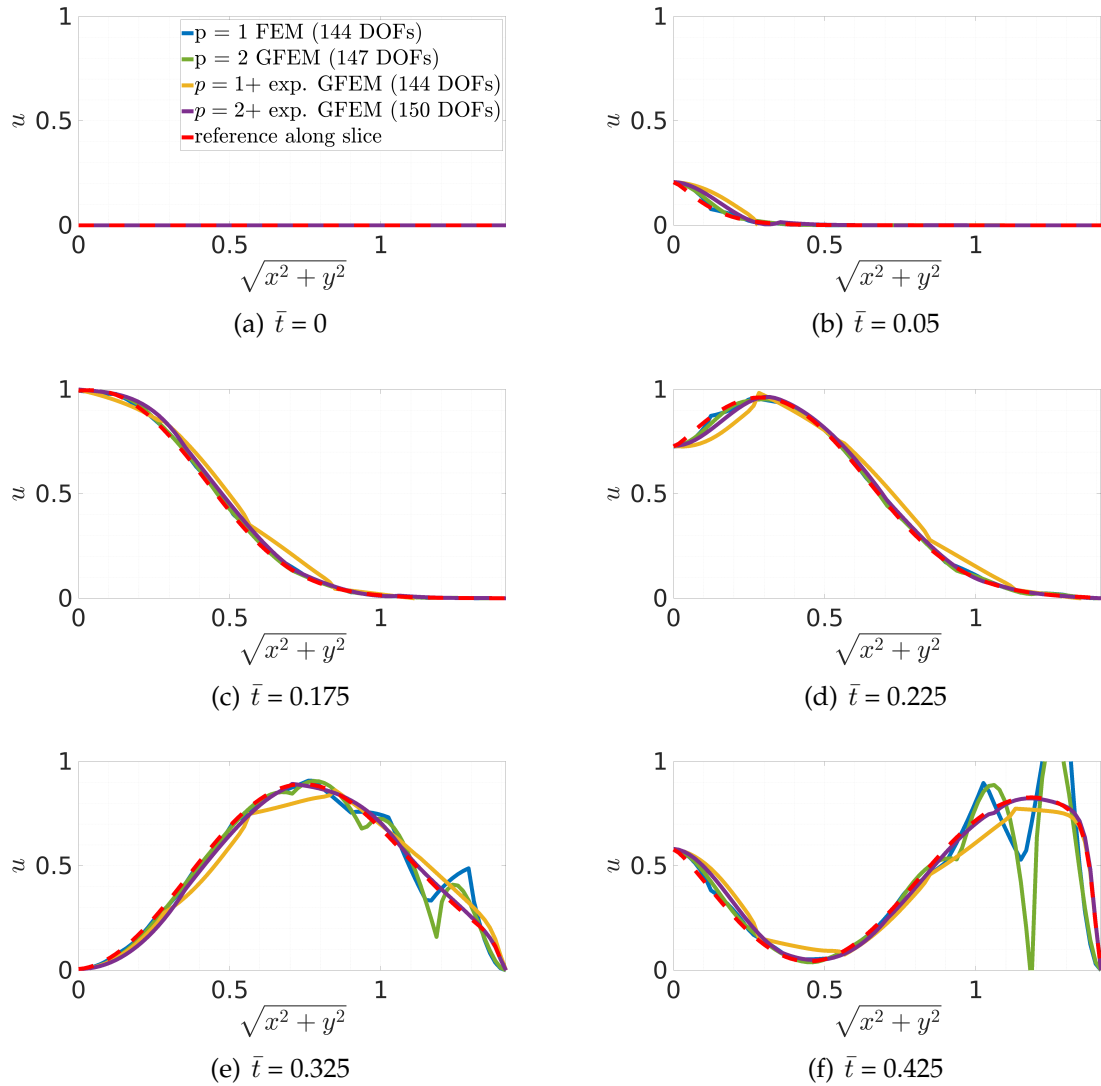


Figure 5.20: 147 ± 3 DOF solutions (u_h) along slice for the 2D unsteady advection-diffusion problem with periodic boundary conditions.

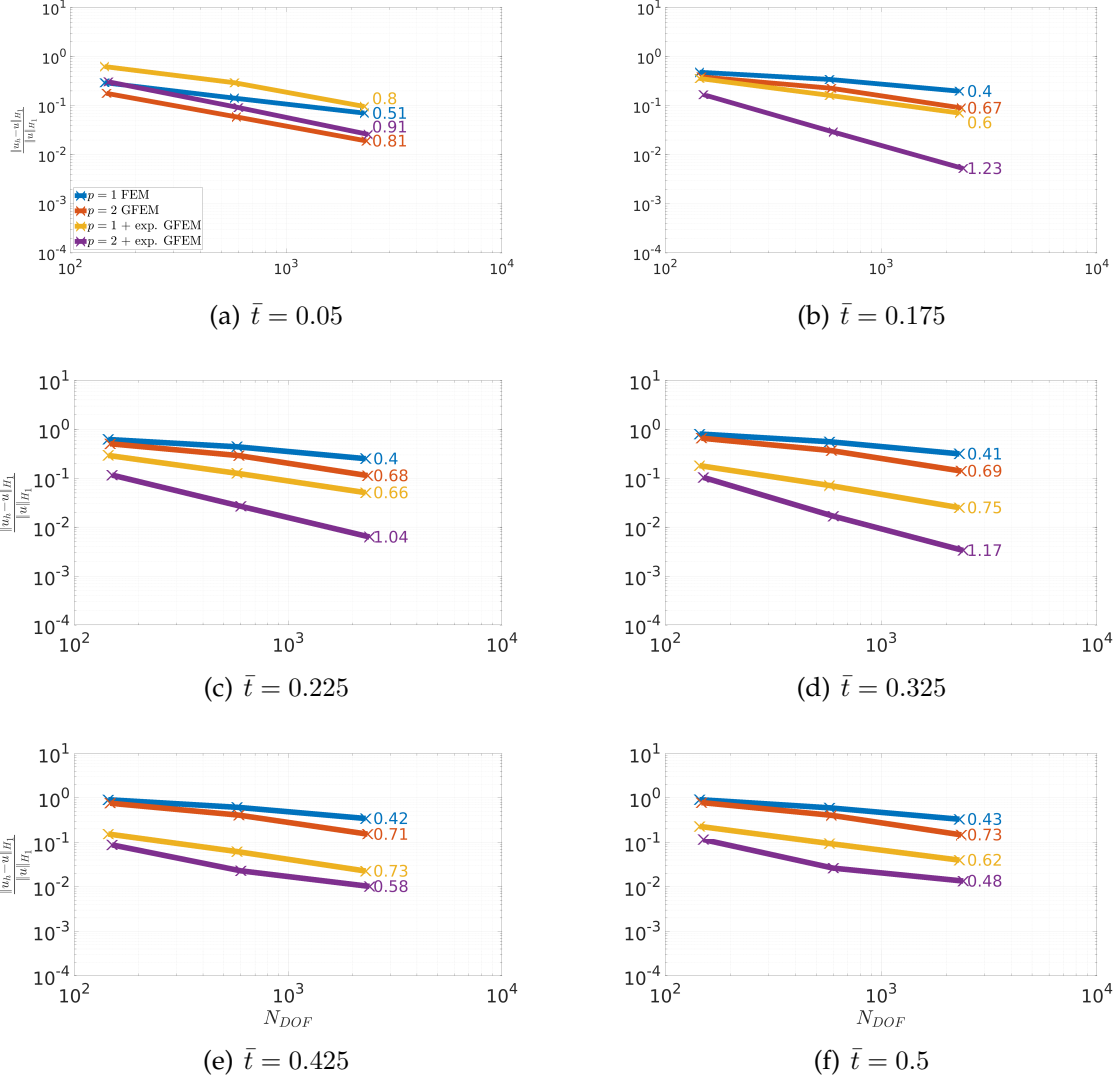


Figure 5.21: Relative H_1 norm $\left(\frac{\|u_h - u\|_{H_1}}{\|u\|_{H_1}}\right)$ versus total degrees of freedom (N_{DOF}) at various normalized times (\bar{t}) before and after a step boundary layer forms with periodic boundary conditions.

Chapter 6

GFEM Solution to the Burgers' Equation

This chapter summarizes work to extend upon the advection-diffusion equation work in Chapter 6 by detailing the exploration of solution-tailored enrichments applied to the one-dimensional, unsteady Burgers' equation. The viscous Burgers' equation is identical to the advection-diffusion equation, except the advection coefficient is replaced by the solution variable, u , thus resulting in a nonlinear term. This equation was first introduced by Bateman in [79] as a relatively simple equation to explore discontinuous solutions as the kinematic viscosity tends towards zero. It was not until many years later that Burgers explored this equation in [80] as a nonlinear equation with similar phenomena to turbulence. Nowadays, the Burgers' equation is known to have physical relevance for problems which include: viscous flows, shock theory, gas dynamics, cosmology, traffic flow, and quantum computing [81]. The Burgers' equation has many features similar to the Navier-Stokes equations and is used to clarify the interaction between transient, dissipative, and nonlinear advective terms. Specifically, the Burgers' equation contains an inertial

and dissipation range similar to turbulence in the Navier-Stokes equations [82, 83]. As such, numerical simulation of the Burgers' equation presents a challenge when inertial effects dominate the solution, analogous to challenges associated with numerically solving Navier-Stokes equations with high Reynolds numbers. These highly advective problems often demand ultra-fine discretizations to resolve the multiscale behavior of the system accurately; Otherwise, nonphysical oscillations arise in the solution.

The outline of this chapter is as follows: first is a summary of the governing equations for the viscous Burgers' equation, formulation of the GFEM nonlinear system of equations, and linearization using Newton-Raphson. Next, the inviscid Burgers' equation is presented, followed by a discussion on the formation of shocks in the domain and numerical stability. Finally, numerical examples are presented for the GFEM solution to the unsteady one-dimensional Burgers' equation, along with a general discussion of the results.

6.1 Viscous Burgers' Equation

6.1.1 Governing equation

The one-dimensional viscous Burgers' equation is given by the following: find u such that:

$$\begin{aligned}
\frac{\partial u}{\partial t} + u \frac{\partial u}{\partial x} - \nu \frac{\partial^2 u}{\partial x^2} &= 0 \quad \text{on } \Omega \\
u(x, 0) &= u_{IC}(x) \quad \text{on } \Omega \\
u(x, t) &= g_{\Gamma_D}(x, t) \quad \text{on } \Gamma_D \\
\frac{\partial u(x, t)}{\partial x} &= g_{\Gamma_N}(x, t) \quad \text{on } \Gamma_N
\end{aligned} \tag{6.1}$$

where when referring to fluids, ν is the kinematic viscosity, and $u(x, t)$ is the fluid velocity.

6.1.2 GFEM Nonlinear System of Equations

Substitution of the GFEM approximation Eq. 2.10 into Eq. 6.1 and following the Galerkin method procedure outlined in Chapter 2 results in the following nonlinear system of equations:

$$\mathbf{M}\dot{\mathbf{c}}(t) = -(\mathbf{A}(t) + \mathbf{K})\mathbf{c}(t) + \mathbf{f}_{\Gamma_N}(t) \tag{6.2}$$

where

$$\mathbf{M} = \int_{\Omega} \phi \phi^T d\Omega \quad (6.3)$$

$$\mathbf{A}(t) = \int_{\Omega} \phi \phi^T \mathbf{c}(t) \frac{\partial \phi^T}{\partial x} d\Omega \quad (6.4)$$

$$\mathbf{K} = \nu \int_{\Omega} \frac{\partial \phi}{\partial x} \frac{\partial \phi^T}{\partial x} d\Omega \quad (6.5)$$

$$\mathbf{f}_{\Gamma_N}(t) = \int_{\Gamma_N} \phi g_{\Gamma_N}(x, t) d\Gamma_N \quad (6.6)$$

After applying the Crank-Nicolson method (Eq. 2.13) and enforcing Dirichlet boundary conditions (Eq. 2.15) to Eq. 6.2, the final system of equations is:

$$[\tilde{\mathbf{M}}(\mathbf{c}^{n+1}) + \mathbf{M}_{\Gamma_D}] \mathbf{c}^{n+1} = \tilde{\mathbf{b}} + \mathbf{b}_{\Gamma_D} \quad (6.7)$$

where $\tilde{\mathbf{M}}(\mathbf{c}^{n+1}) = \frac{2}{\Delta t} \mathbf{M} + \mathbf{A}(\mathbf{c}^{n+1}) + \mathbf{K}$, $\tilde{\mathbf{b}} = \mathbf{f}_{\Gamma_N}(t^{n+1}) + [\mathbf{f}_{\Gamma_N}(t^n) - (\mathbf{A}(\mathbf{c}^n) + \mathbf{K})\mathbf{c}^n]$, and \mathbf{M}_{Γ_D} and \mathbf{b}_{Γ_D} are defined in Eqs. 2.16 and 2.17, respectively. Notice the extreme similarity in Eq. 6.7 with the final system of equations for the advection-diffusion equation in Eq. 5.7. The subtle difference between the two is that the system of equations for the Burgers' equation represent a *nonlinear* system of equations, and thus additional work must be done to obtain the solution vector at each time step. This is the focus of the next section.

6.1.3 Iteration of the Nonlinear System using the Newton-Raphson Method

Eq. 6.7 is a nonlinear system of equations with knowns \mathbf{c}^n and unknowns \mathbf{c}^{n+1} . Using the Newton-Raphson method, the solution may be iterated to solve for the solutions at the $n + 1$ time step. To do so, assume $\mathbf{c}^{n+1} = \mathbf{c}^n + \epsilon$, where solutions at the previous time steps n are an approximation of the $n+1$ solution, and ϵ is a small correction. First, applying this above decomposition to the nonlinear matrix term ($\mathbf{A}(t^{n+1})$) product with solution coefficients at the $n + 1$ time step (\mathbf{c}^{n+1}) simplify to the following after neglecting the underlined $\mathcal{O}(\epsilon^2)$ terms:

$$\begin{aligned} \mathbf{A}(\mathbf{c}^{n+1})\mathbf{c}^{n+1} &\approx \mathbf{A}(\mathbf{c}^n)\mathbf{c}^n + \left(\mathbf{A}(\mathbf{c}^n) + \int_{\Omega} \phi\phi^T \left(\frac{\partial\phi}{\partial x} \mathbf{c}^n \right) d\Omega \right) \epsilon + \underline{\mathcal{O}(\epsilon^2)} \\ &\approx \mathbf{A}(\mathbf{c}^n)\mathbf{c}^n + \left(\mathbf{A}(\mathbf{c}^n) + \tilde{\mathbf{A}}(\mathbf{c}^n) \right) \epsilon + \underline{\mathcal{O}(\epsilon^2)} \end{aligned} \quad (6.8)$$

Substitution of $\mathbf{c}^{n+1} = \mathbf{c}^n + \epsilon$ and Eq. 6.8 into Eq. 6.7 results in the following system of equations to solve for the corrections ϵ :

$$\tilde{\mathbf{G}}\epsilon = \tilde{\mathbf{g}} \quad (6.9)$$

where $\tilde{\mathbf{G}} = \tilde{\mathbf{M}}(\mathbf{c}^n) + \tilde{\mathbf{A}}(\mathbf{c}^n) + \mathbf{M}_{\Gamma_D}$ and $\tilde{\mathbf{g}} = \tilde{\mathbf{b}} + \mathbf{b}_{\Gamma_D} - (\tilde{\mathbf{M}}(\mathbf{c}^n) + \mathbf{M}_{\Gamma_D})\mathbf{c}^n$. Finally, iterate over Eq. 6.9 until some residual is converged.

6.2 Inviscid Burgers' Equation

6.2.1 Governing Equation

The inviscid Burgers' equation represents a limiting case where the kinematic viscosity tends toward zero ($\nu \rightarrow 0$). The resulting inviscid Burgers' equation is the following: find u such that:

$$\begin{aligned}\frac{\partial u}{\partial t} + u \frac{\partial u}{\partial x} &= 0 \quad \text{on } \Omega \\ u(x, 0) &= u_{IC}(x) \quad \text{on } \Omega \\ u(x, t) &= g_{\Gamma_D}(t) \quad \text{on } \Gamma_D \\ \frac{\partial u(x, t)}{\partial x} &= g_{\Gamma_N}(t) \quad \text{on } \Gamma_N\end{aligned}\tag{6.10}$$

Using the method of characteristics an implicit solution to Eq. 6.10 can be constructed. Readers are directed to [84] for additional details on this procedure. The resulting implicit solution is given by $u(x, t) = u_{IC}(x - ut) = u_{IC}(\xi)$, with a characteristic trajectory $x = ut + \xi$, where ξ is an arbitrary point on the x -axis of the x - t plane. Note the formulation of the GFEM system of equations for this inviscid case is identical to that of Eq. 6.9 with \mathbf{K} removed.

6.2.2 Formation of Shocks

In the inviscid case, a discontinuity ("shock") will form in the domain if $u'_{IC}(x) < 0$. This work's notion of a shock is assumed to be inclusive of any solution which con-

tains a steep gradient. Therefore, the distinction between the inviscid and viscous Burgers' equation for shock formation is the discontinuity that appears in the domain. Additionally, the time when the discontinuity first occurs is denoted the breaking time and is given by:

$$t_b = \frac{-1}{\min u'_{IC}(x)} \quad (6.11)$$

If $u_{IC}(x)$ crosses the x -axis at x_b , such that $u_{IC}(x_b) = 0$ and $u'_{IC}(x_b) < 0$, the shock that forms will be stationary at x_b . In the case where $u'_{IC}(x) < 0$ and $u_{IC}(x)$ does *not* cross the x -axis, the shock formed will be moving. If $u_{IC}(x) > 0$ the shock will travel in the positive x -direction with time, otherwise for $u_{IC}(x) < 0$ the shock will travel in the negative x -direction with time. This may be demonstrated by considering a series of Riemann problems represented by the following initial conditions:

$$u_{IC}(x) = \begin{cases} b + 1 & x \leq \frac{1}{2} \\ b + 2(1 - x) & \frac{1}{2} < x < \frac{3}{2} \\ b - 1 & \frac{3}{2} \leq x \end{cases} \quad (6.12)$$

where b is an arbitrary value to translate the initial condition. The resulting solution to Eq. 6.10, with initial conditions Eq. 6.12 for values of $b = \{-1.25, -1, 0, 0.5, 1, 1.25\}$, is shown in Fig 6.1. Observe that the initial problem is strictly negative for $b = -1.25$, and the forming shock moves to the left with time. If $b = 1.25$, the

initial problem is strictly positive and moves to the right. The remaining values of b cross the x -axis at some point and form a stationary wave. Addressing moving shocks is outside of the scope of this paper, as the authors are concerned with addressing stability concerns in the GFEM. Thus, this work considers only stationary shocks for subsequent numerical examples. However, the authors note that previous work on GFEM to solve time-dependent problems indicates a promise to handle transient, local behavior. The authors direct the readers to [15] for work on GFEM solution to highly localized sharp, transient thermal gradients as an example of such application.

6.2.3 A Note on Stability

Recall the viscous Burgers' equation (Eq. 6.1) is form identical to the advection-diffusion equation, where the advection coefficient is replaced by the solution variable, u . For advection-diffusion equations, the Péclet number is considered for stability of the linear FEM. Specifically, for linear FEM solution over uniform grid size, h , $Pe = \frac{ah}{2\nu} > 1$ results in spurious oscillations, where a and ν are the rate of advection and rate of diffusion, respectively. Rearranged, the required element size to eliminate spurious oscillations in the numerical solution is determined by $h \leq \frac{2\nu}{a}$. Using this, a conservative estimate for stability of the Burgers' equation is obtained by replacing a with the absolute maximum value of u at $t = 0$. Specifically, for $\max |u(x, 0)| = \max |u_{IC}(x)|$, then $h \leq \frac{2\nu}{\max |u_{IC}(x)|}$. Note in the limit $\nu \rightarrow 0$,

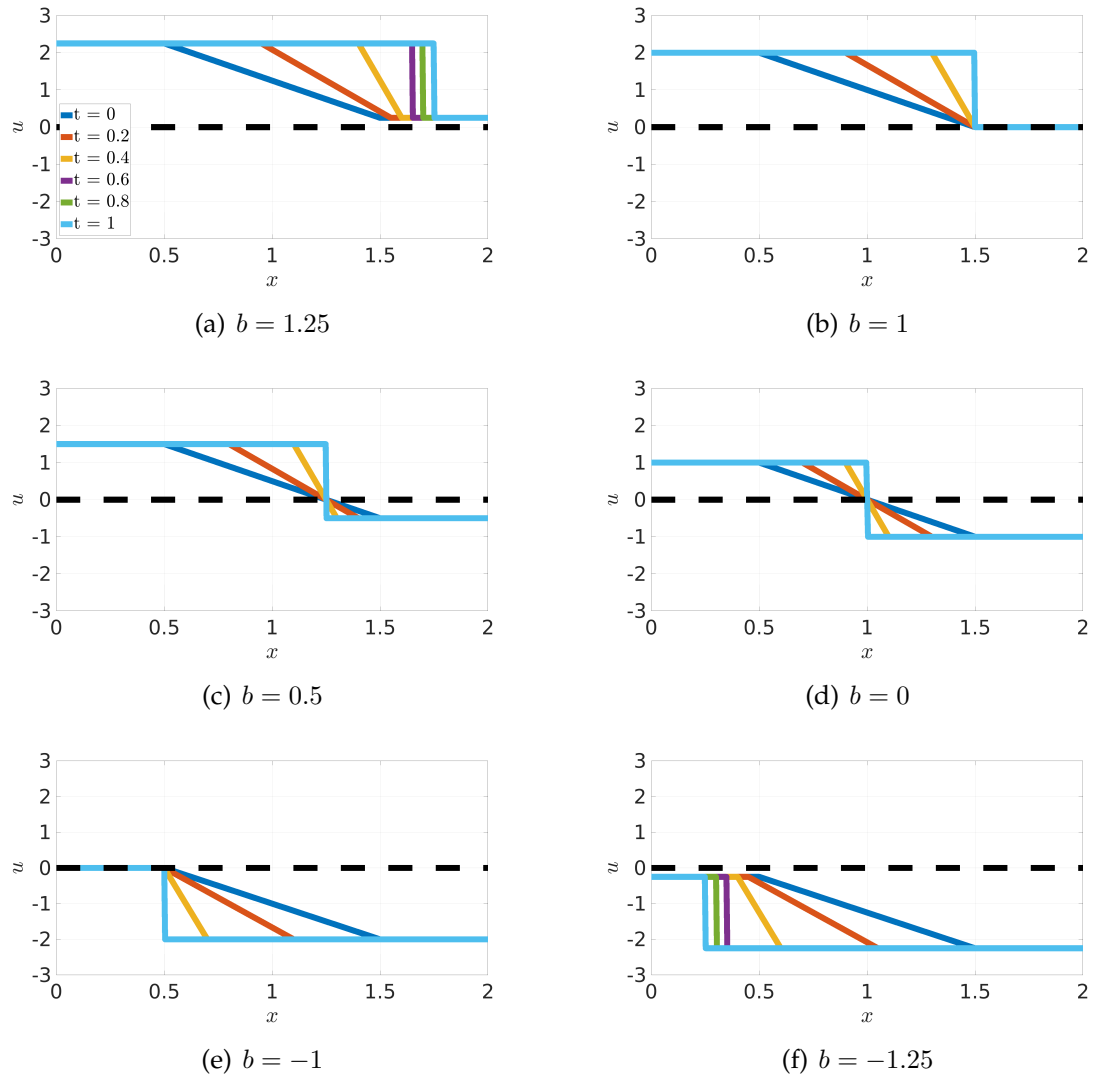


Figure 6.1: Riemann solutions (u) for various initial conditions ($u_I C(x)$).

the required grid size for a stable solution in linear FEM is unachievable.

6.3 Numerical Results

This section presents GFEM solutions of the one-dimensional Burgers' equation.

For the following examples, please consider:

1. All enrichments are shift by their nodal values to retain the physical meaning of the standard FEM DOFs at each node.
2. Special consideration is necessary to integrate the non-polynomial enrichment functions accurately. The computational cost of integrating the enrichments is trivial in the following examples since the elemental matrices are not time-dependent. Such, the following work uses a conservative number of Gaussian quadrature points for each grid refinement. For example, we use ten-point Gaussian quadrature on the most refined meshes considered (approx. $\frac{1}{80}$ element size); while we use sixty-point Gaussian quadrature for the coarsest meshes considered (approx. $\frac{1}{10}$ element size). For problems where the elemental matrices are time-dependent, evaluation of the elemental matrices at each time step using Gaussian quadrature may increase costs considerably. More efficient integration strategies may be beneficial for these problems, such as the Gauss-Laguerre quadrature, an extension of Gaussian quadrature for integrating exponential functions.
3. *A priori* error estimates are well-known for polynomial approximation spaces: for $\Omega \subset \mathbb{R}^n$ with Lipschitz boundary, a p -degree polynomial solution converges in the L_2 and H_1 norm versus total degrees of freedom at a theoretical convergence rate of $\frac{p+1}{n}$ and $\frac{p}{n}$, respectively. However, for approximation spaces containing solution-tailored enrichments, theoretical convergence rates are not formally developed. Insights into convergence rates for

solution-tailored enrichments are provided by considering convergence plots. Unless specified, convergence rates in the L_2 and H_1 norm versus total degrees of freedom use the finest two grids studied. For a sufficiently smooth solution using polynomial + non-polynomial enrichments, convergence rates are similar to those of the polynomial approximation spaces. An exception is when the numerical solution is of the same order of numerical precision as the reference solution. Same order numerical precision is often the case when using solution-tailored enrichments.

6.3.1 Example 1: Boundary Layer Solution as the Kinematic Viscosity Tends Toward Zero

6.3.1.1 Problem Statement and Reference Solutions

Consider the viscous Burgers' equation (Eq. 6.1) defined over a unit domain ($\Omega = [0, 1]$) and subject to homogeneous Dirichlet boundary conditions everywhere ($\Gamma = \Gamma_D = 0; \Gamma_N = \emptyset$). The problem formulation is as follows: For $t \in [0, 1]$, find u such that:

$$\begin{aligned} \frac{\partial u}{\partial t} + u \frac{\partial u}{\partial x} - \nu \frac{\partial^2 u}{\partial x^2} &= 0 \quad \text{on } \Omega \\ u(x, 0) &= \sin \pi x \quad \text{on } \Omega \\ u(0, t) = u(1, t) &= 0 \quad \text{on } \Gamma \end{aligned} \tag{6.13}$$

An analytical Fourier solution to Eq. 6.13 is obtainable through use of the Hopf-

Cole transformation, as detailed in [85]. The resulting analytical Fourier solution is:

$$u(x, t) = 2\pi\nu \frac{\sum_{n=1}^{\infty} a_n e^{-n^2\pi^2\nu t} n \sin n\pi x}{a_0 + \sum_{n=1}^{\infty} a_n e^{-n^2\pi^2\nu t} \cos n\pi x} \quad (6.14)$$

with Fourier coefficients, a_n :

$$\begin{aligned} a_0 &= \int_0^1 e^{-\frac{1}{2\pi\nu}(1-\cos \pi x)} dx \\ a_n &= 2 \int_0^1 e^{-\frac{1}{2\pi\nu}(1-\cos \pi x)} \cos n\pi x dx \end{aligned} \quad (6.15)$$

The integrals of Eq. 6.15 are convergent for all $\nu \neq 0$. However, for small values of ν and t , the rate of convergence of the series slows down significantly, and results in extremely difficulty computing u using this analytical expression [86]. A good discussion on this convergence issue is provided by [87] and the references within. Since this work concerns solution-tailored numerical solutions with very small viscosities, the poor accuracy of the truncated series may affect convergence rates. Thus, a 5000-element, $p = 1$ FEM solution is used as a reference instead, with the Crank-Nicolson scheme implemented with a step size of $\Delta t = \frac{1}{5000}$. For $\nu = 0$, $p = 1$ FEM is incapable of obtaining a convergent solution (recall the conservative estimate for stability $h \leq \frac{2\nu}{\max u_{IC}(x)} = 0$; or see Figs. 6.3 and 6.4). Thus, for $\nu = 0$ the analytical solution to the inviscid problem (Eq. 6.10) is used as a reference, and is found by solving for u in the implicit equation $u = u_{IC}(x - ut)$. Reference solutions for kinematic viscosities $\nu = \left\{ \frac{1}{10}, \frac{1}{50}, \frac{1}{100}, 0 \right\}$ are shown in Fig. 6.2. A

boundary layer forms near $x = 1$ with thickness decreasing as ν decreases. When $\nu = 0$, a discontinuity forms at $x = 1$, starting at time $t_b = \frac{1}{\pi}$, and persisting through later times.

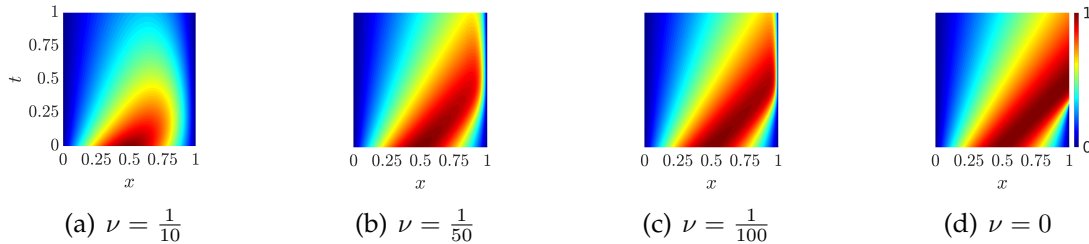


Figure 6.2: Reference solution contours (u) for the boundary layer problem over a range of kinematic viscosities (ν)

6.3.1.2 Finite Element Solutions

Problem 6.13 was initially solved over uniform grids ($h = \left\{ \frac{1}{11}, \frac{1}{23}, \frac{1}{47}, \frac{1}{95}, \frac{1}{191} \right\}$) using linear ($p = 1$) FEM. The Crank-Nicolson scheme is used for temporal discretization with a step size of $\Delta t = \frac{1}{5000}$. At each time step the Newton-Raphson method is used to iteratively solve the nonlinear set of equations. At times $t = [0, 0.25, 0.318, 0.5, 0.75, 1]$, relative L_2 and H_1 integral norms versus total degrees of freedom are shown in Figs. 6.3 and 6.4, respectively. True convergence rates are obtained and presented using the two finest grids studied ($h = \left\{ \frac{1}{95}, \frac{1}{191} \right\}$). It is observed as ν decreases, errors in the L_2 and H_1 norms increase. Specifically, a shift in the relative L_2 and H_1 norm is observed, with convergence rates remaining relatively unaffected except when $\nu = 0$. This is a result of the increasing difficulty in resolving the steep boundary layer that forms around $x = 1$. For $\nu = 0$, conver-

gence does not occur once a discontinuity arises at $t_b \geq \frac{1}{\pi}$. Spurious oscillations are visually observed in the numerical solutions for small viscosities as shown in Fig. 6.5, which displays 11-element solution contours. For relatively large kinematic viscosities ($\nu = \frac{1}{10}$) no oscillations are visually observed. However, when $\nu = \frac{1}{100}$ and $\nu = 0$, severe nonphysical oscillations arise in the 11-element solutions. With sufficient grid refinement, the boundary layer is captured for $\nu = \frac{1}{100}$, as exemplified by the 47-element solutions contours in Fig. 6.6. However grid refinement does not improve the numerical solution when $\nu = 0$.

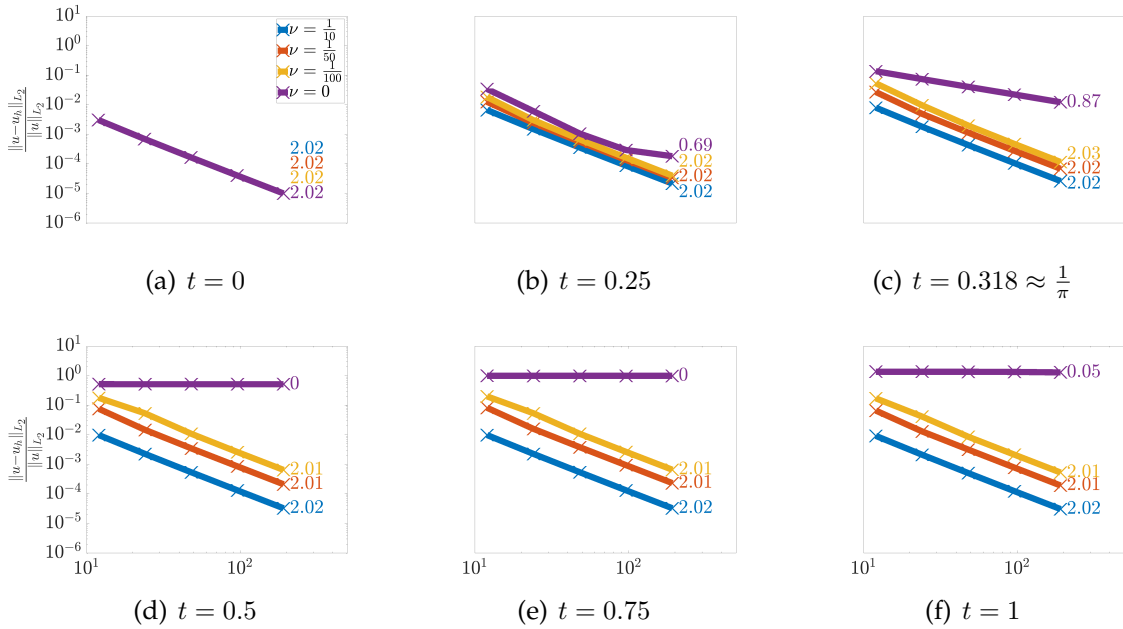


Figure 6.3: Linear ($p = 1$) FEM convergence in the relative L_2 norm $\left(\frac{\|u_h - u\|_{L_2}}{\|u\|_{L_2}}\right)$ versus total degrees of freedom (N_{DOF}) for the boundary layer problem at various times (t).

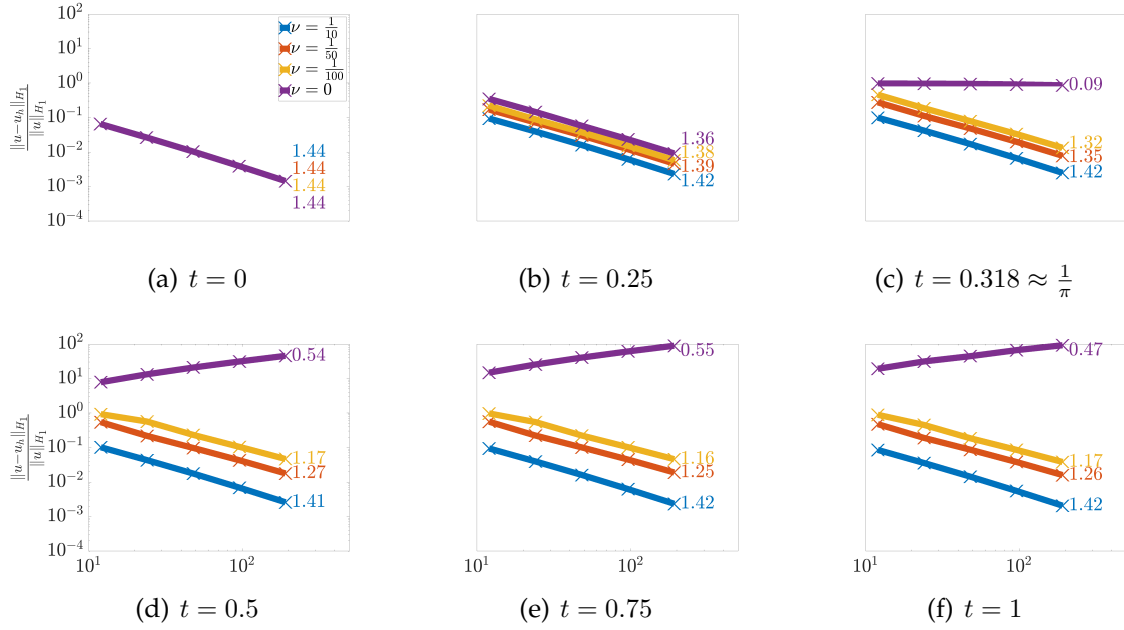


Figure 6.4: Linear ($p = 1$) FEM convergence in the relative H_1 norm $\left(\frac{\|u_h - u\|_{H_1}}{\|u\|_{H_1}}\right)$ versus total degrees of freedom (N_{DOF}) for the boundary layer problem at various times (t).

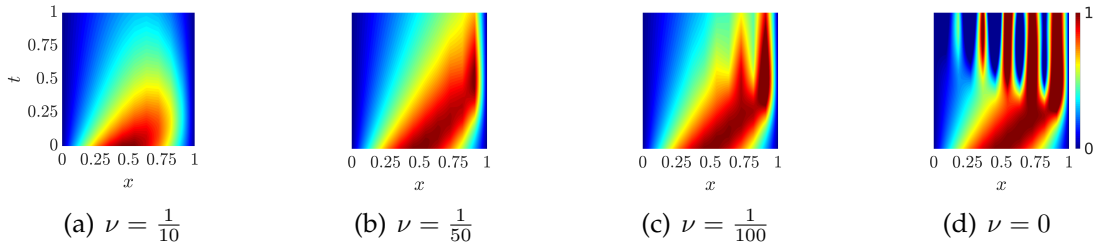


Figure 6.5: 11-element, linear ($p = 1$) FEM solution contours (u_h) for the boundary layer problem over a range of kinematic viscosities (ν).

6.3.1.3 Generalized Finite Element Solutions

For $\nu = \frac{1}{100}$, the $p = 1$ FEM solutions are improved upon using GFEM with exponential functions as enrichments. These enrichments are applied to the local domain, $\Omega_{local} = [0.8, 1]$, roughly where the boundary layer forms. Use of

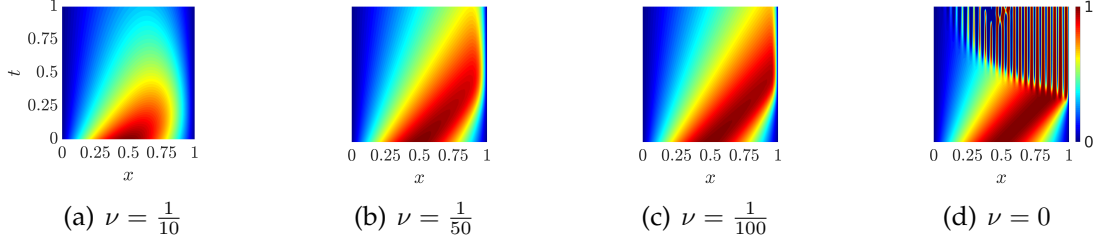


Figure 6.6: 47-element, linear ($p = 1$) FEM solution contours (u_h) for the boundary layer problem over a range of kinematic viscosities (ν).

these enrichments is motivated by findings in [88], which demonstrate exponential enrichments stabilize the GFEM solution around boundary layers arising in the advection-diffusion equation. Recall the Burgers' equation is of similar form to the advection-diffusion, except the rate of advection is replaced with the solution variable, u . Physically, the solution variable u may never exceed the maximum or minimum value provided by the initial conditions $u_{IC}(x)$. Thus, the specific exponential enrichment used for this problem is chosen to be $E_1 = e^{\frac{|\max u_{IC}(x)|x}{\nu}} = e^{100x}$. Results using these exponential enrichments are denoted as $p = 1 + \exp$. GFEM solutions. Grid sizes, temporal discretization, and nonlinear iteration are identical to those used for the $p = 1$ FEM solutions. Convergence in the relative L_2 and H_1 integral norm at various times are shown in Figs. 6.7 and 6.8, respectively. True convergence rates are obtained and presented using the two finest grids studied ($h = \left\{ \frac{1}{95}, \frac{1}{191} \right\}$). Recall no theoretical convergence rates are formally developed for GFEM using the enrichments in this example. It is observed in Figs 6.7 and 6.8 that use of the exponential enrichments results in a significant reduction of error after the boundary layer forms, and at the same number of DOFs when compared to

$p = 1$ FEM. Plots of the relative L_2 and H_1 integral norms versus time are shown in Fig. 6.9 for the 11- and 95-element GFEM solutions. The FEM and GFEM solutions have nearly identical error until $t \approx 0.25$ where boundary layer gradients become larger. The FEM solutions increase in error due to spurious oscillations, whereas the GFEM error levels remain relatively unaffected. The result is approximately 10 times reduction of error in the GFEM solutions at later time steps. Lastly, 11-element solution contours are shown in Fig. 6.10. Here, severe nonphysical oscillations in the $p = 1$ FEM solution are observed; whereas the $p = 1 + \text{exp.}$ GFEM solution successfully captures the steep boundary layer, presenting smooth solution contours at roughly the same number of degrees of freedom.

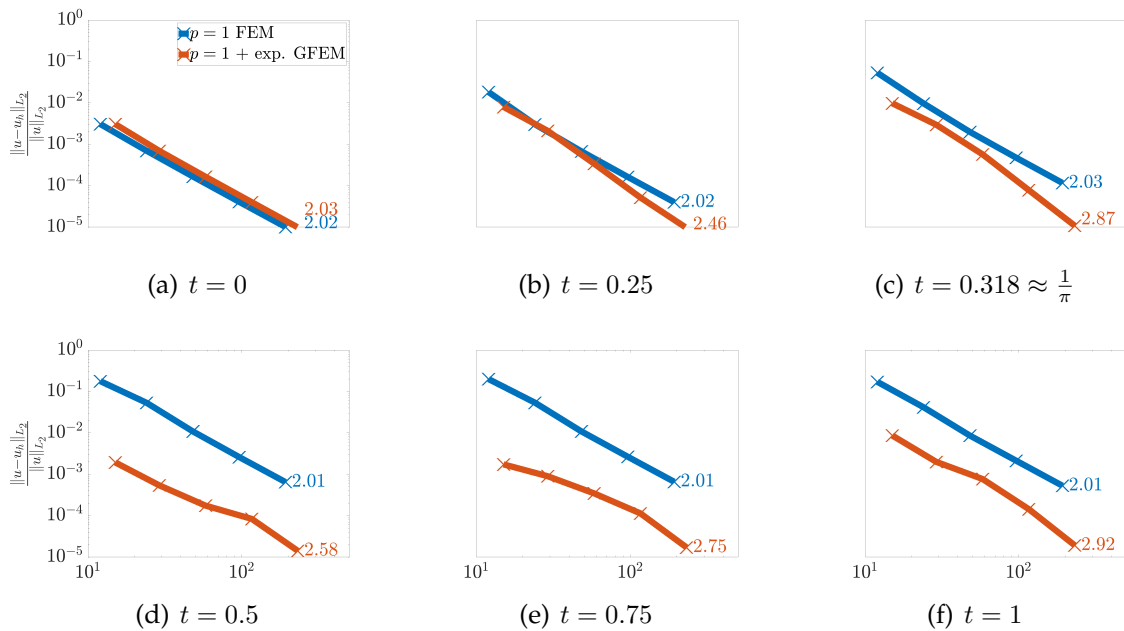


Figure 6.7: Convergence in the relative L_2 integral norm $\left(\frac{\|u_h - u\|_{L_2}}{\|u\|_{L_2}}\right)$ versus total degrees of freedom (N_{DOF}) for the boundary layer problem with kinematic viscosity $\nu = \frac{1}{100}$ using exponential enrichments.

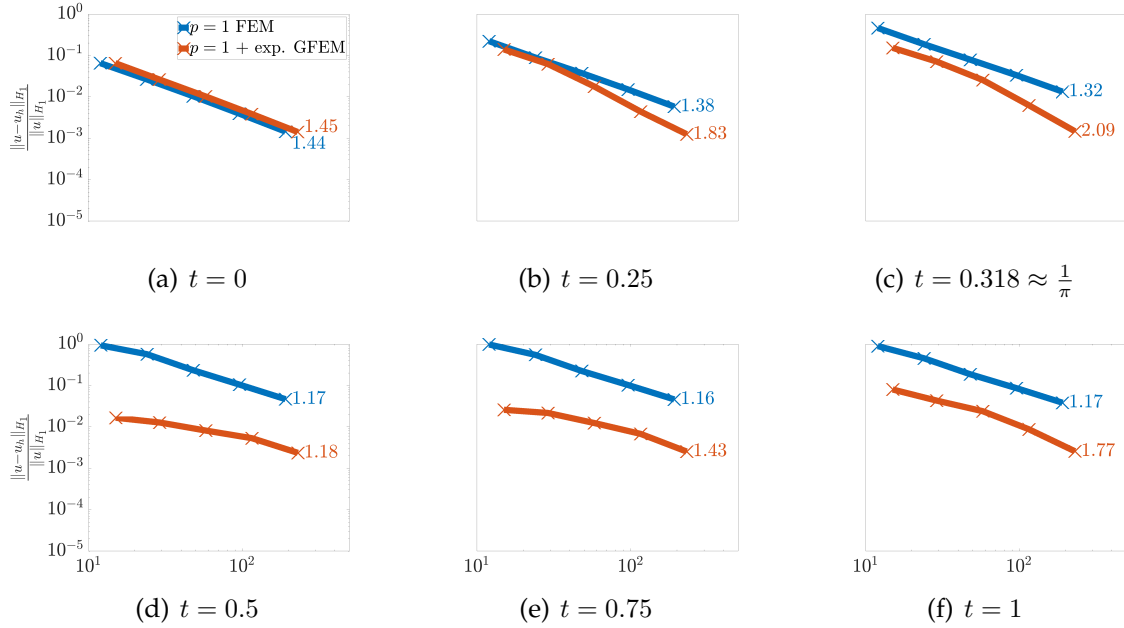


Figure 6.8: Convergence in the relative H_1 integral norm $\left(\frac{\|u_h - u\|_{H_1}}{\|u\|_{H_1}}\right)$ versus total degrees of freedom (N_{DOF}) for the boundary layer problem with kinematic viscosity $\nu = \frac{1}{100}$ using exponential enrichments.

When $\nu = 0$, the presented $p = 1$ FEM is ill-suited for two reasons: 1) enforcement of the Dirichlet boundary condition $u(1, t) = 0$ inhibits the FEM solution from capturing the discontinuity occurring at $x = 1$, and 2) increasingly steep gradients leading up to $t = \frac{1}{\pi}$ (infinitely steep at $t = \frac{1}{\pi}$) results in spurious oscillations which propagate with time. To address the first challenge, the last node in the domain at $x = 1$ is enriched with a Heaviside function which is 0 everywhere except the element containing the node. This may be thought of as a linear correction, which allows the GFEM to satisfy $u(1, t) = 0$, but also account for the discontinuity which arises. Results using the Heaviside enrichment are denoted as $p = 1 + \text{disc. GFEM}$ solutions. Convergence in the relative L_2 and H_1 integral norm at various times are

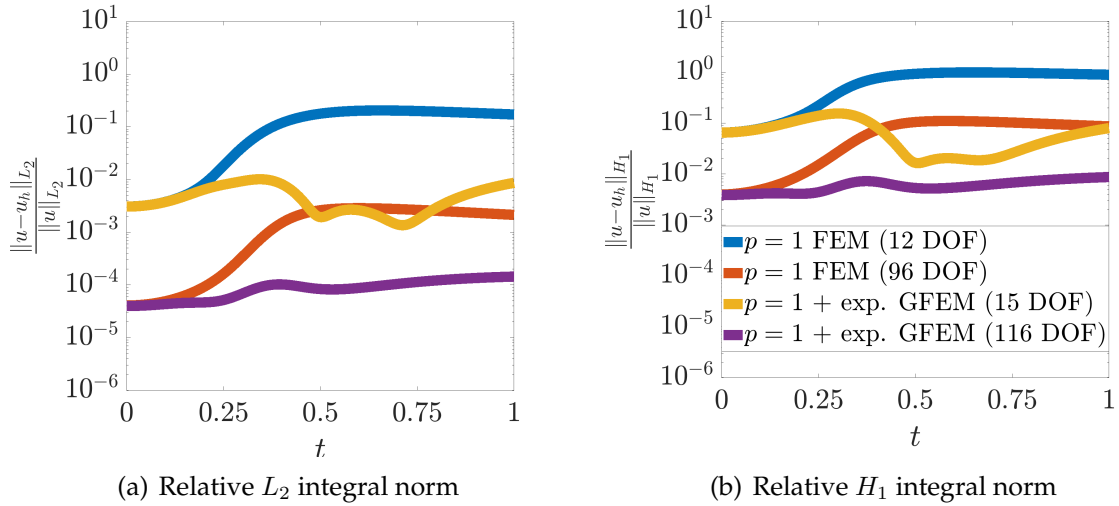


Figure 6.9: Relative L_2 $\left(\frac{\|u_h - u\|_{L_2}}{\|u\|_{L_2}}\right)$ and H_1 $\left(\frac{\|u_h - u\|_{H_1}}{\|u\|_{H_1}}\right)$ integral norms versus time (t) for 11-element and 95-element FEM and $p = 1 + \text{exp.}$ GFEM for the boundary layer problem with kinematic viscosity $\nu = \frac{1}{100}$.

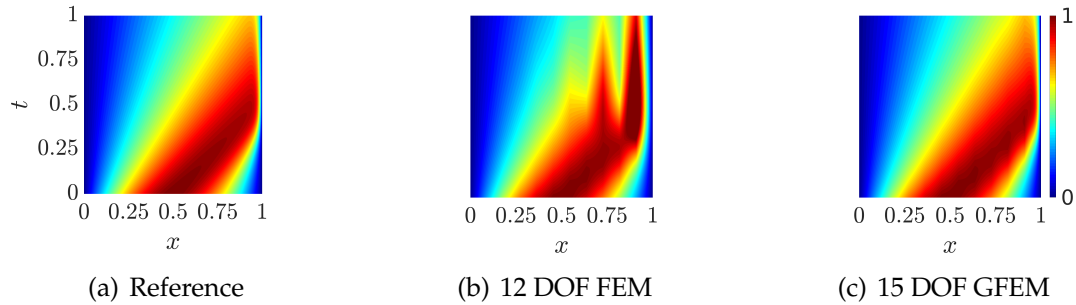


Figure 6.10: 11-element, $p = 1$ FEM (12 DOF) and $p = 1 + \text{exp.}$ GFEM (15 DOF) solution contours (u_h) compared to the reference for the boundary layer problem with $\nu = \frac{1}{100}$

shown in Figs. 6.11 and 6.12, respectively. True convergence rates are obtained and presented using the two finest grids studied ($h = \left\{ \frac{1}{95}, \frac{1}{191} \right\}$). Recall no theoretical convergence rates are formally developed for GFEM using the enrichments in this example. Here convergence in the L_2 norm is significantly improved in the GFEM solutions with respect to linear FEM, however, the GFEM using Heaviside enrich-

ment does not appear to convergence in the H_1 norm. Plots of the relative L_2 and H_1 integral norms versus time are shown in Fig. 6.13 for 11- and 95-element GFEM solutions. Similar to the $\nu = \frac{1}{100}$ results, the FEM and GFEM solutions have similar error levels until $t \approx \frac{1}{\pi}$ where boundary layer gradients become larger. Around $t \approx \frac{1}{\pi}$, both the FEM and GFEM solutions rise in error. This is explained as both the linear interpolation and Heaviside function are ill-suited for capturing the increasingly steep gradients leading up to the discontinuity at $t = \frac{1}{\pi}$. This is observed in Fig. 6.14, which provides 11-element $p = 1$ FEM and $p = 1 + \text{disc.}$ GFEM solution contours. Severe oscillations are observed in the $p = 1$ FEM solutions, whereas comparatively the GFEM solution is significantly better. However, oscillations still persist in the GFEM solutions, starting around $t = \frac{1}{\pi}$, and propagate with time. With grid refinement as shown in Fig. 6.15, which provides 47-element $p = 1$ FEM and $p = 1 + \text{disc.}$ GFEM solution contours, the FEM solution does not improve. However, while oscillations persist with the GFEM solution, they are significantly muted. These results demonstrate the importance of the intermediate, transitional solution features on stability of the GFEM solution for the Burgers' equation. Specific to this example, the infinitely steep boundary formed in the limit as $t \rightarrow \frac{1}{\pi}$ results in spurious oscillations even though the discontinuity is captured. To better explore the effect the intermediate solution features have on the stability of the GFEM, a second example is examined in which a shock forms with a known steady state solution.

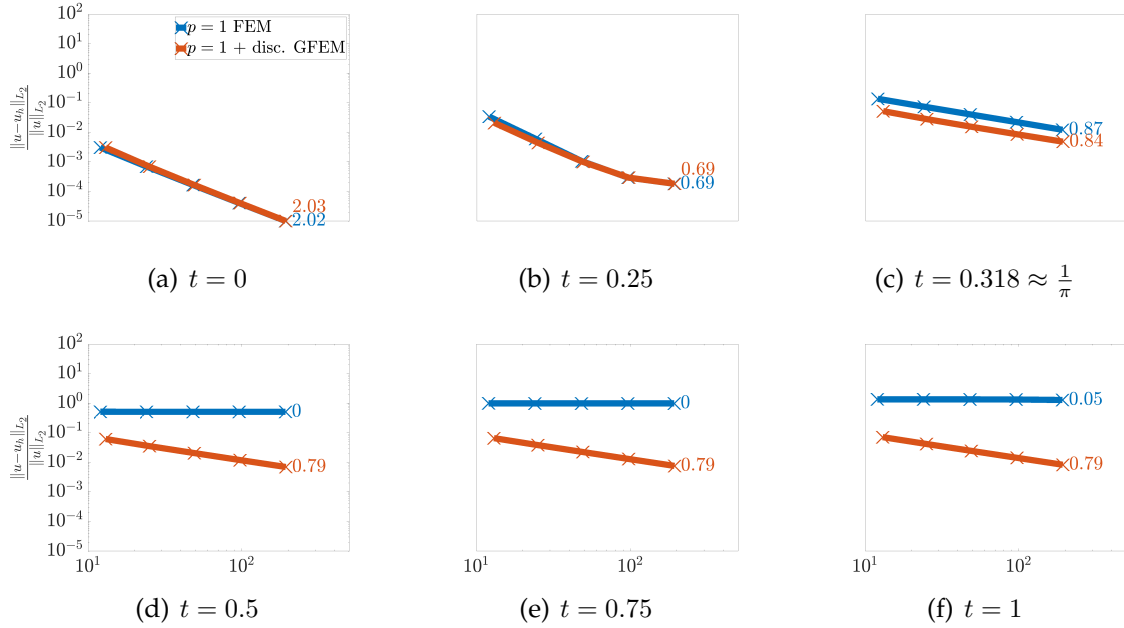


Figure 6.11: Convergence in the relative L_2 integral norm $\left(\frac{\|u_h - u\|_{L_2}}{\|u\|_{L_2}}\right)$ versus total degrees of freedom (N_{DOF}) for the boundary layer problem with $\nu = 0$ using Heaviside enrichments.

6.3.2 Example 2: Shock Formulation in the Domain

6.3.2.1 Problem Statement and Reference Solutions

Consider the viscous Burgers' equation (Eq. 6.1) defined over a unit domain ($\Omega = [0, 1]$) and subject to Dirichlet boundary conditions everywhere ($\Gamma = \Gamma_D$). The problem formulation is as follows: For $t \in [0, 1]$, find u such that:

$$\begin{aligned} \frac{\partial u}{\partial t} + u \frac{\partial u}{\partial x} - \nu \frac{\partial^2 u}{\partial x^2} &= 0 \quad \text{on } \Omega \\ u(x, 0) &= \cos \pi x \quad \text{on } \Omega \\ u(0, t) &= 1; u(1, t) = -1 \quad \text{on } \Gamma \end{aligned} \tag{6.16}$$

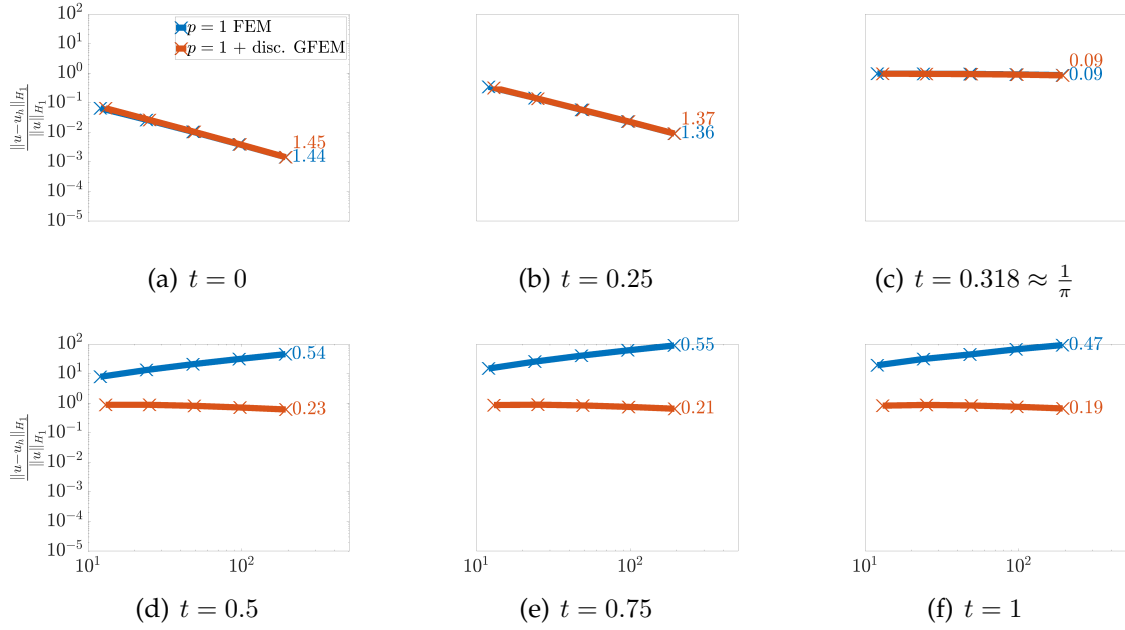


Figure 6.12: Convergence in the relative H_1 integral norm $\left(\frac{\|u_h - u\|_{H_1}}{\|u\|_{H_1}}\right)$ versus total degrees of freedom (N_{DOF}) for the boundary layer problem with $\nu = 0$ using Heaviside enrichments.

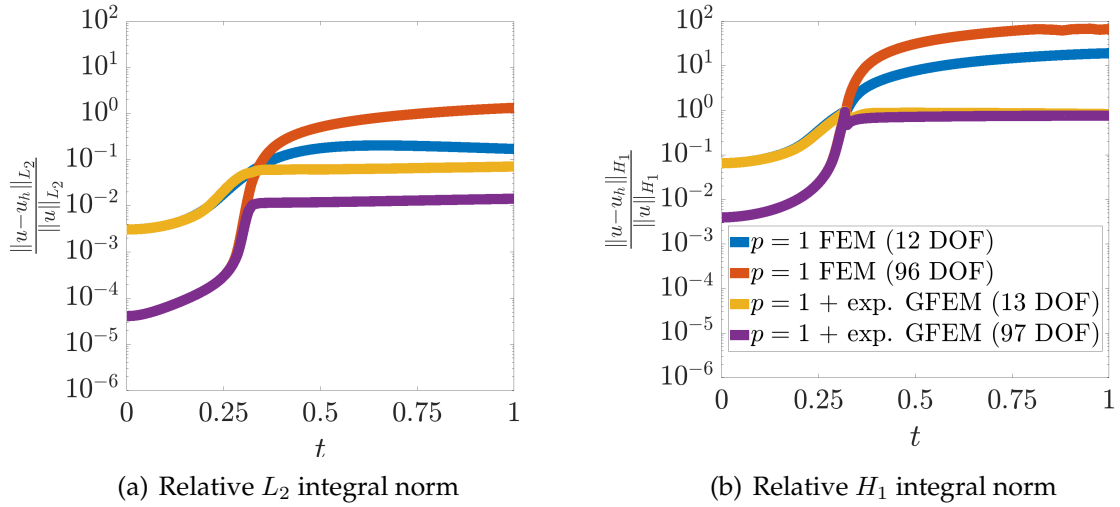


Figure 6.13: Relative L_2 $\left(\frac{\|u_h - u\|_{L_2}}{\|u\|_{L_2}}\right)$ and H_1 $\left(\frac{\|u_h - u\|_{H_1}}{\|u\|_{H_1}}\right)$ integral norms versus time (t) for 11-element and 95-element FEM and $p = 1 + \text{disc. GFEM}$ for the boundary layer problem with kinematic viscosity $\nu = 0$.

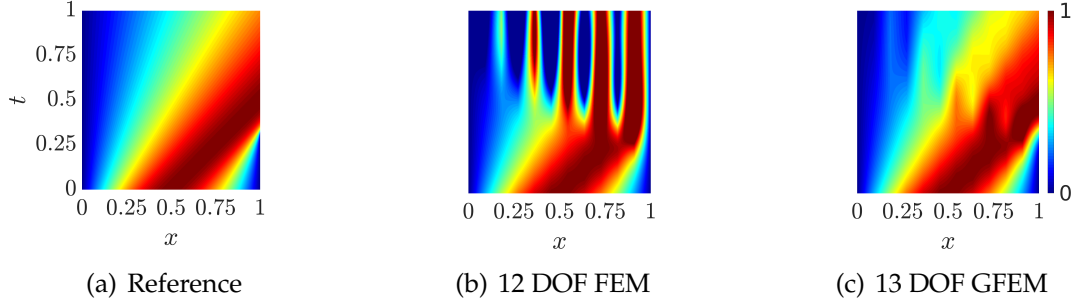


Figure 6.14: 11-element $p = 1$ FEM (12 DOF) $p = 1 + \text{disc.}$ GFEM (13 DOF) solution contours (u_h) compared to the reference for the boundary layer problem with kinematic viscosity $\nu = 0$.

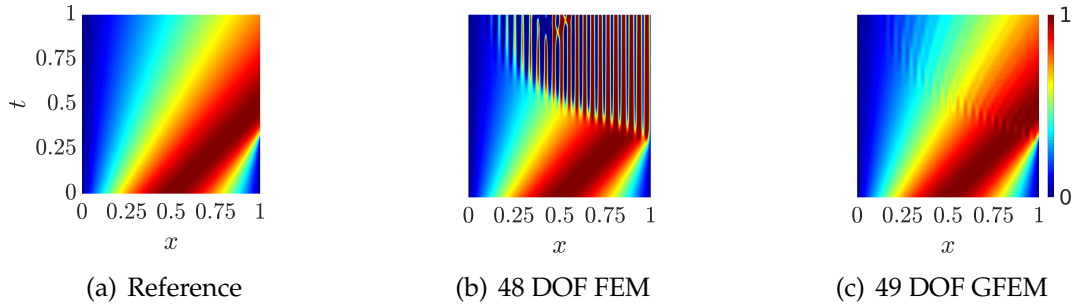


Figure 6.15: 47-element $p = 1$ FEM (48 DOF) $p = 1 + \text{disc.}$ GFEM (49 DOF) solution contours (u_h) compared to the reference for the boundary layer problem with kinematic viscosity $\nu = 0$.

An analytical solution to this problem is unknown, however a steady state solution is provided by $u_{ss} = \sqrt{2k} \tanh \left[\sqrt{\frac{k}{2\nu^2}} \left(\frac{1}{2} - x \right) \right]$, where k is a constant solvable from the nonlinear equation $\sqrt{2k} \tanh \sqrt{\frac{k}{8\nu^2}} - 1 = 0$. For sufficiently small kinematic viscosity ν , the constant $k \approx \frac{1}{2}$, simplifying the steady state solution to $u_{ss} \approx \tanh \left[\frac{1}{2\nu} \left(\frac{1}{2} - x \right) \right]$. The steady state solution represents the instance when the shock has formed entirely, with the shock thickness decreasing as ν decreases. Shock location is at $x = 0.5$. Fig. 6.16 shows 5000-element, $p = 1$ FEM reference solutions for $\nu = \left[\frac{1}{50}, \frac{1}{100}, \frac{1}{500}, \frac{1}{1000} \right]$. Note the temporal term for these references

were solved over $t = [0, 0.75]$ using the Crank-Nicolson scheme with a step size of $\Delta t = \frac{1}{5000}$.

6.3.2.2 Numerical Solutions

Problem 6.16 was initially solved over uniform grids ($h = \left[\frac{1}{11}, \frac{1}{23}, \frac{1}{47}, \frac{1}{95}, \frac{1}{191} \right]$) using $p = 1$ FEM and GFEM enriched with the steady state solution for $\nu = \left[\frac{1}{50}, \frac{1}{100}, \frac{1}{500}, \frac{1}{1000} \right]$. The local domain the steady state enrichment is applied is given by $\Omega_{local} = \left[\frac{1}{2} - 2\nu \tanh^{-1} 0.99 - h_e, \frac{1}{2} + 2\nu \tanh^{-1} 0.99 + h_e \right]$, which includes all nodes around the shock location $x = \frac{1}{2}$ where the steady state solution $|u_{ss}| \leq 0.99$. GFEM solutions using the steady state solution as an enrichment are denoted by $p = 1 + ss$ GFEM solutions. The Crank-Nicolson scheme is used for temporal discretization with a step size of $\Delta t = \frac{1}{5000}$. At each time step the Newton-Raphson method is used to iteratively solve the nonlinear set of equations.

Plots of the relative L_2 and H_1 norm versus time are shown in Figs. 6.17 and 6.18, respectively. The $p = 1$ FEM and $p = 1 + ss$ GFEM solutions return similar error levels up until $t \approx \frac{1}{\pi}$ where shock gradients increase. This is expected since the steady state solution is not closely correlated with the initial transient solution. Around $t = \frac{1}{\pi}$, error levels rise in the $p = 1$ FEM solutions, with the rise increasing as ν becomes smaller. At $t = 0.75$, 95-element $p = 1$ FEM solutions return errors in the relative L_2 are 0.10%, 0.27%, 0.86%, and 3.3% for $\nu = \left[\frac{1}{50}, \frac{1}{100}, \frac{1}{500}, \frac{1}{1000} \right]$, respectively. Similarly in the relative H_1 norm the errors are 4.4%, 10.4%, 35.0%, and 73.5%, respectively. Use of the steady state as an enrichment in

GFEM results in a significant reduction of error in both the L_2 and H_1 norm. At $t = 0.75$ the 95-element GFEM solutions enriched with the steady state solution have errors in the relative L_2 norm of 0.0027%, 0.0047%, 0.0041%, and 0.0032% for $\nu = \left[\frac{1}{50}, \frac{1}{100}, \frac{1}{500}, \frac{1}{1000} \right]$, respectively. Similarly in the relative H_1 norm the errors are 0.13%, 0.26%, 1.36%, and 2.79%, respectively. Although the $p = 1 + \text{ss}$ GFEM solutions significantly reduce relative errors with respect to $p = 1$ FEM, around $t = \frac{1}{\pi}$ errors peak to high values in both the integral norms. The peak value of the 95-element GFEM solution error in the H_1 norm for $\nu = \left[\frac{1}{50}, \frac{1}{100}, \frac{1}{500}, \frac{1}{1000} \right]$ are 0.62%, 1.3%, 12.9%, and 17.0%, respectively. These large errors arising in the GFEM solutions while the shock is forming is due to the linear interpolation and the steady state enrichment being ill-suited at capturing the intermediate solution features, similar to the results of example 1 when $\nu = 0$. Visually this is explained in Fig. 6.19 which shows 11-element $p = 1$ FEM and $p = 1 + \text{ss}$ GFEM solution contours. As expected for $p = 1$ FEM solutions, oscillations arise in the numerical solutions for small $\nu = \left[\frac{1}{100}, \frac{1}{500}, \frac{1}{1000} \right]$. For the $p = 1 + \text{ss}$ GFEM solutions, muted oscillations are observed for $\nu = \left[\frac{1}{500}, \frac{1}{1000} \right]$, which arise during the formation of the shock around $t = \frac{1}{\pi}$ and which propagate with time. With grid refinement as shown in Fig. 6.20, which provides 47-element $p = 1$ FEM and $p = 1 + \text{ss}$ GFEM solution contours, oscillations visually improve.

Convergence plots in the relative L_2 norm versus total degrees of freedom at times $t = [0, 0.25, 0.3, 0.35, 0.5, 0.75]$ for $\nu = \left[\frac{1}{50}, \frac{1}{100}, \frac{1}{500}, \frac{1}{1000} \right]$ are shown in Figs.

6.21, 6.22, 6.23, 6.24, respectively. Similarly, Figs. 6.25, 6.26, 6.27, 6.28, show convergence plots for the relative H_1 norm. Note since the steady state solution is closely correlated with the transient solution post-shock, the $p = 1 + \text{ss}$ GFEM solutions are on the same order of numerical precision as the 5000-element, $p = 1$ FEM reference solution. This is observed in the convergence plots as the $p = 1 + \text{ss}$ GFEM solution convergence begins to flatten out after around $t = \frac{1}{\pi}$. Before shock formation, both FEM and GFEM converge similarly in all norms studied. Additionally, $p = 1$ FEM performs slightly better since the steady state as an enrichment is not correlated with the initial transient solution. However, around $t = 0.25$ and persisting through $t = 0.35$, the formation of the shock results in a shift in the error, as well as sub-optimal convergence in both the FEM and GFEM solutions. After the shock has mostly formed around $t = 0.35$, error levels in the FEM solutions for the 95-element solution are larger than 30% in the H_1 norm. Error levels in the GFEM solutions at the same degrees of freedom are less than 2%. However, the effect of the oscillations which arise in the GFEM solution at earlier time steps greatly affects the convergence rate in the GFEM solution in the H_1 norm, and sub-optimal convergence is observed over all grids studied.

6.3.2.3 Capturing Intermediate Solution Features

For $\nu = \frac{1}{500}$, GFEM solutions are further improved during shock formation by enriching the domain with additional shock enrichments, $E_{\alpha j} = \tanh \left[\frac{1}{2\rho} \left(\frac{1}{2} - x \right) \right]$, where ρ controls the shock thickness. The local domain(s) these enrichments are

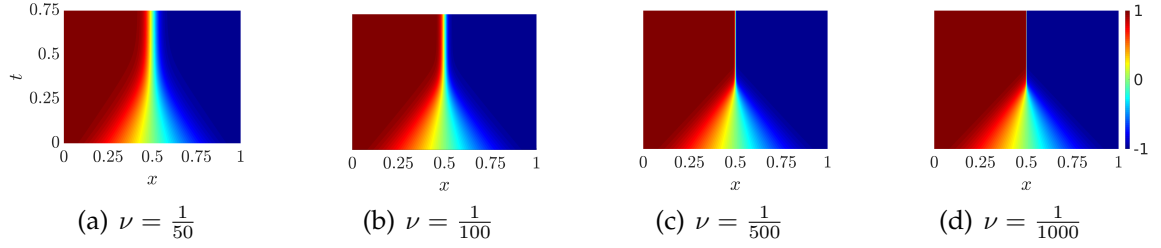


Figure 6.16: 5000-element FEM reference solutions (u) for various kinematic viscosities (ν) for the shock problem.

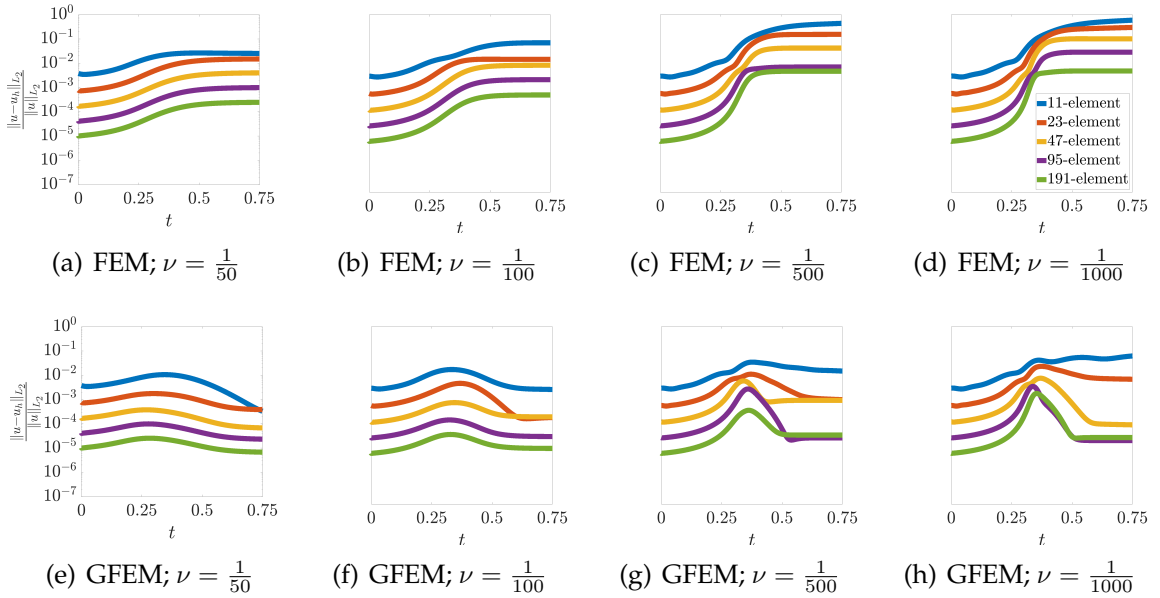


Figure 6.17: Relative L_2 norm $L_2 \left(\frac{\|u_h - u\|_{L_2}}{\|u\|_{L_2}} \right)$ versus time (t) for 11-, 23-, 47-, 95-element, and 191-element $p = 1$ FEM and $p = 1 + ss$ GFEM solutions over various kinematic viscosities (ν) for the shock problem.

applied are given by $\Omega_{local} = \left[\frac{1}{2} - 2\rho \tanh^{-1} 0.99 - h_e, \frac{1}{2} + 2\rho \tanh^{-1} 0.99 + h_e \right]$, which is the region where $|E_{\alpha j}| \leq 0.99$. Plots of the shock enrichments for various ρ are shown in Fig. 6.29. The $p = 1 + ss$ GFEM solution is further enriched using $\rho = \frac{1}{50}$, $\rho = \frac{1}{100}$, $\rho = \frac{1}{200}$, $\rho = \left[\frac{1}{50}, \frac{1}{100}, \frac{1}{200} \right]$. These solutions are presented as $p = 1 + ss + \rho = \frac{1}{50}$, $p = 1 + ss + \rho = \frac{1}{100}$, $p = 1 + ss + \rho = \frac{1}{200}$, and $p = 1 + ss + \rho =$ all GFEM solutions,

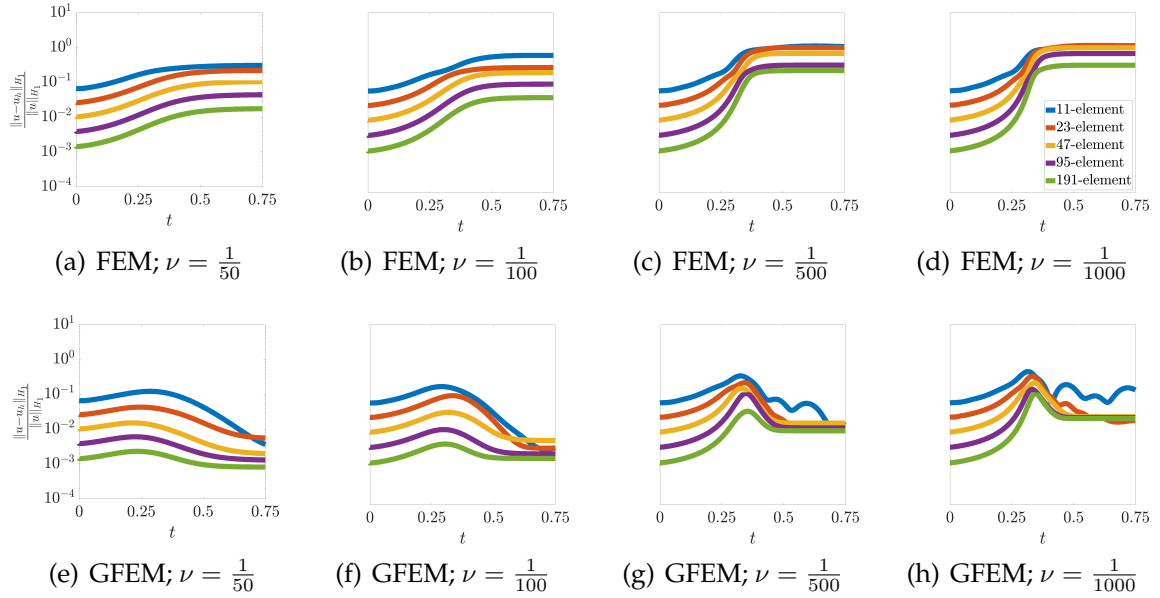


Figure 6.18: Relative H_1 norm $H_1 \left(\frac{\|u_h - u\|_{H_1}}{\|u\|_{H_1}} \right)$ versus time (t) for 11-, 23-, 47-, 95-element, and 191-element $p = 1$ FEM and $p = 1 + \text{ss}$ GFEM solutions over various kinematic viscosities (ν) for the shock problem.

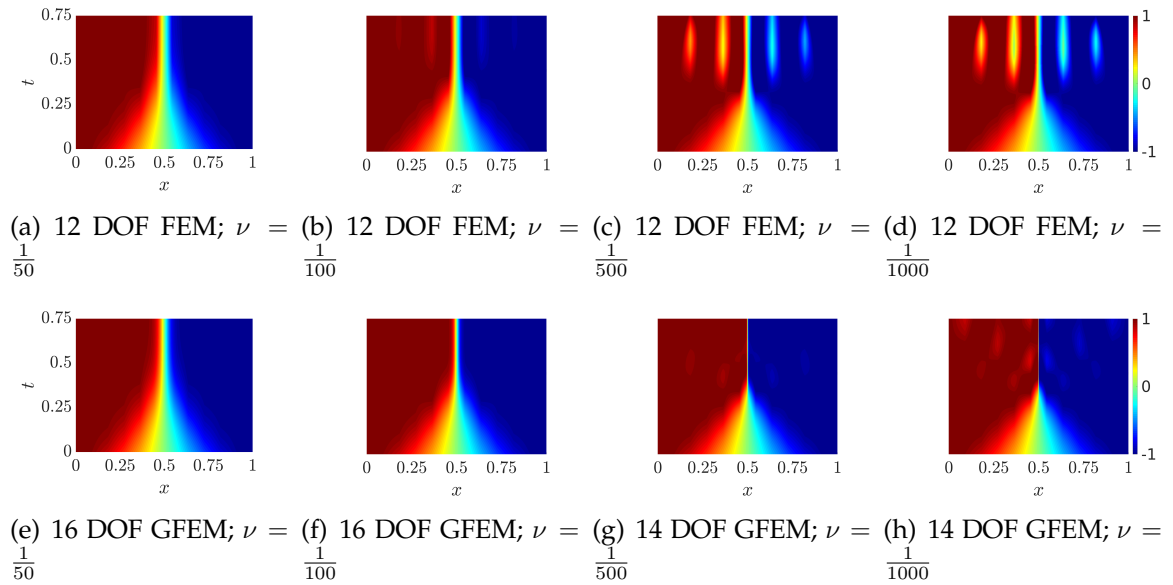


Figure 6.19: 11-element $p = 1$ FEM and $p = 1 + \text{ss}$ GFEM solution contours (u_h) over various kinematic viscosities (ν) for the shock problem.

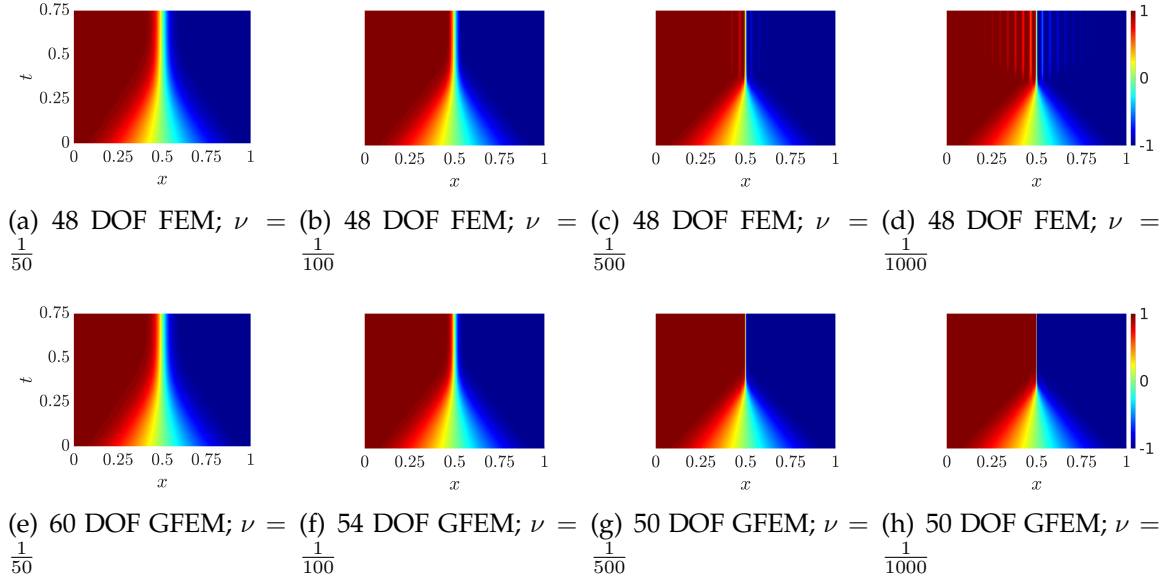


Figure 6.20: 47-element $p = 1$ FEM and $p = 1 + \text{ss}$ GFEM solution contours (u_h) over various kinematic viscosities (ν) for the shock problem.

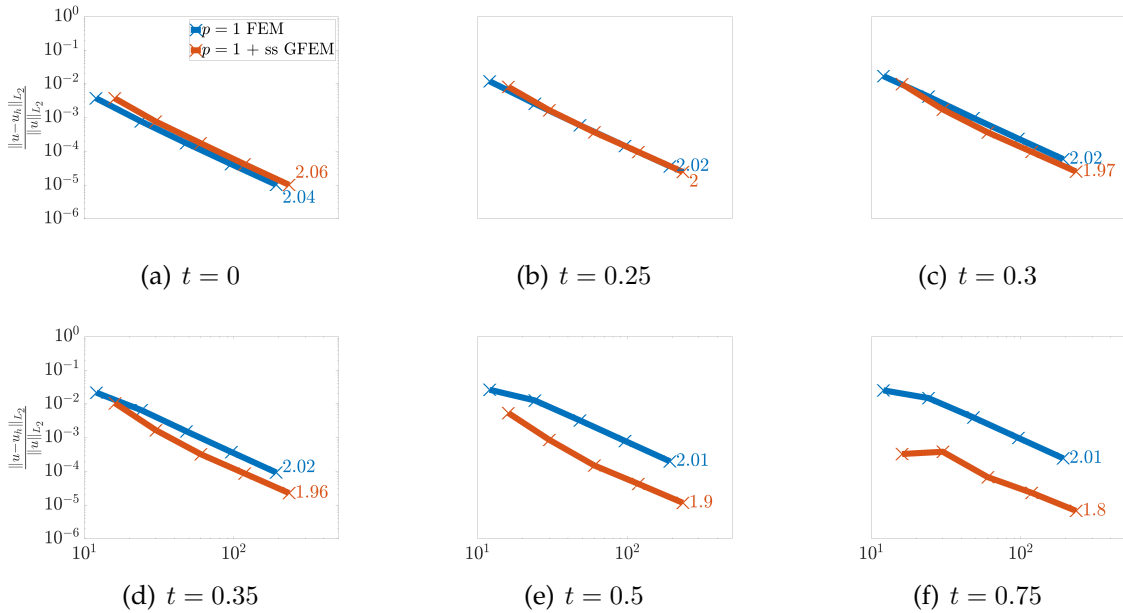


Figure 6.21: Convergence the relative L_2 integral norm $\left(\frac{\|u_h - u\|_{L_2}}{\|u\|_{L_2}}\right)$ versus total degrees of freedom (N_{DOF}) for the shock problem with kinematic viscosity $\nu = \frac{1}{50}$.

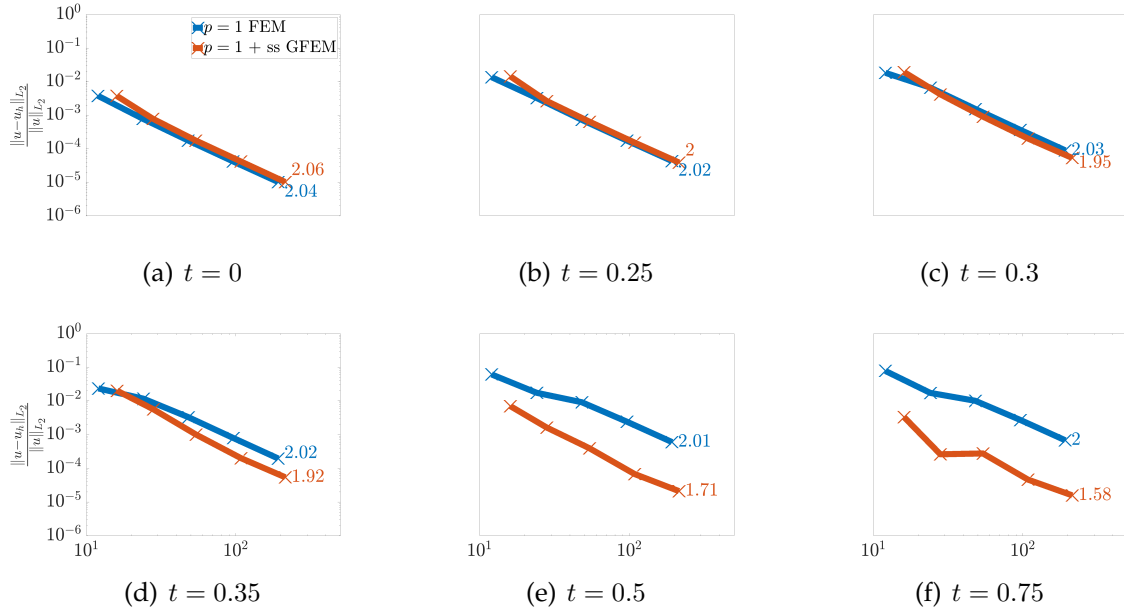


Figure 6.22: Convergence the relative L_2 integral norm $\left(\frac{\|u_h - u\|_{L_2}}{\|u\|_{L_2}}\right)$ versus total degrees of freedom (N_{DOF}) for the shock problem with kinematic viscosity $\nu = \frac{1}{100}$.

respectively. Relative L_2 and H_1 norm versus time plots are shown in Fig. 6.30 for 11-element solutions. Here the addition of various shock enrichments reduces the maximum error in the GFEM solutions, with the $p = 1 + ss + \rho = \text{all}$ GFEM providing the largest reduction of error. The maximum error in the L_2 and H_1 norm for 11-element $p = 1 + ss$ GFEM is 4% and 37.9%, respectively. For 11-element $p = 1 + ss + \rho = \text{all}$ GFEM, the maximum error in the L_2 and H_1 norm is 0.75% and 9.6%, respectively, providing a 4-5 times reduction of error. Error levels improve further with grid refinement, as shown in Fig. 6.30 for 47-element solutions. Here, the maximum error in the L_2 and H_1 norm for 47-element $p = 1 + ss$ GFEM is 0.75% and 17.1%, respectively. For 47-element $p = 1 + ss + \rho = \text{all}$ GFEM, the maximum error in the L_2 and H_1 norm is 0.031% and 1.55%, respectively, providing over a

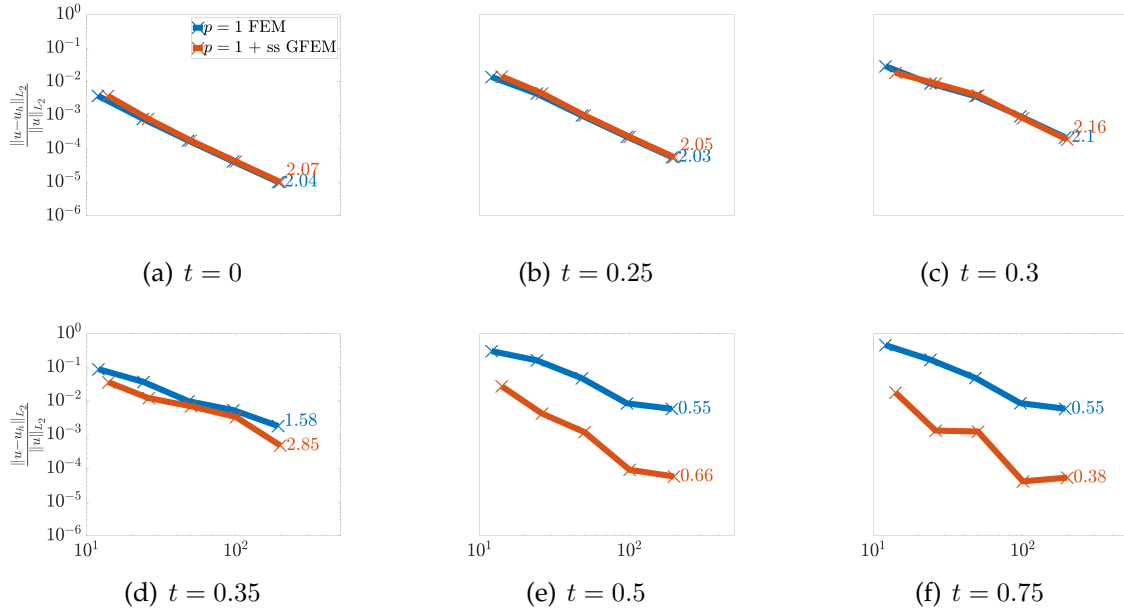


Figure 6.23: Convergence the relative L_2 integral norm $\left(\frac{\|u_h - u\|_{L_2}}{\|u\|_{L_2}}\right)$ versus total degrees of freedom (N_{DOF}) for the shock problem with kinematic viscosity $\nu = \frac{1}{500}$.

10 times reduction of error. Lastly, convergence in the L_2 and H_1 norms versus total degrees of freedom are shown in Figs. 6.32 and 6.33, respectively. Here, the addition of multiple shock enrichments improves overall convergence, specifically during shock formation between $t = 0.25$ and $t = 0.35$.

6.4 General Discussion

This chapter presents a stable, numerical solution of the one-dimensional, unsteady Burgers' equation for both a boundary layer and shock formation problem over a range of small kinematic viscosities. Compared to linear FEM, the GFEM using solution-tailored enrichments yields a significant error reduction at the same

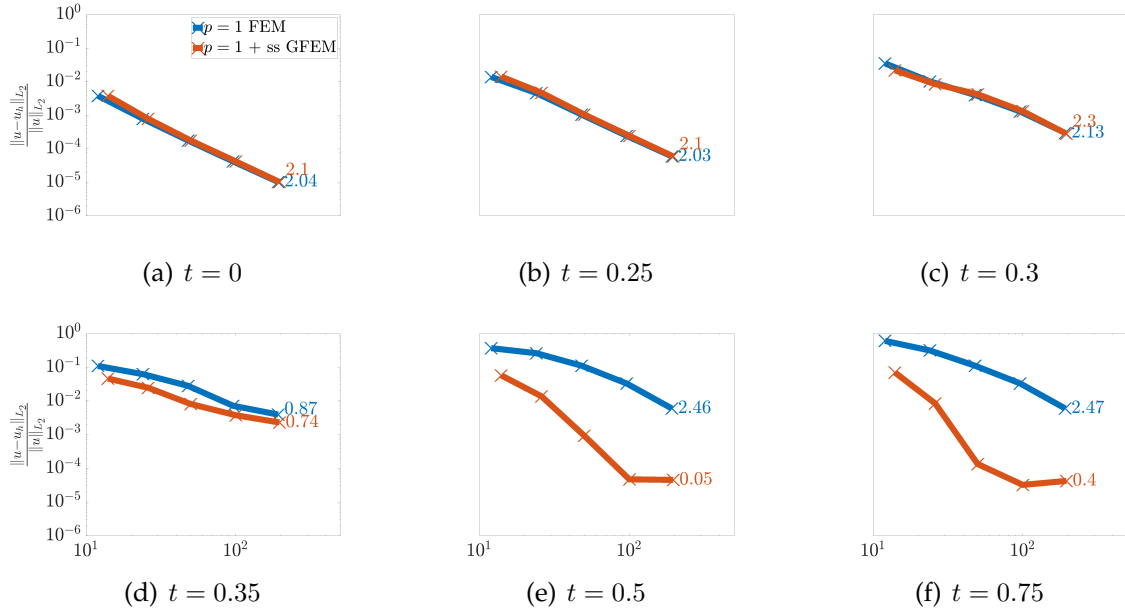


Figure 6.24: Convergence the relative L_2 integral norm $\left(\frac{\|u_h - u\|_{L_2}}{\|u\|_{L_2}}\right)$ versus total degrees of freedom (N_{DOF}) for the shock problem with kinematic viscosity $\nu = \frac{1}{1000}$.

number of degrees of freedom. For the boundary layer problem, the exponential enrichments obtained in [88] are sufficient for capturing the formation of steep boundary layers. A hyperbolic tangent function is used for the shock formation problem to capture the thin shock forming in the domain. For both examples presented, the enrichments effectively capture the local phenomena up to relatively small kinematic viscosities and reduce errors significantly regarding linear FEM in both the relative L_2 and H_1 norms. However, as the kinematic viscosity approaches extremely small values, the intermediate solution features impact the GFEM solution stability. Specifically, the boundary layer and shock formation in both examples exhibit a range of steep gradients over intermediate time scales when $\nu \ll 1$, which neither the linear interpolation nor initially presented solution-tailored en-

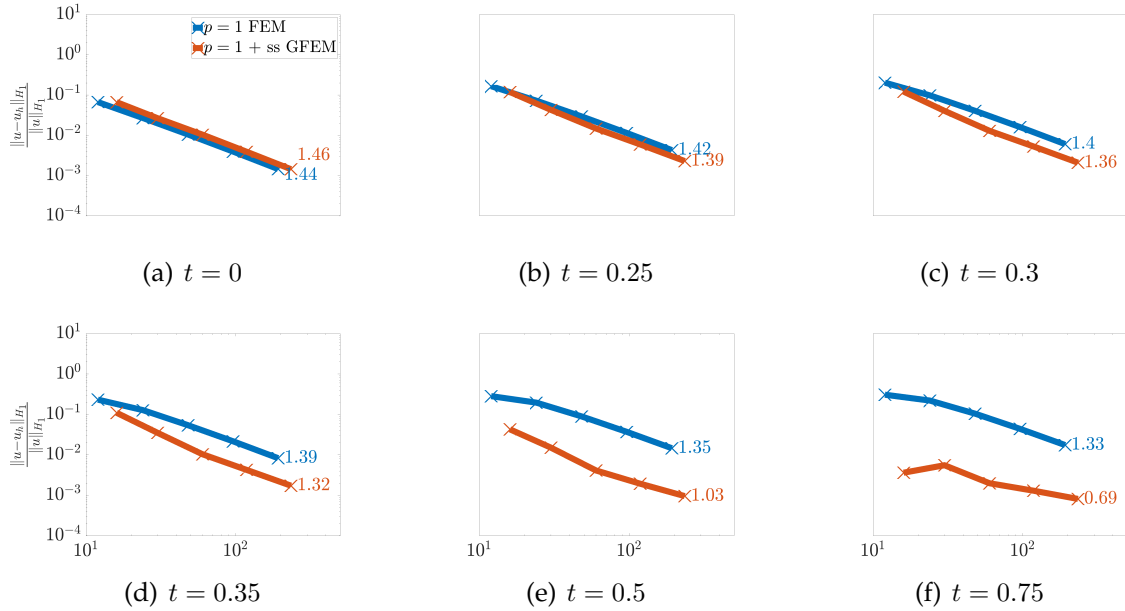


Figure 6.25: Convergence the relative H_1 integral norm $\left(\frac{\|u_h - u\|_{H_1}}{\|u\|_{H_1}}\right)$ versus total degrees of freedom (N_{DOF}) for the shock problem with kinematic viscosity $\nu = \frac{1}{50}$.

richments are sufficient at capturing. The result is spurious oscillations in the GFEM solution during the formation of the boundary layer/shock. These oscillations propagate through later time steps and affect H_1 and L_2 norm convergence. Although oscillations exist in the GFEM solutions over extremely small kinematic viscosities, the oscillations are small over coarse grids, and the errors of the GFEM solutions are still significantly reduced compared to the linear FEM. However, to further improve the shock formation problem results, a set of shock enrichments were introduced to capture the range of scales, resulting in a further reduction of error in both the L_2 and H_1 norms. Specifically, roughly greater than 100 times reduction of error is observed compared to the linear FEM at the same number of degrees of freedom. Capturing the intermediate, transitional solution features

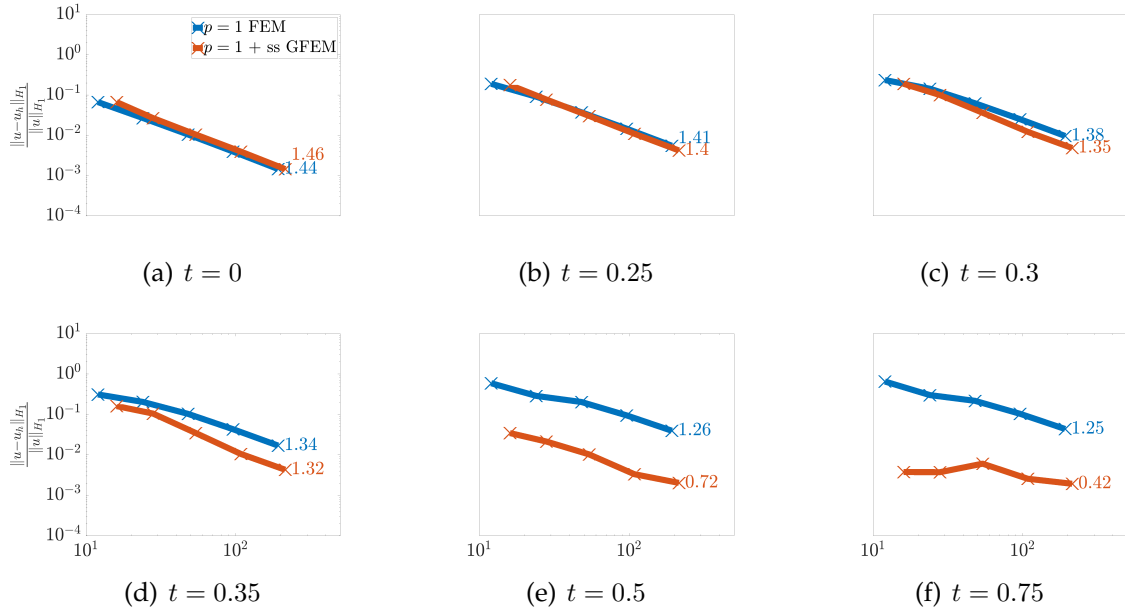


Figure 6.26: Convergence the relative H_1 integral norm $\left(\frac{\|u_h - u\|_{H_1}}{\|u\|_{H_1}}\right)$ versus total degrees of freedom (N_{DOF}) for the shock problem with kinematic viscosity $\nu = \frac{1}{100}$.

will likely be an important challenge for solving more complex flow field problems using the presented GFEM framework. Such problems may demand a set of enrichments that capture various scales of the flow as presented in the shock example or time-dependent enrichments as presented in [15].

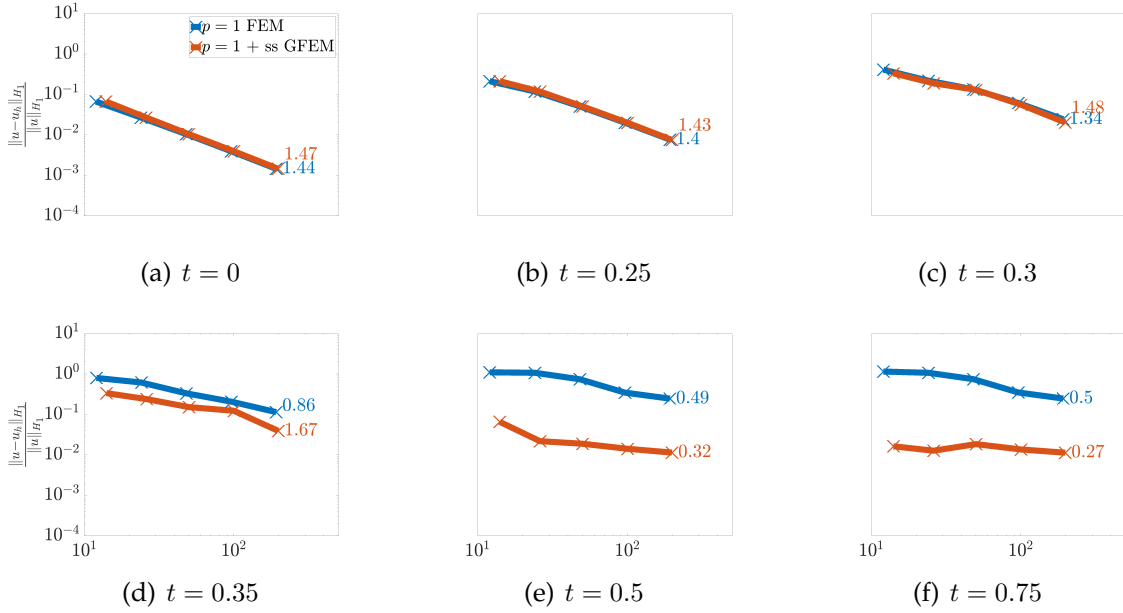


Figure 6.27: Convergence the relative H_1 integral norm $\left(\frac{\|u_h - u\|_{H_1}}{\|u\|_{H_1}}\right)$ versus total degrees of freedom (N_{DOF}) for the shock problem with kinematic viscosity $\nu = \frac{1}{500}$.

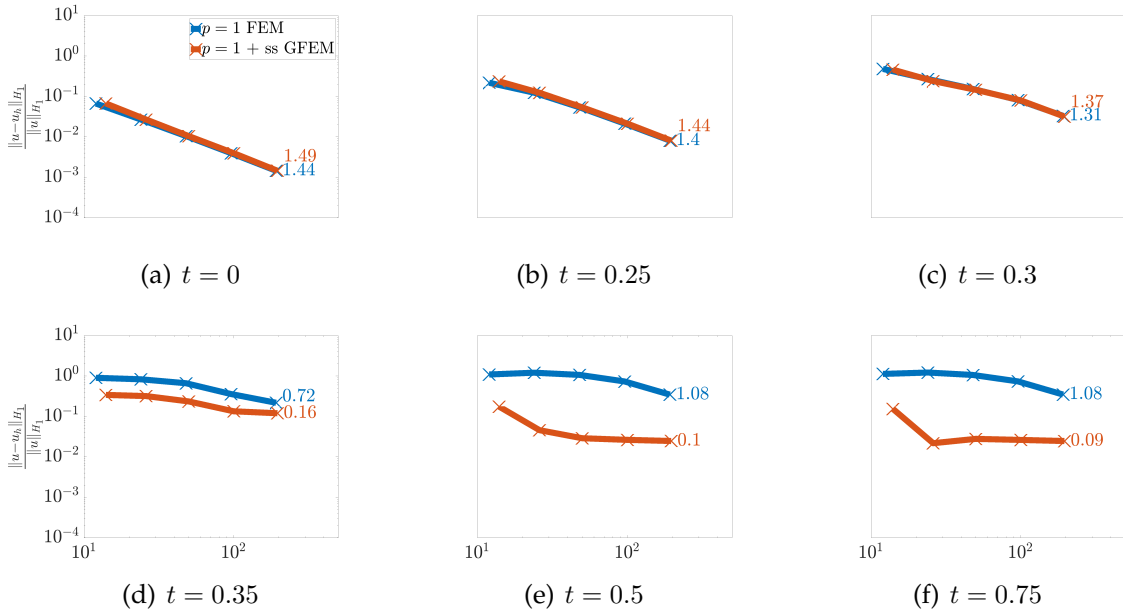


Figure 6.28: Convergence the relative H_1 integral norm $\left(\frac{\|u_h - u\|_{H_1}}{\|u\|_{H_1}}\right)$ versus total degrees of freedom (N_{DOF}) for the shock problem with kinematic viscosity $\nu = \frac{1}{1000}$.

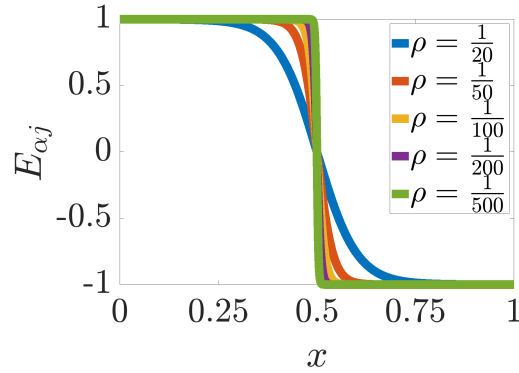


Figure 6.29: Set of shock enrichments $\left(E_{\alpha_j} = \tanh \left[\frac{1}{2\rho} \left(\frac{1}{2} - x \right) \right] \right)$ for various ρ

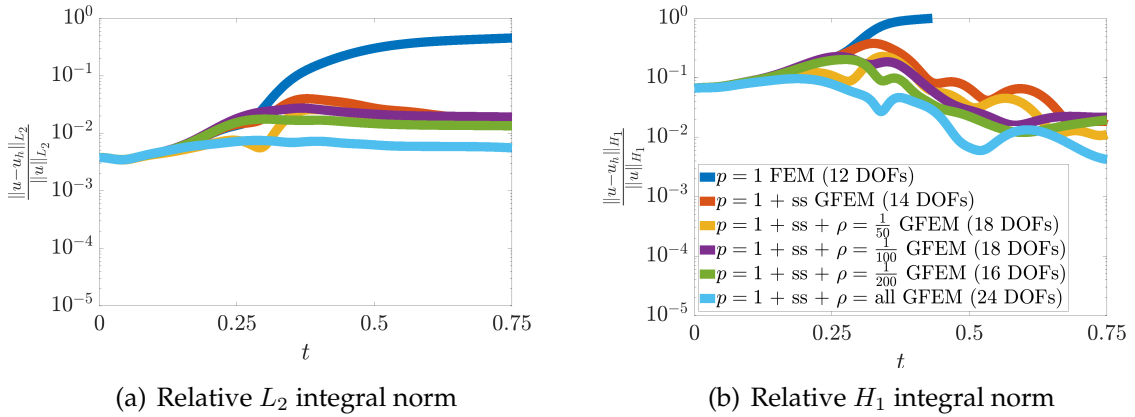


Figure 6.30: Relative $L_2 \left(\frac{\|u_h - u\|_{L_2}}{\|u\|_{L_2}} \right)$ and $H_1 \left(\frac{\|u_h - u\|_{H_1}}{\|u\|_{H_1}} \right)$ integral norms versus time (t) for 11-element FEM and GFEM solutions to the shock formation problem when kinematic viscosity $\nu = \frac{1}{500}$.

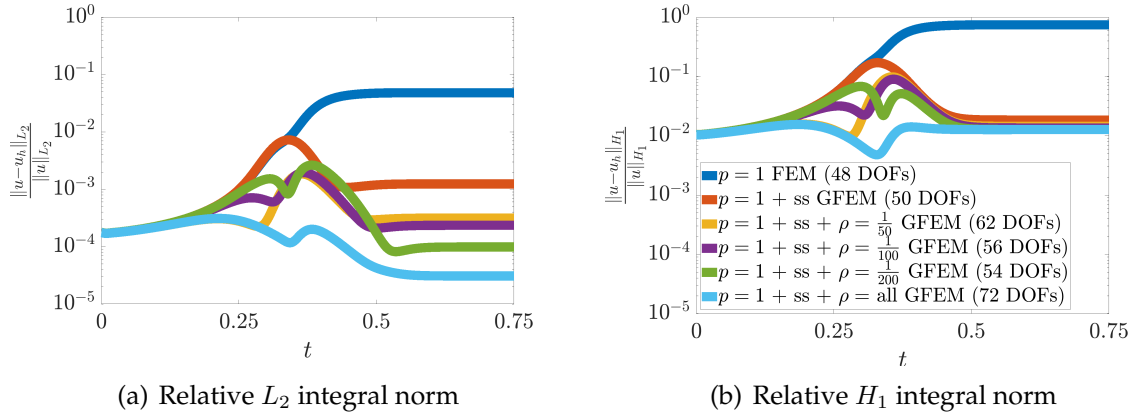


Figure 6.31: Relative L_2 $\left(\frac{\|u_h - u\|_{L_2}}{\|u\|_{L_2}}\right)$ and H_1 $\left(\frac{\|u_h - u\|_{H_1}}{\|u\|_{H_1}}\right)$ integral norms versus time (t) for 47-element FEM and GFEM solutions to the shock formation problem when kinematic viscosity $\nu = \frac{1}{500}$.

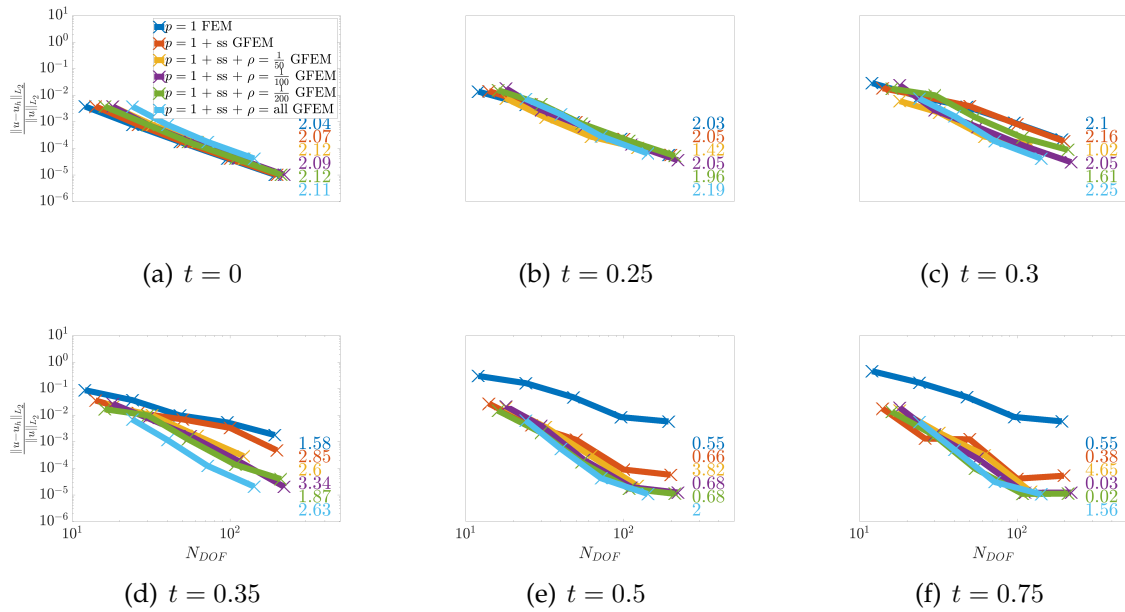


Figure 6.32: Convergence the relative L_2 integral norm $\left(\frac{\|u_h - u\|_{L_2}}{\|u\|_{L_2}}\right)$ versus total degrees of freedom (N_{DOF}) for the shock problem with kinematic viscosity $\nu = \frac{1}{500}$.

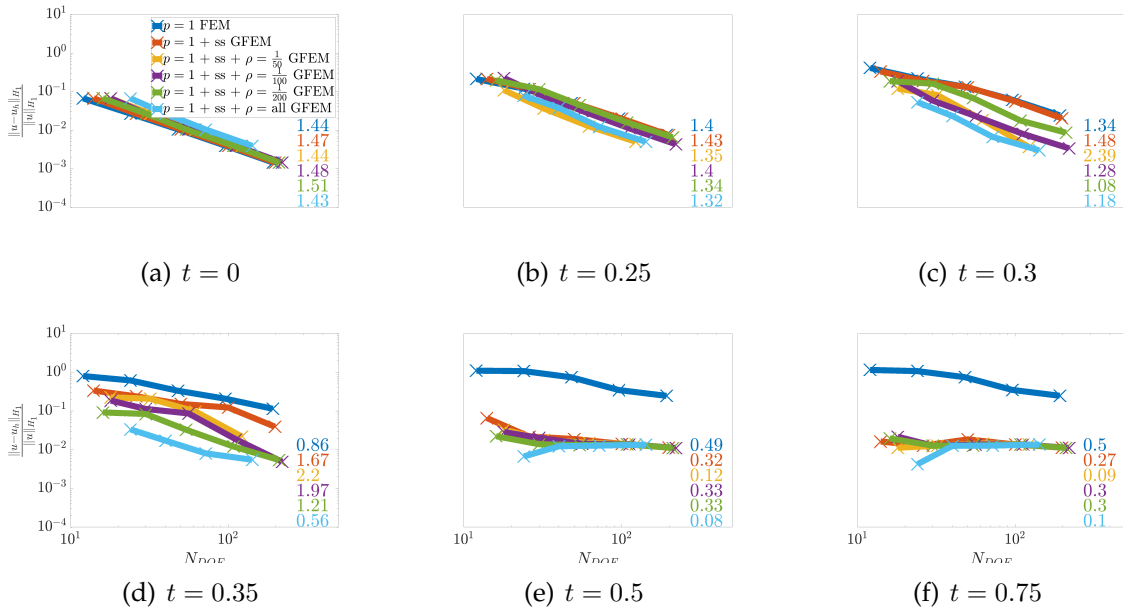


Figure 6.33: Convergence the relative H_1 integral norm $\left(\frac{\|u_h - u\|_{H_1}}{\|u\|_{H_1}}\right)$ versus total degrees of freedom (N_{DOF}) for the shock problem with kinematic viscosity $\nu = \frac{1}{500}$.

Chapter 7

Concluding Remarks

7.1 Principal Conclusions Obtained in this Study

This research aims to provide meaningful theoretical and numerical results that support and build confidence in the enriched finite element framework for high-resolution numerical solutions of fluid dynamics problems. As such, this research focuses on a deep study on the role of the enrichment process in solving fluid dynamic problems. Specifically, in this work, the enrichment process is considered for addressing the following numerical challenges incurred when solving the complete Navier-Stokes equations: (1) restrictions on allowable velocity-pressure discretization for the solution of incompressible flows, (2) non-physical, spurious oscillations that arise in numerical solutions for advection-dominated problems, and (3) capturing steep gradients due to shock waves, boundary layers, and laminar to turbulent boundary layer transition.

The complete Navier-Stokes equations simultaneously exhibit all of the above

numerical challenges and, therefore, are not ideal for providing clarity into the enrichment process. Isolation of each challenge is achievable in this work by making various simplifications to the complete Navier-Stokes equations. The first of these challenges is the focus of Chapter 3, which develops the GFEM formulation for Stokes flow, an incompressible, viscous dominated flow exempt from the latter challenges. In this chapter, the GFEM, combined with the penalty pressure method, is shown to address this challenge naturally using higher-order enrichments. Subsequently, results yield improvements in solution convergence regarding more traditional, Lagrangian finite elements.

Chapter 4 reinforces the theoretical foundation for stable, numerical solutions of linear advection-dominated problems using enriched finite elements. Insight into the enrichment process for stabilizing this class of problems is achievable using a consistent decomposition with the variational multiscale method. The enrichment process improves status-quo stabilized methods by reducing the number of assumptions necessary to achieve practical methods. No restrictions are placed on the enrichment selection process, allowing the choice of solution-tailored enrichments. This chapter provides insights into stabilizing solution-tailored enrichments based on fundamental solutions of linear differential operators. Fundamental solutions represent robust, generalizable enrichments for enriched finite elements, as they are independent of boundary conditions and volumetric forcing, albeit exist only for linear boundary value problems.

Chapter 5 puts the theory from Chapter 4 into practice for the numerical solu-

tion of several advection-diffusion examples. The solution-tailored, stabilizing enrichments used in the results are fundamental solutions, representing exponential functions for advection-diffusion equations. The exponential enrichments effectively capture upwind, boundary layer features arising in the advection-diffusion equations. The result is significant improvements for both stability and error convergence relative to more traditional approaches. Chapter 6 introduces additional complexity by providing numerical solutions to the nonlinear Burgers' equation. Similar exponential enrichments effectively represent boundary layer features in the Burgers' solutions, and hyperbolic tangent functions effectively represent shock features. However, an important observation from these results is that a sufficient representation of the full range of scales is necessary for stable numerical solutions using enriched finite elements. Specifically, capturing intermediate, transitional solution features will significantly challenge solving more complex flow field problems using enriched finite elements.

Overall, this research presents theoretical and numerical results that build confidence in enriched finite elements for the numerical solution of fluid dynamics problems. Results demonstrate significant improvements compared to more traditional finite elements for the numerical solution of the governing equations of an elastic medium, creeping flow, the advection-diffusion equation, and the Burgers' equation. This work helps lay the foundation for further research on enriched finite elements applied to fluid dynamics problems. The following section provides some suggestions for future work.

7.2 Recommendations for Future Research

This research helps lay the foundation of enriched finite elements for application to fluid dynamics problems. The methodology and problems considered in this work provide both theory and numerical results that support and build confidence in the enriched finite element framework for high-resolution numerical solutions of fluid dynamics problems. However, the numerical problems considered in this work by no means represent the full range of complexities associated with the complete incompressible and compressible Navier-Stokes equations. Thus, crucial future work is the application of enriched finite element methods to the complete Navier-Stokes equations.

In addition to the numerical solution of more complex problems, more work developing theory on stable solutions of nonlinear differential equations is necessary. Specifically, in Chapter 4, the methodology that uses a consistent decomposition of the variational multiscale method to compare GFEM to classical stabilized methods is only formally developed for linear differential operators. It may be assumed implicitly through linearization of nonlinear equations that the framework presented in Chapter 4 is applicable, but explicitly showing this stability for nonlinear problems would be beneficial.

The most significant avenue of future work likely comes from different methodologies for enrichment selection. The GFEM enrichment selection process is restriction-

free and detached from the remaining procedure. This freedom enables the use of both analytical and numerical enrichments that may be time-independent or time-dependent. For example, in this work, solution-tailored enrichments are obtained based on fundamental solutions of linear differential operators and known steady-state solutions; Deshmukh et al. in [27] apply data-derived, spatially localized enrichments to reconstructing 3D flow past a cylinder and a 2D flow inside a lid-driven cavity. A popular approach for the solution to solid mechanics problems is using global-local enrichments [71], where the enrichment basis is computed numerically, on-the-fly, using two-way communication between a coarse, global discretization and a potentially highly-adapted local boundary value problem defined in regions of localized interest.

Lastly, the versatility of the GFEM enrichment selection process also offers potential solutions in the field of model order reduction (MOR) and scientific machine learning (SciML). MOR and SciML make use of available data from experiments, numerical simulations, or analytical solutions to find patterns, signals, or structures that enhance predictions compared to more traditional scientific computing methods [18]. Traditional modal decomposition techniques such as proper orthogonal decomposition (POD) [19], balanced POD [20], dynamic mode decomposition (DMD) [21], global stability methods [22], and sparse coding based decomposition [23, 24] share commonality in that representation of their solutions use “global” basis vectors spanning the entire computational domain. Such methods are often inefficient for achieving dimensionality reductions for fields with high variance

[25]. Essentially, global bases often fail to take advantage of redundant features which exist locally. The GFEM framework offers the potential to spatially localize and learn redundant features, resulting in a more effective, “simpler” basis for representations of high variance fields. In SciML, an ongoing research focus is developing techniques which *complement* traditional domain models, such as hybrid methods, which combines both machine learning techniques with first principle models [26]. The GFEM offers a direct link between the governing equations and available data through the enrichment process.

Bibliography

- [1] Bisek, N. J., *High-Order Implicit Large-Eddy Simulations of Supersonic Corner Flow*.
- [2] Miller, B. A. and McNamara, J. J., "Loosely Coupled Time-Marching of Fluid-Thermal-Structural Interactions with Time-Accurate CFD," .
- [3] Zhao, S., "On the spurious solutions in the high-order finite difference methods for eigenvalue problems," *Computer Methods in Applied Mechanics and Engineering*, Vol. 196, No. 49, 2007, pp. 5031–5046.
- [4] Tran, S., Cummings, R., and Sahni, O., "Finite element based large eddy simulation of flow over bluff bodies," *Computers & Fluids*, Vol. 158, 2017, pp. 221–235, Large-eddy and direct numerical simulations of oceanic and atmospheric flows.
- [5] Brooks, A. N. and Hughes, T. J., "Streamline upwind/Petrov-Galerkin formulations for convection dominated flows with particular emphasis on the incompressible Navier-Stokes equations," *Computer Methods in Applied Mechanics and Engineering*, Vol. 32, No. 1, 1982, pp. 199–259.
- [6] Babuška, I., Caloz, G., and Osborn, J. E., "Special Finite Element Methods for a Class of Second Order Elliptic Problems with Rough Coefficients," *SIAM Journal on Numerical Analysis*, Vol. 31, No. 4, 1994, pp. 945–981.
- [7] Melenk, J., *On generalized finite element methods*, Ph.D. thesis, University of Maryland, 1995.
- [8] Melenk, J. and Babuška, I., "The partition of unity finite element method: Basic theory and applications," *Computer Methods in Applied Mechanics and Engineering*, Vol. 139, No. 1, 1996, pp. 289–314.
- [9] Duarte, C., *The hp Cloud Method*, Ph.D. thesis, The University of Texas, 1996.

- [10] Duarte, C. A. and Oden, J. T., "H-p clouds—an h-p meshless method," *Numerical Methods for Partial Differential Equations*, Vol. 12, No. 6, 1996, pp. 673–705.
- [11] Duarte, C. and Oden, J., "An h-p adaptive method using clouds," *Computer Methods in Applied Mechanics and Engineering*, Vol. 139, No. 1, 1996, pp. 237–262.
- [12] Belytschko, T. and Black, T., "Elastic crack growth in finite elements with minimal remeshing," *International Journal for Numerical Methods in Engineering*, Vol. 45, No. 5, 1999, pp. 601–620.
- [13] Belytschko, T., Gracie, R., and Ventura, G., "A Review of Extended/Generalized Finite Element Methods for Material Modelling," *Modelling and Simulation in Materials Science and Engineering*, Vol. 17, 04 2009, pp. 043001.
- [14] Oden, J., Duarte, C., and Zienkiewicz, O., "A new cloud-based hp finite element method," *Computer Methods in Applied Mechanics and Engineering*, Vol. 153, No. 1, 1998, pp. 117–126.
- [15] O'Hara, P., Duarte, C., and Eason, T., "Transient analysis of sharp thermal gradients using coarse finite element meshes," *Computer Methods in Applied Mechanics and Engineering*, Vol. 200, No. 5, 2011, pp. 812–829.
- [16] Moës, N., Dolbow, J., and Belytschko, T., "A finite element method for crack growth without remeshing," *International Journal for Numerical Methods in Engineering*, Vol. 46, No. 1, 1999, pp. 131–150.
- [17] Pereira, J. P., Duarte, C. A., Guoy, D., and Jiao, X., "hp-Generalized FEM and crack surface representation for non-planar 3-D cracks," *International Journal for Numerical Methods in Engineering*, Vol. 77, No. 5, 2009, pp. 601–633.
- [18] Baker, N., Alexander, F., Bremer, T., Hagberg, A., Kevrekidis, Y., Najm, H., Parashar, M., Patra, A., Sethian, J., Wild, S., Willcox, K., and Lee, S., "Workshop Report on Basic Research Needs for Scientific Machine Learning: Core Technologies for Artificial Intelligence," .
- [19] SIROVICH, L., "TURBULENCE AND THE DYNAMICS OF COHERENT STRUCTURES PART I: COHERENT STRUCTURES," *Quarterly of Applied Mathematics*, Vol. 45, No. 3, 1987, pp. 561–571.
- [20] Ilak, M. and Rowley, C. W., "Modeling of transitional channel flow using balanced proper orthogonal decomposition," *Physics of Fluids*, Vol. 20, No. 3, 2008, pp. 034103.
- [21] SCHMID, P. J., "Dynamic mode decomposition of numerical and experimental data," *Journal of Fluid Mechanics*, Vol. 656, 2010, pp. 5–28.

- [22] Noack, B. R. and Eckelmann, H., "A global stability analysis of the steady and periodic cylinder wake," *Journal of Fluid Mechanics*, Vol. 270, 1994, pp. 297–330.
- [23] Lee, H., Battle, A., Raina, R., and Ng, A. Y., "Efficient Sparse Coding Algorithms," *Proceedings of the 19th International Conference on Neural Information Processing Systems, NIPS'06*, MIT Press, Cambridge, MA, USA, 2006, p. 801–808.
- [24] Deshmukh, R., McNamara, J. J., Liang, Z., Kolter, J. Z., and Gogulapati, A., "Model order reduction using sparse coding exemplified for the lid-driven cavity," *Journal of Fluid Mechanics*, Vol. 808, 2016, pp. 189–223.
- [25] Mojjani, R. and Balajewicz, M., "Lagrangian basis method for dimensionality reduction of convection dominated nonlinear flows," *arXiv: Fluid Dynamics*, 2017.
- [26] Brunton, S. L., Noack, B. R., and Koumoutsakos, P., "Machine Learning for Fluid Mechanics," *Annual Review of Fluid Mechanics*, Vol. 52, No. 1, 2020, pp. 477–508.
- [27] Deshmukh, R., Shilt, T., and McNamara, J. J., "Efficient representation of turbulent flows using data-enriched finite elements," *International Journal for Numerical Methods in Engineering*, Vol. 121, No. 15, 2020, pp. 3397–3416.
- [28] Franca, L. P. and Hughes, T. J., "Two classes of mixed finite element methods," *Computer Methods in Applied Mechanics and Engineering*, Vol. 69, No. 1, 1988, pp. 89–129.
- [29] Brezzi, F. and Fortin, M., *Mixed and Hybrid Finite Element Methods*, Springer-Verlag, New York, NY, 1991.
- [30] Ladyzhenskaya, O. A. and Salkow, H., *The mathematical theory of viscous incompressible flow*, New York: Gordon and Breach, 1969.
- [31] Babuska, I., "Error-bounds for finite element method," *Numerische Mathematik*, Vol. 16, No. 4, Jan 1971, pp. 322–333.
- [32] Brezzi, F., "On the existence, uniqueness and approximation of saddle-point problems arising from lagrangian multipliers," *ESAIM: Mathematical Modelling and Numerical Analysis - Modélisation Mathématique et Analyse Numérique*, Vol. 8, No. R2, 1974, pp. 129–151.
- [33] Legrain, G., Moës, N., and Huerta, A., "Stability of incompressible formulations enriched with X-FEM," *Computer Methods in Applied Mechanics and Engineering*, Vol. 197, No. 21, 2008, pp. 1835–1849.

- [34] Srinivasan, K., Matous, K., and Geubelle, P., "Generalized finite element method for modeling nearly incompressible bimaterial hyperelastic solids," *Computer Methods in Applied Mechanics and Engineering - COMPUT METHOD APPL MECH ENG*, Vol. 197, 09 2008.
- [35] Hughes, T. J., Franca, L. P., and Balestra, M., "A new finite element formulation for computational fluid dynamics: V. Circumventing the babuska-brezzi condition: a stable Petrov-Galerkin formulation of the stokes problem accommodating equal-order interpolations," *Computer Methods in Applied Mechanics and Engineering*, Vol. 59, No. 1, 1986, pp. 85–99.
- [36] Hughes, T. J., Franca, L. P., and Hulbert, G. M., "A new finite element formulation for computational fluid dynamics: VIII. The galerkin/least-squares method for advective-diffusive equations," *Computer Methods in Applied Mechanics and Engineering*, Vol. 73, No. 2, 1989, pp. 173–189.
- [37] Baiocchi, C., Brezzi, F., and Franca, L. P., "Virtual bubbles and Galerkin-least-squares type methods (Ga.L.S.)," *Computer Methods in Applied Mechanics and Engineering*, Vol. 105, No. 1, 1993, pp. 125–141.
- [38] Hughes, T. J., "Multiscale phenomena: Green's functions, the Dirichlet-to-Neumann formulation, subgrid scale models, bubbles and the origins of stabilized methods," *Computer Methods in Applied Mechanics and Engineering*, Vol. 127, No. 1, 1995, pp. 387–401.
- [39] Ye, X. and Hall, C. A., "A discrete divergence-free basis for finite element methods," *Numerical Algorithms*, Vol. 16, No. 3, Mar 1997, pp. 365–380.
- [40] du Toit, C., "Finite element solution of the Navier-Stokes equations for incompressible flow using a segregated algorithm," *Computer Methods in Applied Mechanics and Engineering*, Vol. 151, No. 1, 1998, pp. 131–141, Containing papers presented at the Symposium on Advances in Computational Mechanics.
- [41] Hughes, T. J., Liu, W. K., and Brooks, A., "Finite element analysis of incompressible viscous flows by the penalty function formulation," *Journal of Computational Physics*, Vol. 30, No. 1, 1979, pp. 1–60.
- [42] Babuska, I. and Suri, M., "On Locking and Robustness in the Finite Element Method," *Siam Journal on Numerical Analysis - SIAM J NUMER ANAL*, Vol. 29, 10 1992.
- [43] Seabra Mariana R. R., Cesar de Sa Jose M. A., Šušтариč Primož, and Rodič Tomaž, "Some numerical issues on the use of XFEM for ductile fracture," *Computational Mechanics*, Vol. 50, No. 5, 2012, pp. 611–629.

- [44] Zienkiewicz, O., Taylor, R., and Zhu, J., *The Finite Element Method: Its Basis and Fundamentals*, Elsevier Science, 2005.
- [45] Simo, J. and Hughes, T., *Computational Inelasticity*, Springer-Verlag New York, 1998.
- [46] Herrmann, L. R., "Elasticity equations for incompressible and nearly incompressible materials by a variational theorem." *AIAA Journal*, Vol. 3, No. 10, 1965, pp. 1896–1900.
- [47] Elman, H., Silvester, D. J., and Wathen, A. J., *Finite Elements and Fast Iterative Solvers : with Applications in Incompressible Fluid Dynamics*, Oxford University Press, 2005 2005.
- [48] Franca, L. P. and Carmo, E. G. D. D., "The Galerkin gradient least-squares method," *Computer Methods in Applied Mechanics and Engineering*, Vol. 74, No. 1, 1989, pp. 41–54.
- [49] Franca, L. and Russo, A., "Deriving upwinding, mass lumping and selective reduced integration by residual-free bubbles," *Applied Mathematics Letters*, Vol. 9, No. 5, 1996, pp. 83–88.
- [50] Brezzi, F., Franca, L., Hughes, T., and Russo, A., "b = g," *Computer Methods in Applied Mechanics and Engineering*, Vol. 145, No. 3, 1997, pp. 329–339.
- [51] Hughes, T. J. R., Scovazzi, G., and Franca, L. P., *Multiscale and Stabilized Methods*, In *Encyclopedia of Computational Mechanics Second Edition*, 2017, p. 1–64.
- [52] Turner, D. Z., Nakshatrala, K. B., and Hjelmstad, K. D., "A stabilized formulation for the advection–diffusion equation using the Generalized Finite Element Method," *International Journal for Numerical Methods in Fluids*, Vol. 66, No. 1, 2011, pp. 64–81.
- [53] Brenner, S. and Scott, R., *The Mathematical Theory of Finite Element Methods*, Springer-Verlag New York, 2008.
- [54] Reddy, B., *Introductory Functional Analysis*, Springer-Verlag New York, 1998.
- [55] Gupta, V., Duarte, C., Babuska, I., and Banerjee, U., "A stable and optimally convergent generalized FEM (SGFEM) for linear elastic fracture mechanics," *Computer Methods in Applied Mechanics and Engineering*, Vol. 266, 2013, pp. 23–39.
- [56] Duarte, C., Babuska, I., and Oden, J., "Generalized finite element methods for three-dimensional structural mechanics problems," *Computers & Structures*, Vol. 77, No. 2, 2000, pp. 215–232.

- [57] Hughes, T., *The Finite Element Method: Linear Static and Dynamic Finite Element Analysis*, Prentice-Hall, 1987.
- [58] Cook, R., *Concepts and applications of finite element analysis*, Wiley, 2001.
- [59] Donea, J. and Huerta, A., *Finite Element Methods for Flow Problems*, Wiley, 2003.
- [60] Oñate, E., *Structural Analysis with the Finite Element Method. Linear Statics. Vol. 2: Beams, Plates and Shells*, Springer Netherlands, 2013.
- [61] Malkus, D. S. and Hughes, T. J., "Mixed finite element methods — Reduced and selective integration techniques: A unification of concepts," *Computer Methods in Applied Mechanics and Engineering*, Vol. 15, No. 1, 1978, pp. 63–81.
- [62] BABUSKA, I. and MELENK, J. M., "THE PARTITION OF UNITY METHOD," *International Journal for Numerical Methods in Engineering*, Vol. 40, No. 4, 1997, pp. 727–758.
- [63] Tian, R., Yagawa, G., and Terasaka, H., "Linear dependence problems of partition of unity-based generalized FEMs," *Computer Methods in Applied Mechanics and Engineering*, Vol. 195, No. 37, 2006, pp. 4768–4782, John H. Argyris Memorial Issue. Part I.
- [64] An, X., Zhao, Z., Zhang, H., and Li, L., "Investigation of linear dependence problem of three-dimensional partition of unity-based finite element methods," *Computer Methods in Applied Mechanics and Engineering*, Vol. 233–236, 2012, pp. 137–151.
- [65] Babuska, I., Banerjee, U., and Kergrene, K., "Strongly stable generalized finite element method: Application to interface problems," *Computer Methods in Applied Mechanics and Engineering*, Vol. 327, 2017, pp. 58–92, *Advances in Computational Mechanics and Scientific Computation—the Cutting Edge*.
- [66] Temam, R., *Navier-Stokes Equations*, AMS Chelsea Publishing, 1977.
- [67] Roache, P. J., "Code Verification by the Method of Manufactured Solutions," *Journal of Fluids Engineering*, Vol. 124, No. 1, 11 2001, pp. 4–10.
- [68] Szabó, B. and Babuska, I., *Finite Element Analysis*, Wiley Series in Computational Mechanics, Wiley, 1991.
- [69] Hughes, T. J., Feijóo, G. R., Mazzei, L., and Quincy, J.-B., "The variational multiscale method—a paradigm for computational mechanics," *Computer Methods in Applied Mechanics and Engineering*, Vol. 166, No. 1, 1998, pp. 3–24, *Advances in Stabilized Methods in Computational Mechanics*.

- [70] Kim, D.-J., Pereira, J. P., and Duarte, C. A., "Analysis of three-dimensional fracture mechanics problems: A two-scale approach using coarse-generalized FEM meshes," *International Journal for Numerical Methods in Engineering*, Vol. 81, No. 3, 2010, pp. 335–365.
- [71] Duarte, C. and Kim, D.-J., "Analysis and applications of a generalized finite element method with global–local enrichment functions," *Computer Methods in Applied Mechanics and Engineering*, Vol. 197, No. 6, 2008, pp. 487–504.
- [72] O'Hara P., Duarte C. A., Eason T., and Garzon J., "Efficient analysis of transient heat transfer problems exhibiting sharp thermal gradients," *Computational Mechanics*, Vol. 51, No. 5, 2013, pp. 743–764.
- [73] Li, H., O'Hara, P., and Duarte, C., "A two-scale generalized FEM for the evaluation of stress intensity factors at spot welds subjected to thermomechanical loads," *Engineering Fracture Mechanics*, Vol. 213, 2019, pp. 21–52.
- [74] Noor, A. K., "Global-local methodologies and their application to nonlinear analysis," *Finite Elements in Analysis and Design*, Vol. 2, No. 4, 1986, pp. 333–346.
- [75] O'Hara, P., Duarte, C. A., and Eason, T., "Generalized finite element analysis of three-dimensional heat transfer problems exhibiting sharp thermal gradients," *Computer Methods in Applied Mechanics and Engineering*, Vol. 198, 2009, pp. 1857–1871.
- [76] Kim D.-J., Duarte C. A., and Sobh N. A., "Parallel simulations of three-dimensional cracks using the generalized finite element method," *Computational Mechanics*, Vol. 47, No. 3, 2011, pp. 265–282.
- [77] Oskay, C., "Variational multiscale enrichment method with mixed boundary conditions for modeling diffusion and deformation problems," *Computer Methods in Applied Mechanics and Engineering*, Vol. 264, 2013, pp. 178–190.
- [78] Zhang Shuhai and Oskay Caglar, "Variational multiscale enrichment method with mixed boundary conditions for elasto-viscoplastic problems," *Computational Mechanics*, Vol. 55, No. 4, 2015, pp. 771–787.
- [79] BATEMAN, H., "SOME RECENT RESEARCHES ON THE MOTION OF FLUIDS," *Monthly Weather Review*, Vol. 43, No. 4, 04 1915, pp. 163–170.
- [80] Burgers, J., "A Mathematical Model Illustrating the Theory of Turbulence," Vol. 1 of *Advances in Applied Mechanics*, Elsevier, 1948, pp. 171–199.
- [81] Bonkile Mayur P., Awasthi Ashish, Lakshmi C., Mukundan Vijitha, and Aswin V. S., "A systematic literature review of Burgers' equation with recent advances," *Pramana*, Vol. 90, No. 6, 2018, pp. 69.

- [82] Burgers, J., *The Nonlinear Diffusion Equation*, Springer Netherlands, 1974.
- [83] Bayona, C., Baiges, J., and Codina, R., "Variational multiscale approximation of the one-dimensional forced Burgers equation: The role of orthogonal sub-grid scales in turbulence modeling," *International Journal for Numerical Methods in Fluids*, Vol. 86, 08 2017.
- [84] LeVeque, J. R., *Numerical Methods for Conservation Laws*, Birkhäuser Basel, 1992.
- [85] Kutluay, S., Bahadir, A., and Özdeş, A., "Numerical solution of one-dimensional Burgers equation: explicit and exact-explicit finite difference methods," *Journal of Computational and Applied Mathematics*, Vol. 103, No. 2, 1999, pp. 251–261.
- [86] Dey, S. K., Dey, C., and Center, A. R., *An explicit predictor-corrector solver with applications to Burgers' equation [microform]* / Suhrit K. Dey and Charlie Dey, National Aeronautics and Space Administration, Ames Research Center Moffett Field, Calif, 1983.
- [87] Ozis, T. and Ozdes, A., "A direct variational methods applied to Burgers' equation," *Journal of Computational and Applied Mathematics*, Vol. 71, No. 2, 1996, pp. 163–175.
- [88] Shilt, T., O'Hara, P. J., and McNamara, J. J., "Stabilization of advection dominated problems through a generalized finite element method," *Computer Methods in Applied Mechanics and Engineering*, est. 2021. IN REVIEW.